

DISSERTATION

Characterization of the Wireless MIMO Channel

ausgeführt zum Zwecke der Erlangung des akademischen Grades eines
Doktors der technischen Wissenschaften

eingereicht an der

Technischen Universität Wien

Fakultät für Elektrotechnik und Informationstechnik

durch

Dipl.-Ing. Helmut Hofstetter

Landersdorferstrasse 33A, 3500 Krems

geboren am 18. Oktober 1975 in Krems

Matr. Nr. 9525327

Wien, im September 2006

Date of examination:

21. September 2006

Supervisor:

Univ. Prof. Dr. Ernst Bonek
TECHNISCHE UNIVERSITÄT WIEN, AUSTRIA

Examiner:

Prof. Dr. Andreas Molisch
LUND UNIVERSITY, SWEDEN

To My Parents

Zusammenfassung

Diese Dissertation beschäftigt sich mit der Charakterisierung des Mobilfunkkanals für Mehrantennensysteme mit Antennengruppen an Sende- und Empfangsseite. Solche Systeme werden allgemein als MIMO-Systeme (Multiple-Input Multiple-Output Systeme) bezeichnet.

Im ersten Teil werden der Mobilfunkkanal und seine typischen Eigenschaften erklärt und unterschiedliche Ansätze zur Modellierung des Kanals erläutert. Dabei wird speziell auf standardisierte Kanalmodelle eingegangen, deren Konzept dem vorgestellten Kanalmodell ähnelt. Besonderes Augenmerk gilt den COST 259 und COST 273 Kanalmodellen, welche als Basis für das neu entwickelte Kanalmodell dienen.

Der zweite Teil beschäftigt sich mit Messungen des Mobilfunkkanals und deren Evaluierung. Zu Beginn wird das verwendete Messequipment beschrieben, gefolgt von einer Auflistung der Messumgebungen. Gemessen wurden Makrozellen in urbanen Gebieten wie auch Pikozellen in Hallen und in Büroumgebungen. Dabei wurden im Durchschnitt Kanalkapazitäten von bis zu 11 bits/s/Hz für 4x4 Antennensysteme bei einem SNR von 10 dB festgestellt. Die Kapazität wird sowohl mit der üblichen Annahme konstanter Empfangsleistung als auch unter dem Ansatz konstanter Sendeleistung berechnet, welche zu einem faireren Vergleich der Kapazitäten ganzer Systeme führt. Im Fall einer direkten Sichtverbindung zwischen Sender und Empfänger bewirkt die weit höhere Empfangsleistung eine höhere Kapazität des Kanals unter der Annahme konstanter Sendeleistung verglichen mit Messungen ohne direkte Sichtverbindung. Unter der Annahme konstanter Empfangsleistung ist das Ergebnis aufgrund der höheren Diversität des Kanals genau umgekehrt. Gleichpolarisierte Sende- und Empfangsantennen erreichen die höchsten Kapazitätswerte. Zweifach polarisierte Empfangsantennen an der Mobilstationsseite erreichen annähernd hohe Kapazitätswerte, sind aber resistent

gegenüber Drehungen des Mobilteils. Dadurch präsentieren sich zweifach polarisierte Antennen als vielversprechende Lösung zur Erreichung hoher Kapazitäten auch für kleine Empfangsgeräte wie Mobiltelefone oder PDAs.

Der Hauptteil der Dissertation behandelt die Einführung und Implementierung eines neuen Kanalmodells. Dabei handelt es sich um die Erweiterung eines geometrie-basierten Kanalmodells (sogenannten GSCM-Modell) um für MIMO-Systeme relevante Eigenschaften. Zuerst wird eine allgemeine Struktur für Kanalmodelle vorgestellt, welche auf zahlreichen Modulen und klar definierten Schnittstellen zwischen diesen Modulen basiert. Die nachfolgende Beschreibung der einzelnen Module orientiert sich an der Implementierung des Kanalmodells. Das Konzept des Kanalmodells basiert auf der Annahme, dass Mehrwegekomponenten in Gruppen, sogenannten Clustern, auftreten. Dabei wird zwischen lokalen Clustern rund um die Basisstation und die Mobilstation, einfach interagierenden Clustern und Zwillingclustern unterschieden. Das Konzept der Zwillingcluster stellt eine einfache Möglichkeit dar, die Limitierungen der einfach interagierenden Cluster ohne Erhöhung der Komplexität eines Kanalmodells zu umgehen. Lösungen für die Verteilung und Gewichtung der interagierenden Objekte in bewegten und räumlich fixierten Clustern werden gezeigt. Um eine einfache Adaptierung des Kanalmodells an zahlreiche Empfangsalgorithmen zu erleichtern werden drei Synchronisationsmethoden vorgestellt, welche auch Mehrbenutzersimulationen unterstützen. Das Kanalmodell ermöglicht auch grossräumige Bewegungen der Mobilstation und benötigt dafür eine adäquate Modellierung der Kanaldämpfung. Eine Methode zum Abgleich der mittleren Kanaldämpfung auf die Werte zahlreicher Dämpfungsmodelle basierend auf einer Monte-Carlo Simulation wird vorgestellt.

Der letzte Teil beschäftigt sich mit der Validierung des vorgestellten Kanalmodells. Dazu werden physikalische Grössen wie die Amplituden- und Phasenstatistiken oder das Dopplerspektrum betrachtet. Ergebnisse für die MIMO-Kapazität zeigen eine gute Übereinstimmung mit den Messergebnissen aus Kapitel 3. Zur Validierung des Modells in Hinblick auf großflächige Änderungen des Kanals wird der 'F-eigen ratio' als Kenngröße herangezogen. Als letzter Punkt wird die praktische Verwendbarkeit des Modells anhand eines Empfangsalgorithmuses inklusive Kanalschätzung demonstriert. Das Modell verhält sich sehr realistisch und erlaubt die Anpassung von Empfangsalgorithmen an die Realität.

Abstract

This thesis describes the characterization of the wireless MIMO channel via the analysis of measurement data and introduces and validates a new channel model.

In the first part a short introduction to the wireless MIMO channel is given. Starting with a brief review of the propagation effects of the wireless channel, the various channel modelling approaches are compared. The principal concept of standardized channel models related to the work of this thesis is discussed. The major focus is put on the COST 259 and COST 273 channel models that serve as the basis for the presented channel model.

The second part is dedicated to MIMO measurements and their evaluation. A description of the measurement hardware and its functionality is presented first. The measurement scenarios are then described. Macrocellular urban areas as well as picocell areas in office environments and halls were chosen.

The evaluation of these measurements shows an average mutual information of up to 11 bits/s/Hz for a 4x4 antenna system at 10 dB SNR. The standard approach of constant receive power is compared to the case of constant transmit power, which seems to be fairer from a system point of view. Normalizing the measured channels to constant transmit power shows that the LOS case is superior to the NLOS case in terms of mutual information due to the higher receive power in the LOS case. It turns out that co-polarization of transmit and receive antenna results in the highest mutual information. Dual-polarized antenna arrays at the mobile terminal side show nearly the same high values of the mutual information and are robust against rotations of the MT. Therefore dual-polarized antennas are a promising way of achieving high capacities for small devices like PDAs or mobile phones.

The major contribution of this thesis is the introduction and implementation of a new channel model. The GSCM approach is extended to the needs of MIMO channel models using several approaches found in literature. At first a structure for the model

is proposed based on functional modules and clearly defined interfaces in between. The description of the modules focuses on implementational aspects. The model can cope with local clusters around the BS and the MT as well as single-interaction clusters and the novel twin-clusters. The twin-cluster concept is introduced as a way to overcome the limitations of the single-interaction channel models and to make the model fully MIMO compliant. Solutions for the distribution of IOs inside of moving clusters are shown and several weighting strategies for the IOs are discussed. To allow for an easy adaptation of the model to various receive algorithms three synchronisation modes of interest are identified, including multi-user scenarios. Since the model can cope with large movements of the MT an appropriate modeling of the pathloss is important. An approach using a Monte-Carlo simulation to obtain the average receive power levels as specified by various pathloss models is introduced.

In the last part, the channel model and its implementation is validated by physical measures like the amplitude and phase statistics or the Doppler spread. Results of the mutual information obtained in various simulation environments are presented and their fit to the estimated mutual information from the measurement evaluation in Chapter 3 is shown. The F-eigen ratio is used to validate the large-scale properties of the model. At the end a receive algorithm is used to demonstrate the usability of the model for performance evaluations of receive algorithms including channel estimation. The model shows very realistic performance results and allows for a better tuning of receive algorithms.

Acknowledgment

The help of various people has made this thesis possible or complete:

Prof. Ernst Bonek for supporting me with my PhD, his encouraging words, and giving me a vision on my research. Especially I want to thank him for facilitating an open-minded atmosphere in his group which brought up a lot of constructional criticism.

Prof. Andreas Molisch for introducing the field of wireless channel modelling to me and very fruitful technical discussions. His outstanding technical expertise was a valuable resource for finding new approaches.

Furthermore I would like to thank FTW – it was a pleasure for me to work in this outstanding and international group. The variety of knowledge in different fields brought together always served valuable for getting on. I like to mention especially Christoph Mecklenbräuker for all his support and engagement to allow me a continuous research on the topic of my thesis over various projects. Special thanks go to Thomas Zemen for his support with the test of my channel model, Nicolai Czink and Bernard Fleury for fruitful discussions on channel modelling and measurements, Harald Kuncier for the various discussions in our office, Hermann Anegg and Joachim Wehinger for their support with the measurement campaigns, Ralf Müller and Merouane Debbah who showed me the field of stochastic channel modelling, Markus Kommenda and Horst Rhode for their commitment for a research friendly atmosphere at FTW, and Stavros, John, Katja, Thomas, Per, Rainer, Florian and Horst for their support.

I also want to thank all the project partners showing their interest in my research: Austrian Research Centers GmbH, Infineon Technologies AG, Mobilkom Austria AG & Co KG, and Siemens AG Österreich.

I thank all colleagues from the Mobilfunkgruppe at TU Wien, especially Markus Herdin, Hüseyin Özcelik and Martin Steinbauer for their support with the measurements and the discussion on measurement results. In addition I want to thank Ingo Viering from Siemens for his support with the measurements and the discussion on the results.

Within the group of COST273, I thank its chairman Prof. Luis Correia for supporting the subgroups on MIMO Systems (SWG2.1) and Channel Measurements (SWG2.3). I thank all active participants who have lent their expertise for designing the common COST273 model, especially Henrik Asplund from Ericsson Radio AB, Claude Oestges from UCL, Christiane Kuhnert and Thomas Fuegen from University of Karlsruhe, Prof. Reiner Thomä, Wim Kotterman and Giovanni Del Galdo from TU Ilmenau, Prof. Pertti Vainikainen from HUT, Prof. Alister Burr from the University of York, and Prof. Robert Bultitude from CRC.

From the FLOWS project, I thank all partners for the cooperative atmosphere, especially Per Lehne and Magne Pettersen from Telenor R&D who supported me with the measurement campaigns carried out within the FLOWS project and the project leader Dave Evans from Philips. Funding of the FLOWS project by the Commission of the European Communities (IST-2001-32125) is further acknowledged.

Special thanks go to my sister for her support during my thesis. Furthermore I want to thank my volleyball club *Pizza Funghi*.

Last but not least, for supporting me in any situation, and with all their efforts, my parents deserve my deepest gratitude.

Table of Contents

Table of Contents	vii
1 Introduction	1
1.1 Outline	4
1.2 Contributions	6
1.3 Notation	10
2 The wireless MIMO Channel	11
2.1 Multi-path Propagation	11
2.2 Channel Model Characterization	14
2.2.1 Stochastic Channel Models	15
2.2.2 Deterministic (Ray-tracing) Models	15
2.2.3 Geometry based Stochastic Channel Models	16
2.3 Standardized Channel Models	17
2.3.1 COST 207 and COST 231	18
2.3.2 The COST 259 Channel Model	19
2.3.3 The 3GPP/3GPP2 Spatial Channel Model	20
2.3.4 The COST 273 Channel Model	21
2.4 Antenna Arrays and Polarization	23
3 MIMO Channel Measurements	25
3.1 Measurement Equipment	26
3.1.1 Measurement Principle	26
3.1.2 Medav RUSK-ATM Channel Sounder	28
3.1.3 Sintef Channel Sounder	32
3.2 Measurement Scenarios	39
3.2.1 Suburban area - Weikendorf measurements	39
3.2.2 Urban area - Oslo Kvadraturen	39

3.2.3	Picocell Indoor - Telenor Headquarter Fornebu	40
3.3	Measurement Evaluation	46
3.3.1	Mutual Information	46
3.3.2	Long Term Properties of the Channel	56
3.3.3	Polarization	62
4	A new MIMO Channel Model	65
4.1	Interfaces and Modules	66
4.1.1	PA-Interface	69
4.1.2	AC-Interface	72
4.1.3	Convolution Module	72
4.1.4	Receive and Transmit Filter	81
4.1.5	Impulse Response Module	81
4.1.6	Antenna Module	81
4.1.7	Propagation Module	84
4.2	Cluster Distribution	86
4.2.1	Local Clusters	86
4.2.2	Single-interaction Cluster	86
4.2.3	The Twin Cluster Concept	90
4.3	Cluster Visibility	94
4.3.1	Single-interaction Cluster	97
4.3.2	Twin Cluster	97
4.4	Cluster Power Model	97
4.5	Interacting Object Distribution and Weighting	98
4.5.1	Local Clusters	98
4.5.2	Single-interaction Cluster	106
4.5.3	Twin Cluster	108
4.6	LOS Component	109
4.7	Polarization	110
4.8	Shadow Fading	111
4.9	Delay/ Azimuth/ Elevation Dispersion	111
4.10	Parameter Updates	112
4.11	Power Compatibility and Pathloss	113
4.12	Multi-User Case	120
5	Channel Model Validation	121
5.1	Replacement of IOs	122
5.2	Amplitude and Phase Statistics	124
5.3	Transfer Function	125

5.4	Doppler Spread	125
5.5	Small-Scale Fading	127
5.6	Mutual Information	128
5.7	Large-Scale Variations and Pathloss	130
5.8	F-eigen-ratio	131
5.9	Multi-User Detector	138
5.9.1	Overview	138
5.9.2	Simulation Environment	139
5.9.3	Results	142
6	Conclusions and Outlook	145
A	Model Parameter Sets	149
B	List of Abbreviations	155
C	List of Symbols	159
	Bibliography	163

Chapter 1

Introduction

Multiple-Input Multiple-Output (MIMO) systems are one promising way of achieving high data rates in broadband wireless communication systems [1], [2]. In principle, the information-theoretic capacity of these systems can increase linearly with the number of antennas. Figure 1.1 shows the achievable MIMO capacity for various numbers of transmit (Tx) and receive (Rx) antennas for i.i.d. Gaussian channels. It is obvious that MIMO can boost the throughput of communication systems.

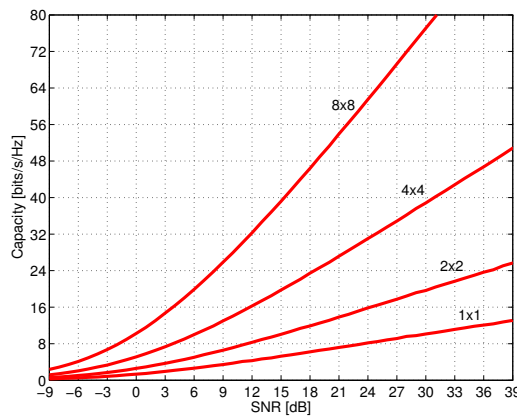


Figure 1.1: Achievable MIMO capacity for various numbers of Tx and Rx antennas and i.i.d. Gaussian channels.

MIMO systems have now found their way into standards like the IEEE 802.11n standard for high-throughput wireless local area networks [3] and the long term evolution (LTE) of the third generation cellular standard 3GPP. Furthermore first products using MIMO techniques are now on the market.

Realistic channel models are one key technique in order to design new systems

and to evaluate their performance. A first step towards realistic channel models is to explore the nature of the wireless channel using channel measurements. The topic of channel measurements has considerably improved over recent years. Starting from single-input single-output (SISO) measurements several years ago people have included antenna arrays at the transmit side or the receive side. The resulting directional channel [4] is called a single-input multiple-output (SIMO) or multiple-input single-output (MISO) channel depending on whether transmit or receive side the antenna array is employed. Such directional measurements like [5] had big influence on the standardization of the COST259 channel model [6]. However, for MIMO systems and channel models the double-directional channel, as introduced by Steinbauer [4], has to be measured and analyzed. MIMO measurements can be performed using a network analyzer plus positioning equipment for creating virtual antenna arrays [7]. The best way, but also the most expensive one, is to use dedicated measurement hardware specifically built for the measurement of the wireless MIMO channel. The two leading companies in the field of MIMO measurement hardware are Medav [8] and Elektrobit [9]. This state-of-the-art equipment allows even measuring the MIMO channel in highly dynamic environments including a mobile transmitter and/or a mobile receiver.

The analysis of the MIMO measurements can be divided into two research areas: (i) analysis of stochastic properties of the channel and (ii) exploring the double-directional nature of the channel. The most prominent stochastic measure of the MIMO channel is its capacity [2]. Several papers have investigated in this measure analyzing various environments [10], [11]. Other people investigated in the stationarity of the MIMO channel [12], the eigenvalue distributions [13], [11], and the spatial covariance matrices and second order statistics of the channel [14], [15].

Exploring the double-directional channel is based on the evaluation of the multipath components (MPC). Algorithms like SAGE [16], [17] and ESPRIT [18], [19] were developed for extracting MPC parameters like the complex weight of the MPCs, their delays, DOAs, DODs, and Doppler shifts [17], [20], [21] from measurement data. The latter one also includes the estimation of the dense multipath components which are often called the *diffuse components* [22] of the channel. In [23] the extraction of MPC parameters is taken as the basis for the automatic clustering of the MPCs.

All the measurements and their evaluation establish the basis for the design and parametrization of new channel models representing reality more specific. One can

find a different taxonomy of channel models, distinguishing three generic approaches [24]: (i) stochastic models, (ii) deterministic (ray-tracing) based models, and (iii) geometry-based stochastic models (GSCMs).

Stochastic channel models describe the statistics of the transfer function matrix (or equivalently the impulse response matrix) where each entry in that matrix gives the transfer function from the i -th transmit to the j -th receive antenna element. They suit well for information theoretic investigations since their mathematical description allows for closed form solutions. A well known representative of this group of models is the Kronecker model which describes the channel as a Kronecker product of the correlation matrices at the transmit and receive side. It has considerable drawbacks [25] due to the assumption that the total correlation matrix is the Kronecker product of the correlation matrices of the transmitter and receiver. An extensions of the Kronecker model has been developed by Weichselberger [26] which mitigates this drawback. [27] discusses the goodness of the Kronecker model in comparison to the Weichselberger model and the virtual channel representation of Sayeed [28].

Deterministic (ray-tracing) channel models are well suited for site specific tasks like cell planning. They are able to predict the channel impulse response at several points of real world maps. Although many papers have covered narrow-band predictions using two-dimensional (2-D) and three-dimensional (3-D) ray-tracing tools [29],[30],[31], only few publications [32],[33] have addressed the wide-band issue from a physical point of view at small ranges. Therefore up to nine reflections are considered in some situations. This can lead to a prohibitive computational effort. In addition, in most areas, no complete description of the building shapes is available, so the prediction quality of most models will often be compromised. In [34] a simplified deterministic wide-band model is proposed which limits computational complexity but still enables the evaluation of several design parameters like the antenna height or the beamwidth. Even this simplified deterministic wide-band model requires substantial computational effort.

GSCMs are an efficient and natural way to simulate propagation channels: the location of scatterers and other interacting objects is placed at random, according to a certain probability distribution; during the simulation, the propagation of the MPCs from the transmitter to the receiver is then traced. GSCMs have been used for the simulation of systems with receive diversity antennas since the 1970s [35], and

developed in more detail in [36], [37], [38]. A more general, cluster-based model was introduced in [39]. The GSCM was also suggested as one method for implementing the standardized COST 259 channel model [40]. Furthermore it can be seen as the basis for the newly introduced COST 273 channel model, which is among the first standardized models specifically dedicated to the MIMO case.

The principal idea of the original GSCM models is based on the assumption that MPCs undergo only single-interaction processes on the way from the transmitter to the receiver. Even in those cases where an MPC undergoes multiple interaction processes, all those processes could be represented adequately by "equivalent" single-interaction processes. This concept works well for the simulation of SIMO (single-input-multiple-output) and MISO (multiple-input-single-output) systems. In this case it is always possible to describe the properties of a MPC (delay plus angle-of-arrival) by an "equivalent interacting object (IO)". In other words, an IO can always be placed in such a way that a single-interaction process leads to the desired delay and angle-of-arrival[41]. However, such an equivalent representation is *not* possible in MIMO systems. A number of attempts have been made at generalizing GSCMs to the MIMO case. [42] suggested a two-ring model (scatterers placed near the BS, and near the MT) that explicitly models double-interaction processes, and allows an explanation of the so-called "keyhole" effect. In [43] a double-bounce channel model for multi-polarized MIMO systems is introduced. [44] gave a comprehensive model that includes single- and double-interactions, as well as wave guiding and other effects.

In my thesis I propose an extended approach of the GSCM models. To reflect the demands of MIMO systems I split up the single-interaction cluster into two representation of itself. One, as seen by the base station (BS) and one as it is seen by the mobile terminal (MT). To ease the usage of the model I define a set of modules and interfaces which eases the adaptation of my model to several standardized channel models.

1.1 Outline

The key contribution of my thesis is the development of a new channel model that is suitable for the simulation of MIMO systems. For this purpose, I introduce new generic methods for simulating MIMO channels, and also provide measurement results that serve to parameterize this generic model.

Chapter 2 gives an introduction to the propagation mechanisms present in wireless communication systems. The description of the wave propagation is usually based on clustered sets of MPCs. I will give a definition of a cluster based on physical constraints.

The first step towards new and more realistic channel models is to measure the channel and extend the knowledge on the propagation mechanism. In Chapter 3 I will first describe the measurement equipment I have used for my MIMO measurement campaigns followed by an overview on the measurement environments chosen for the measurements.

The topic of MIMO channel modelling is always closely related to the information theoretic MIMO capacity [2]. I will briefly review this measure and explain why the term MIMO capacity is misleading in terms of MIMO measurements and most MIMO channel models.

I will discuss the problem of measurement noise for the estimation of mutual information and show how it influences the calculations. A somehow unsolved problem of calculating mutual information is the power normalization of the channel impulse responses. I will discuss this problem in detail and show a way how to obtain reasonable results. After this discussion I will show results for the mutual information obtained in rural areas. The usage of a dual polarized receive antenna at the MT allows the investigation of polarization effects on the mutual information. This leads to the next topic of my measurement evaluation where I will discuss the cross polarization discrimination factor of urban and indoor environments.

Also the long term properties of the MIMO channel are covered by my channel model. To validate the long term property of my model against measurements I use the F-eigen ratio [14]. I will show results obtained from urban area measurement, followed by a statistical analysis of the channel using the WSS Quality Q_{WSS} of [45].

Channel modelling is the main component of my thesis. In Chapter 4 my modelling approach is discussed in detail. It is an extension of the GSCM approach. I will start with the definition of several modules I use, like the Antenna Module or the Convolution Module. The heart of my channel model is the Propagation Module. It covers all relevant computations for placing clusters and MPCs. My major contributions are the extension of the GSCM to the MIMO case which inherently leads to the introduction of the twin clusters as a novel clustering approach. The twin

cluster concept allows for independent delay and angular statistics at both, BS and MT side. A clear mathematical formulation of all the steps invoked in the modelling process is one additional advantage. For system simulations, one needs to model not only the propagation channel, but also antennas and transmit/receive filters. The antenna pattern defines the visibly surrounding of the BS and MT and therefore changes the characteristics of the channel. The receive filter of the channel model defines the bandwidth of the channel and therefore also the temporal resolution. It therefore also influences the statistics of the channel. All these considerations are taken into account using separate modules. My model is able to cope with multiple MTs and BSs to allow for the investigation of multiple user scenarios. This feature becomes more and more important since state of the art technologies like CDMA and OFDM systems demand for realistic co-channel interference modelling.

A channel model has to be validated to show its physical correctness and its usefulness. Chapter 5 discusses the properties of my model in detail. It starts with the validation of well known physical propagation statistics. In a next step results on the mutual information demonstrate the physical behavior of the model. The long term properties of my channel model are discussed and compared with my measurement results of Section 3. As the last topic of this section an application of my model is discussed. It is shown that the usage of GSCMs for the receive algorithm design and test is very beneficial and yields more realistic performance results than simple stochastic models.

This application of my model directly leads to the last chapter of my thesis which summarizes the results and highlights the major contributions.

1.2 Contributions

Parts of this thesis have been or will be presented in journals and conferences. During my thesis I have collaborated with many people. In the following I will point out my contributions on the joint papers I have written together with them.

Papers about the measurements I have conducted:

- H. Hofstetter, C. Mecklenbräuker, H. Anegg, E. Bonek, R. Müller, and H. Kunczler, *The FTW wireless MIMO measurement campaign at 2GHz: documentation of the downloadable data sets*, COST 273, TD(02)135, 2002.
- D. Evans, L. Correia, H. Hofstetter, A. Burr, H. Rohling, G. Lehmann, R. Williams, and P. Lehne, *Flexible Convergence of Wireless Standards and Services. The IST FLOWS Project - An Overview*, E&I Journal, 2003.
- P. Lehne, H. Hofstetter, and M. Debbah, *Eigenvalue distributions and capacity evaluations from outdoor MIMO measurements at 2.1GHz*, in Proceedings of the IST Mobile and Wireless Communications Summit 2003, (Aveiro, Portugal), June 2003.
- M. Herdin, H. Özcelik, H. Hofstetter, and E. Bonek, *Linking Reduction in Measured MIMO Capacity with Dominant-Wave Propagation*, COST 273, TD(02)157.
- R. Müller and H. Hofstetter, *Confirmation of random matrix model for antenna array channel by indoor measurements*, in Proceedings of the IEEE Antennas & Propagation Society Symposium, (Boston, USA), July 2001.
- H. Hofstetter, M. Steinbauer, and C. Mecklenbräuker, *Double-directional radio channel estimation at 2GHz for high speed vehicular mobiles - Experimental results*, in Proceedings of the International Symposium on Wireless Personal Multimedia Communications (WPMC), (Aalborg, Denmark), September 2001.
- E. Bonek, H. Hofstetter, C. Mecklenbräuker, and M. Steinbauer, *Double-directional Superresolution Radio Channel Measurements*, in Proceedings of the 39th Annual Allerton Conference on Communication, Control, and Computing, (Monticello, USA), October 2001.
- E. Bonek, M. Steinbauer, H. Hofstetter, and C. Mecklenbräuker, *Double-directional radio channel measurements - What we can derive from them*, in Proceedings of the International Symposium on Signals, Systems, and Electronics, (Tokyo, Japan), July 2001.

The F-eigen ratio is based on an idea of Ingo Viering and we have published the following papers about the evaluation of the F-eigen ratio using measurement data I have collected:

- I. Viering, H. Hofstetter, and W. Utschick, *Spatial Long-Term Variations in Urban, Rural and Indoor Environments*, COST 273, TD(02)131, 2002.
- I. Viering and H. Hofstetter, *Potential of Coefficient Reduction in Delay, Space and Time based on Measurements*, in Proceedings of the Conference on Information Sciences and Systems (CISS), (Baltimore, USA), March 2003.
- I. Viering, H. Hofstetter, and W. Utschick, *Validity of Spatial Covariance Matrices over Time and Frequency*, in Proceedings of the IEEE Global Telecommunications Conference (GLOBECOM), (Taipei, Taiwan), November 2002.
- H. Hofstetter, I. Viering, and W. Utschick, *Evaluation of Suburban Measurements by Eigenvalue Statistics*, in Proceedings of the COST 273 Workshop, (Espoo, Finland), May 2002.
- H. Hofstetter, I. Viering, and P. Lehne, *Spatial and temporal long term properties of typical urban base stations at different heights*, COST 273, TD(03)061, 2003.
- I. Viering and H. Hofstetter and W. Utschick, *Spatial Long-Term Variations in Urban, Rural and Indoor Environments*, COST 273, TD(02)131, 2002.

When talking about "my model", I mean the model I have developed and implemented in collaboration with other COST 273 members, especially Nicolai Czink, Gerhard Steinböck, and Andreas F. Molisch.

- A.F. Molisch and H. Hofstetter, *The COST-273 MIMO Channel Model*, in *TOWARDS MOBILE BROADBAND MULTIMEDIA NETWORKS (COST 273)*, Section 4.7, Luis Correia (Ed.), May 2006.
- H. Hofstetter, A. Molisch, and M. Steinbauer, *Implementation of a COST 259 Geometry based Stochastic Channel Model for Macro- and Microcells*, in Proceedings of the European Personal Mobile Communication Conference (EPMCC), (Vienna, Austria), February 2001.
- H. Hofstetter and G. Steinböck, *A Geometry based Stochastic Channel Model for MIMO Systems*, in Proceedings of the ITG Workshop on Smart Antennas, (Munich, Germany), March 2004.

- H. Hofstetter, *MIMO Channel Modeling: COST-273 and 3GPP-SCM*, in Tutorial on Smart Antennas, European Microwave Week (EuMW 2003), Munich, Germany, September 2003.
- H. Hofstetter and G. Steinböck, *A Geometry based Stochastic Channel Model for MIMO – Athen 2004*, COST 273, TD(04)060, 2004.
- H. Hofstetter, A. Molisch, and N. Czink, *A twin-cluster MIMO channel model*, in Proceedings of the European Conference on Antennas and Propagation (Eu-Cap)), (Nice, France), p. to be published, November 2006.

The application of my channel model is based on the receive algorithm of Thomas Zemen. We have written the following papers on our investigations:

- H. Hofstetter, T. Zemen, J. Wehinger and G. Steinböck, *Iterative MIMO Multi-User Detection: Performance Evaluation with COST 259 Channel Model*, in Seventh International Symposium on Wireless Personal Multimedia Communications (WPMC), Abano Terme, Italy, September 12-15, 2004, invited paper.
- T. Zemen, H. Hofstetter, G. Steinböck, *Subspace Projection in the Time and Frequency Domain for Time-Variant Multi-User MIMO OFDM Channel Estimation*, COST 273, TD(04)203, Duisburg, Germany, September 20-22, 2004.
- T. Zemen, H. Hofstetter and G. Steinböck, *Successive Slepian Subspace Projection in Time and Frequency for Time-Variant Channel Estimation*, in 14th IST Mobile and Wireless Communication Summit (IST SUMMIT), Dresden, Germany, June 19-22, 2005.

1.3 Notation

I will use the notation listed in Table 1.1 throughout my thesis.

Symbol	Description
a	scalar
$ a $	absolute value of a
\vec{a}	vector
\mathbf{a}	matrix
$\tilde{\mathbf{a}}$	estimate of \mathbf{a}
$\hat{\mathbf{a}}$	outdated version of \mathbf{a}
$\mathbf{a}_{n,m}$	n, m -th element of \mathbf{a}
\mathbf{a}^H	conjugate transpose of \mathbf{a}
\mathbf{a}^T	transpose of \mathbf{a}
\mathbf{I}_Q	$Q \times Q$ identity matrix
j	$\sqrt{-1}$
$\delta(k)$	1 for $k = 0$, 0 otherwise
$\mathbf{a} * \mathbf{b}$	convolution of \mathbf{a} and \mathbf{b}
$a \otimes b$	Kronecker product of a and b
$CDF(a)$	cumulative distribution function of a
$PDF(a)$	probability density function of a
$f(a)$	distribution function of a
$\mathcal{U}(a, b)$	Uniform distribution in the range $a - b$
$\mathcal{N}(\mu/\sigma)$	Normal distribution with mean μ and variance σ
$\mathcal{N}_{log}(\mu/\sigma)$	Log-Normal distr. with mean μ and variance σ
$\mathbf{E}\{a\}$	expectation of a

Table 1.1: Notation used throughout my thesis.

Chapter 2

The wireless MIMO Channel

In this chapter I will first discuss the properties of the wireless channel based on multipath propagation. In the sequel I will give a classification of channel models and discuss standardized channel models relevant for my work. The influence of antenna arrays and polarization for a channel model is discussed in the last section of this chapter.

2.1 Multi-path Propagation

Multi path propagation is one of the properties of the wireless propagation channel [46], [47], [24]. Each single MPC has a specific delay corresponding to its path length, is attenuated according to the propagation effects and propagates into certain directions. Multi-path propagation causes fading effects due to the superposition of several MPCs at the receiver and inter-symbol interference due to the different path delays. Figure 2.1 shows an example of multi-path propagation. Depending on the environment a direct path between the BS and the MT may exist, a so called line-of-sight (LOS) component. In addition waves emitted at the transmitter find their way to the receiver via single or multiple interactions at objects in the surrounding of the wireless system. Such interacting objects (IO) might be houses, walls, trees or windows and furniture - depending on the propagation environment. The basic mechanisms that govern the propagation of electromagnetic waves are

- Reflection,
- Transmission,
- Diffraction, and
- Scattering.

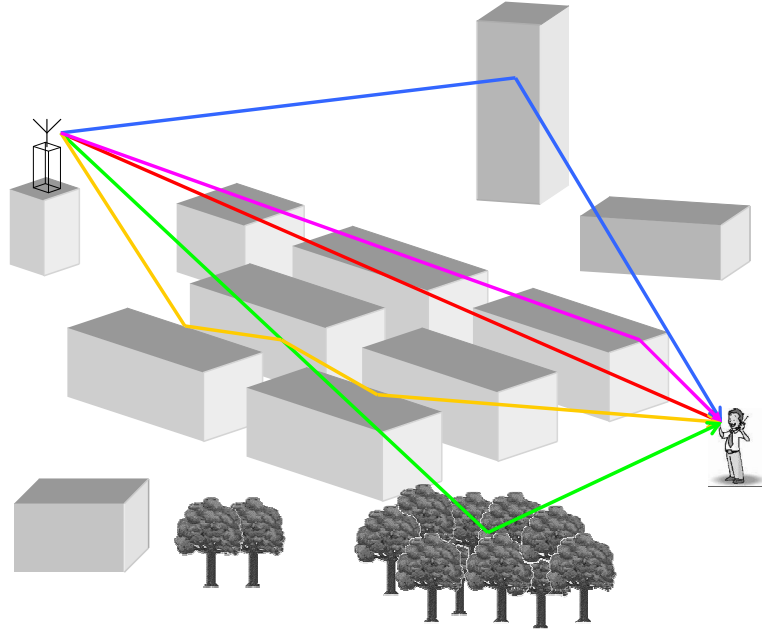


Figure 2.1: Multi-path propagation of the wireless channel.

Reflections occur at smooth surfaces and behave in accordance to Snell's law [48]. The angle of a reflected homogeneous plane wave (HPW) is always equal to the angle of the impinging HPW. When a wave hits a wall there is not only a reflection process but also part of the energy is transmitted through the wall. This transmission of waves is important for the indoor coverage by an outdoor BS. One propagation effect based on reflections, mainly appearing in dense urban areas, is the wave guiding through street canyons. In this case the paths are multiply reflected within a street canyon before they hit the receiver. Due to the small power loss at a reflection such paths have still considerable energy at the receiver.

Diffraction usually occurs at the edges of rooftops and at the house edges at street crossings. An edge can be seen as a new point source of a wave.

When a wave hits a rough surface it is scattered into all directions due to the irregularity of the surface. This process is called diffuse scattering. The roughness of a surface depends on the wavelength. Based on the Rayleigh criterion a surface is defined as smooth if $\Delta h < \lambda/8 \cos \theta$ where Δh denotes the standard deviation of the surface roughness, λ is the wavelength and θ is the angle of incidence. For a center frequency of 2 GHz and an angle of incidence of $\theta = 45^\circ$ a surface is called rough if $\Delta h > 13$ mm. One has to distinguish between truly random roughness assumed in theory, and the more regular structures like bookshelves or windowsills. Usually it is

sufficient to model small regular structures as rough surfaces. For ,e.g., ray-tracing predictions such details cannot be modelled (and are also not included in the used maps) and are therefore described by rough surfaces. Scattering is a very important propagation effect in mobile communications due to its spreading of waves into all directions. While reflected waves usually carry much more power, scattered waves are visible much more often.

Taking above propagation effects into account, the wireless propagation channel can be described as a set of MPCs, each represented by a HPW. Each MPC is described by its complex amplitude $|h_s| e^{j\phi_s}$, its delay τ_s , and its corresponding DODs and DOAs in azimuth and elevation,

$$h(t, \tau, \varphi_{\text{DOD}}, \varphi_{\text{DOA}}, \vartheta_{\text{DOD}}, \vartheta_{\text{DOA}}) = \sum_{s=1}^S |h_s| e^{j\phi_s} \delta(\tau - \tau_s) \delta(\varphi_{\text{DOA}} - \varphi_{\text{DOA},s}) \delta(\varphi_{\text{DOD}} - \varphi_{\text{DOD},s}) \delta(\vartheta_{\text{DOA}} - \vartheta_{\text{DOA},s}) \delta(\vartheta_{\text{DOD}} - \vartheta_{\text{DOD},s}), \quad (2.1)$$

where S denotes the number of MPCs of a certain environment. This impulse response is independent of any antennas and describes the double directional channel, as introduced in [4].

In MIMO systems the system dependent radio channel [4] from each transmit antenna ($1..n_T$) to every receive antenna ($1..n_R$) is required, which is depicted in Figure 2.2. The channel impulse response $\mathbf{h}(\tau)$ of the radio channel can therefore be

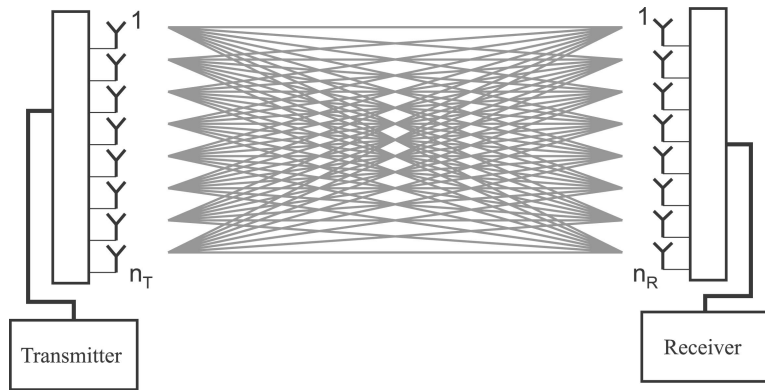


Figure 2.2: The MIMO channel matrix.

expressed as a matrix

$$\mathbf{h} = \begin{bmatrix} h_{11} & h_{21} & \cdots & h_{n_T 1} \\ h_{12} & h_{22} & \cdots & \vdots \\ \vdots & \vdots & \ddots & \vdots \\ h_{1n_R} & \cdots & \cdots & h_{n_T n_R} \end{bmatrix}, \quad (2.2)$$

where the columns and rows denote the different combinations of transmit and receive antenna impulse responses¹. All the single entries of (2.2) are representations of (2.1) for certain combinations of transmit and receive antenna elements. Due to the angular spread, the finite number of MPCs, and the finite separation of antenna elements the statistics of the impulse responses of different antenna combinations are not independent but contain some dependencies since they result from different superpositions of the same MPCs. The goal of a channel model is to describe the channel matrix in a most appropriate way, including all possible correlation effects. From my point of view this implies that the antennas have to be part of the channel model and therefore the model describes the whole radio channel and not only the propagation channel. In literature a lot of different channel modelling approaches can be found. I will classify these approaches and give a short explanation on them in the next section.

2.2 Channel Model Characterization

In accordance with [24] I divide the MIMO channel models into three major groups:

- Stochastic channel models,
- Deterministic (ray-tracing) models,
- Geometry based stochastic channel models (GSCMs).

I will briefly discuss the stochastic and the deterministic channel models in the following. The GSCMs are the basis for my own work and therefore I will go into more detail for this type of models.

¹All the dependencies of the impulse response are now suppressed to increase readability. The dependency of the impulse response on several parameters will be discussed in the next section in more detail.

2.2.1 Stochastic Channel Models

Stochastic channel models prescribe statistics of the impulse response (possibly including directional characteristics). It is then possible to generate realizations of the impulse response according to those statistics.

A very popular stochastic channel model is the Kronecker model [49], [50] where the full covariance matrix of the channel is separated into a transmit covariance matrix $\mathbf{R}_{\text{Tx}} = \mathbf{E}\{(h^H h)^T\}$ and a receive covariance matrix $\mathbf{R}_{\text{Rx}} = \mathbf{E}\{h h^H\}$

$$\mathbf{R}_{kron} = \frac{1}{\text{tr}\{\mathbf{R}_{\text{Rx}}\}} \mathbf{R}_{\text{Tx}} \otimes \mathbf{R}_{\text{Rx}}, \quad (2.3)$$

where \otimes denotes the Kronecker product and $\text{tr}\{\cdot\}$ stays for the trace of a matrix. The Kronecker channel matrix therefore becomes

$$\mathbf{h}_{kron} = \frac{1}{\sqrt{\text{tr}\{\mathbf{R}_{\text{Rx}}\}}} \mathbf{R}_{\text{Tx}}^{1/2} h_{iid} \mathbf{R}_{\text{Rx}}^{1/2}, \quad (2.4)$$

where H_{iid} denotes an $(n_R \times n_T)$ i.i.d. random fading matrix with full unity-variance and n_T and n_R denote the number of transmit and receive antennas respectively. The major drawback of the Kronecker model lies in its main assumption. It can only model channels with separable joint angular power spectra [25] where all transmit eigenvectors couple into all receive eigenvectors.

A novel approach for generating stochastic channel models based on information theoretic assumptions is given in [51]. The model maximizes the entropy of the channel and is therefore also referred as the *MaxEnt* model. It describes a way on how to generate a channel model based on the state of knowledge one has. This approach was also validated against measurements [52].

2.2.2 Deterministic (Ray-tracing) Models

Deterministic channel models try to describe the propagation in specific real world environments in a most accurate manner. They model the channel based on the basic wave propagation mechanisms and geometrical data of the specific environment of interest. The first ray-tracing models used a 2-dimensional approach where only the elevation was fully modelled, i.e. height information of buildings was included, for macrocellular environments. In a next evolution step people started to model propagation in horizontal plane only, combined with propagation in vertical plane only. Such models are referred to as being 2.5-dimensional models. Nowadays most

ray-tracing models model the full 3-dimensional space where also rays that get to the receiver by some mixture of horizontal and vertical propagation are included.

Ray-tracing models are very useful for cell planning applications. This is also their main field of application. Since they always reflect specific environments they are not that useful for testing of receive algorithms. Their dependency on highly accurate environmental descriptions like 3-dimensional maps limit their usage.

2.2.3 Geometry based Stochastic Channel Models

In GSCMs, it is assumed that each wave interacts at an IO and is propagated towards the receiver. In contrast to the ray-tracing models GSCMs do not rely on real world scenarios but generate the locations of the IOs according to stochastic rules. The rules are chosen in such a way that certain environments are characterized. Usually the parameters of the stochastic rules are obtained from measurement campaigns [23], [53].

The analysis of measurements has also shown that IOs are typically grouped within certain areas, corresponding, e.g., to groups of buildings or objects in a room. Such a spatially separable group of IOs is called a cluster. I use the following definition of a cluster:

Definition: *A cluster is a set of MPCs which are grouped together resulting in the same delay, DOA, and DOD statistics taken over the large-scale movement of the MT.*

In the literature slightly different definitions of a cluster can be found [5], [54], [53]. [5] defines a cluster as a group of waves whose delay, azimuth, and elevation at the receiver are very similar, while being notably different from other waves in at least one dimension. Additionally all waves inside a cluster must stem from the same propagation mechanism. The authors define therefore three kinds of propagation mechanisms resulting from different wave propagation effects: (i) Street-Guided Propagation, (ii) Direct Propagation - Over the Rooftop, and (iii) Reflection From High-Rise Objects - Over the Rooftop. This results in three different types of clusters which are used for a quantitative description of different propagation effects. The definition of different types of clusters based on the leading propagation effect seems useful for the classification of measurements but is of less interest for channel models. In [55] another definition of a cluster is given. A cluster is defined as a group of MPCs showing similar DOAs and DODs whereas the APS of the cluster is decreasing from the cluster's center to the outskirts.

Note that all these definitions are based on the evaluation of static measurements and therefore do not include any temporal constraints on a cluster. From my point of view it is more precise to define a cluster including its temporal behavior.

Clusters are an important propagation phenomenon which has to be taken into account by channel models. The authors of [56] have shown that channel models disregarding clustering effects overestimate channel capacity.

In the literature [6], [37] the term *scatterer* is often used for an IO which is somehow misleading. GSCMs are not limited to scattering processes. They cope with all the propagation effects and do not even distinguish between them. Therefore I prefer to call the points where MPCs interact interacting objects.

Most geometry based channel models [6], [37], [57] assume a single interaction of the MPCs on their way from the transmit to the receive antenna only. Nature is not bound to single interaction processes, however these models give good results for a lot of environments. Their drawback is that some propagation environments (e.g. indoor environments) cannot be modelled using single-interaction processes only. To avoid the limitations of single-interacting clusters people have started to include double-bounce paths in their models [42], [43]. Their drawback is the high complexity resulting from a multitude of possible MPCs. To overcome this limitation, I have introduced the twin-cluster in [58]. This approach broadens the common single-interaction models but does not increase the computational complexity. It will be discussed in more detail in Chapter 4.

2.3 Standardized Channel Models

There exist some standardized MIMO channel models nowadays in literature. The 3GPP standard has included the 3GPP spatial channel model (SCM) [59]. This is more or less a reduced version of the COST 259 channel model [6]. The COST 259 channel model itself is not really a MIMO channel model. It was originally designed for the smart antenna case with an antenna array only at one link end. From my point of view it can be applied to MIMO environments within some limitations². The COST 273 channel model is among the first models specifically designed for the MIMO channel including large-scale and small-scale effects of the channel. The COST 273 MIMO channel model is part of the COST 273 final report [60]. It is the basis of

²A more detailed description of the COST 259 channel model and its limitations is given in Section 2.3.2.

my channel model and I will give a short introduction on it in Section 2.3.4.

2.3.1 COST 207 and COST 231

COST is a European research initiative with a long tradition in channel modelling. The first COST research activity in the area of channel modelling was COST 207 [61] where models for the delay dispersion in cellular macrocells were derived. These models were instrumental for the development of the GSM system. The four models are called Typical Urban (TU), Bad Urban (BU), Hilly Terrain (HT), and Rural Area (RA). Their power delay profiles are given in Figure 2.3 and can still be found nowadays, e.g. in COST 259 [44]. The difference between a typical urban and a bad urban environment is the greater delay dispersion of the GBU environment which is established via a second, delayed cluster. COST 207 was active from 1984 till 1988. At this time people were mainly interested in macro cells for mobile communication systems. Therefore only macro cellular environments can be found within COST 207.

The successor of COST 207 was COST 231 [62]. In COST 231 pathloss model like the well known Hata-pathloss model [62], the Walfish-Ikegami model [62], or the Feuerstein model [63], [62] were standardized and extended to frequency ranges and environments (e.g., microcells) of interest to modern cellular systems. This work still serves as the basis for the pathloss of the COST 259 and COST 273 models.

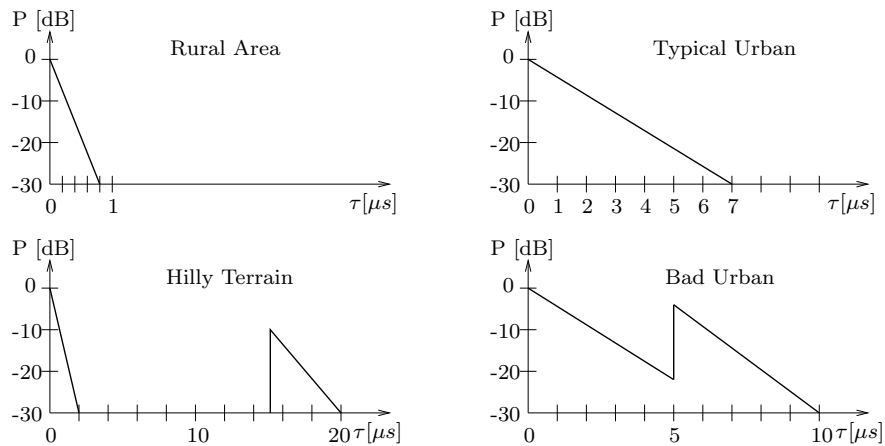


Figure 2.3: The power delay profiles of the four COST 207 macrocell environments.

2.3.2 The COST 259 Channel Model

COST 259 derived a model for the directional characteristics in macro-, micro- and picocells, and merged this with a description of the attenuation and delay dispersion that is more general than that of previous models. It is commonly known as *the COST 259 channel model* but in fact different modelling approaches were used for different cell types. If people talk about the COST 259 channel model they usually mean the COST 259 macro cellular model. In the following I will briefly describe the different modelling approaches. In accordance with the names of the COST 207 environments COST 259 has defined a name and a three letter abbreviation of all its environments. To stress the improvement of the model compared to COST 207 all the names start with the term *general* and all the abbreviations with a 'G'.

Macro cells

The principal idea of the COST 259 macrocell channel model is given in Figure 2.4. MPCs are grouped into clusters where the number and position of the clusters are selected according to probability density functions (PDF) depending on the specific environment. A local cluster around the MT exists all the time. Additional far clusters are placed inside the whole cell. These far clusters are only visible at certain MT positions. Therefore so called visibility regions of finite size, which are associated with specific clusters, are spread over the whole cell. If a MT is inside of such a region the depending cluster becomes visible. To avoid step functions of the signal level when a cluster appears or disappears transition regions are used. The size and number of visibility regions depends on the environment [64].

Based on the COST 207 propagation scenarios a set of four environments is defined: GTU–General Typical Urban, GBU–General Bad Urban, GHT–General Hilly Terrain, and GRA–General Rural Area. The distinction between GTU and GBU is mainly the number of far clusters which lead to a greater angular and delay dispersion for the GBU scenario.

Microcells

The COST 259 microcell approach is based on so called *virtual cell deployment areas* (VCDA). BS and MT are placed on artificially constructed maps which represent "typical" situations with streets and buildings and the MT follows predefined routes along the streets. The clusters are placed according to specific visibility rules based on the position of the MT. Slightly simplified one can say that clusters occur in all

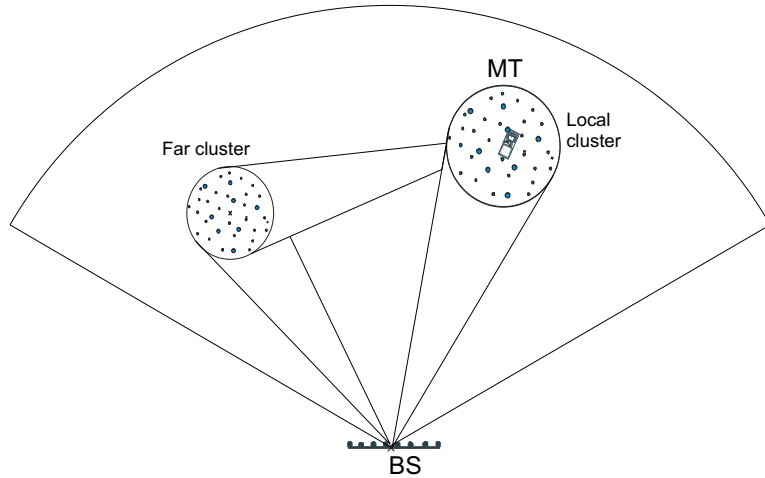


Figure 2.4: The COST259 macrocell approach.

the streets the MT can 'see'. These rules can be approximated using visibility regions as for the macro cells or simple geometric considerations. A set of 4 environments is specified: GSX–General Street Crossing, GSL–General Street LOS, GSN–General Street NLOS, and GOP–General Open Place. A discussion on the implementation of this model and its features and drawbacks can be found in Section 4.2.2.

Picocells

As for the microcell environment a VCDA is defined covering typical European buildings. The picocell environment covers the five scenarios GOL–Large Office or conference/meeting room with LOS, GON–Small Office NLOS, GCL–Corridor LOS, GCN–Corridor NLOS, and GFH–Factory/Hall.

2.3.3 The 3GPP/3GPP2 Spatial Channel Model

The 3GPP/3GPP2 spatial channel model (SCM) [59] is a stochastic tapped delay line channel model based on paths with certain power, DOA, DOD and delay. The received signal at the MT consists of 6 time-delayed multi-path replicas of the transmitted signal. Each path consists of 20 subpaths that have different angles of arrival. There exists a defined list of 13 to 19 steps for each environment describing the modelling process of the channel in detail.

The SCM covers three simulation environments: suburban macro, urban macro, and urban micro. All the paths belong to the same, single local cluster with the

exception of the urban macrocell environment where two paths belong to a far cluster to represent the bad urban case. This bad urban environment is selectable among the urban macrocell scenario and represents a case with increased delay spread of the signal. Other selectable features of the SCM include polarized antenna arrays, a LOS scenario for the microcell environment and an urban street canyon scenario. In addition to the pure link-level capability a simplified approach for the modelling of intercell interference is described where a set of the strongest interfering sectors is modelled as spatially correlated processes and weak interferers are modelled as spatially white Gaussian noise processes.

The SCM is a stochastic channel model which contains some properties of the GSCMs. However, there is no location of IOs, and the DOAs and DODs are stochastically paired. Therefore I count it still as a stochastic channel model.

2.3.4 The COST 273 Channel Model

COST 273 is the successor of COST 259 and also the COST 273 channel model is based on the COST 259 macro cellular model, which is described in [6] and in greater detail in [65] and [66]. It is a full MIMO channel model based on the analysis of MIMO measurements. The COST 273 model uses the same generic channel model for all types of environments. This is an important distinction to the COST 259 model, which used different generic models for macro-, micro- and picocells. While such an identical generic model might not result in the most accurate modelling structure, it is a great simplification for the actual implementation. In the following I will briefly describe the most important features of the COST 273 channel model.

The model defines a set of the 7 mandatory environment³ out of a total set of 22 environments where I introduce 3-letter abbreviations for the environments for an easier distinction. These mandatory COST environments are also the basis for the parametrization of my model.

COST 273 Environments

1. **SMC**: Small macrocells in city center; describes densely built-up areas with a homogenous building structure.
2. **LUM**: Large Urban Macrocell; this environment is comparable to the COST

³In COST 273 mandatory scenarios are defined as scenarios mandatory for system tests, while the other ones are optional. The set of the 7 mandatory scenarios covers the most important environments.

259 GTU environment and describes densely built-up areas. The BS is far above rooftop level.

3. **OIU**: Outdoor-to-indoor urban; this environment is similar to the small macrocells in city centers, but the mobile station is in an indoor, NLOS location.
4. **MCC**: Microcell City Center; the environment is defined similar to the urban environment but the BS height is at or below the level of the surrounding rooftops.
5. **POL**: Office LOS; this is an office environment where the BS and MT have LOS. A modern concrete/steel/glass building structure is assumed.
6. **PON**: Office NLOS; like the POL environment but without an LOS. BS and MT might be in different rooms.
7. **PCH**: Halls; this environment covers big indoor areas like railway stations, airport halls, and factory halls.

The principal idea of the COST 273 channel model is to model the mean angles and delays of the clusters by geometric considerations, while the intra cluster spreads and the small-scale fading can be represented by either a geometrical approach, or a tapped delay line representation. Also this philosophy is similar to the COST 259 model. The COST 273 model distinguishes between MPCs with only one interaction on their way from the transmitter to the receiver and multiple interacted waves. To cope with the wide range of scenarios, the COST 273 model includes three kinds of clusters: local clusters around BS and/or MT, clusters incorporating single interaction, and finally I introduced the twin-cluster concept allowing for multiple IOs. Not all kinds of clusters are mandatory for all scenarios. In macrocells the single interaction cluster is the dominant propagation mechanism whereas in indoor environments multiple interaction processes account for most of the energy of the arriving radiation. The model finally specifies a *selection parameter* K_{sel} that gives the ratio of single-interaction to multiple interaction additional clusters. Since no measurements were available, this parameter was put to unity in macrocells, to 0.5 in microcells, and to zero in picocells. Local clusters show always pure single-interaction behavior. This cluster structure is also the basis for my channel model and is discussed in more detail in Section 4.

2.4 Antenna Arrays and Polarization

The usage of space diversity in the reception of mobile radio signals is a well known technique to mitigate fading. During the last few years the interest in dual polarized antennas for mobile communication systems increased. Using dual polarized antenna elements results in more or less uncorrelated receive signals [67] while keeping the receive unit small. This is very important for small mobile devices. In order to simulate systems exploring polarization diversity, channel models are required that cope with dual polarized radiation. The effect of depolarization can be described using the well known cross polarization discrimination (XPD) coefficient

$$XPD = \frac{P_{VV} + P_{HH}}{P_{VH} + P_{HV}}, \quad (2.5)$$

where P_{VV} denotes the power of the vertically co-polarized components and P_{VH} the power in the cross polarized components from vertical polarization to horizontal polarization.

To gain more information on the polarization behavior of the radio channel, antenna arrays using dual polarized antenna elements were designed for channel sounder measurements. In [68] a spherical antenna array looking like a football is described which allows dual polarized measurements. Using such spherical antenna designs allows for investigation of propagation effects in azimuth and elevation. In [69] other dual polarized antenna arrays are discussed. All these arrays are designed for measurement purposes. Their major goal is to allow a detailed characterization of the air interface. Therefore up to 64 antenna elements [70] are used for one array. Dual polarized antennas for mobile devices are, for example, shown in [71, 72]. A cubic antenna array exploiting space and a combination of polarization and pattern diversity is discussed in [73].

To include polarization on the model, let us first assume that the transmitter emits vertically polarized MPCs only. The MPCs interact with the IOs and become attenuated and depolarized. The same occurs for horizontally polarized MPCs as well. The complex amplitudes \mathbf{a}_s of the MPCs can therefore be written as 2×2 polarimetric matrices [24]

$$\mathbf{a}_s = \begin{bmatrix} a_{VV,s} & a_{VH,s} \\ a_{HV,s} & a_{HH,s} \end{bmatrix}, \quad (2.6)$$

where the entries of the matrix describe the four possible polarization combinations of the MPCs.

Another important topic for channel models are the antenna arrays and their imperfections. Using real antenna elements with non-isotropic antenna patterns yields a weighting of the MPCs according to their DODs and DOAs. (2.1) can be redefined by introducing the spherical complex (amplitude) antenna patterns $\Omega_{\text{DOA}}(\varphi_{\text{DOA}}, \vartheta_{\text{DOA}})$ and $\Omega_{\text{DOD}}(\varphi_{\text{DOD}}, \vartheta_{\text{DOD}})$ for the transmit and receive antenna elements, resulting in

$$h_{n_T, n_R}(t, \tau) = \sum_{s=1}^S |h_s| e^{j\phi_s} \Omega_{\text{DOD}}(\varphi_{\text{DOD}, s}, \vartheta_{\text{DOD}, s}) \Omega_{\text{DOA}}(\varphi_{\text{DOA}, s}, \vartheta_{\text{DOA}, s}), \quad (2.7)$$

where the impulse response is now antenna element specific and the antenna patterns replace the Dirac functions.

Not only IOs are new point sources in space but also all antenna elements. This results in the well known coupling between the elements of the array. The end-to-end impulse response \mathbf{h}_C , which includes the antenna coupling, is given by

$$\mathbf{h}_C = \mathbf{C}_{Rx} \mathbf{h} \mathbf{C}_{Tx}, \quad (2.8)$$

where \mathbf{C}_{Tx} and \mathbf{C}_{Rx} denote the array coupling matrices [74] at transmit and receive side, respectively.

Chapter 3

MIMO Channel Measurements

The radio channel is the only part of each wireless system which is given by nature and cannot be changed. Each standard and system has to adapt to the properties and limitations of the radio channel. To ease the development of new systems, appropriate channel models are required which reflect all the properties and limitations of the wireless channel. For the design of such realistic models the understanding of the wireless channel is essential. Channel measurements are the best way to exploit the nature of the wireless propagation channel. A direct measurement of the propagation channel is not feasible but the whole radio channel, including the antenna arrays and the imperfections of the measurement hardware, can be measured. This means that the measurement itself has influence on the results of any parameter extraction obtained from measurements. For example, antenna arrays can usually not measure the full 3-dimensional space including both polarizations. The, for measurement purposes, quite usual uniform linear arrays (ULA) are not able to cope with the elevation (if oriented in azimuth direction) and polarized patch antennas can not observe the full radiation sphere. All this limitations are drawbacks of the channel measurements but shall not limit the importance of such measurements for algorithm and system design.

In the following I will describe the hardware I have used for my measurement campaigns and describe the way I have measured including the selected measurement environments. In the end of this chapter I will show some measurement evaluations which are useful for the parametrization and evaluation of my channel model.

3.1 Measurement Equipment

For my investigations I have used measurement equipment from two companies, namely Medav [8] and Sintef [75]. Both channel sounders are able to measure the double directional channel and measure in a bandwidth of 100 MHz. In the following I will introduce the measurement principle, which is very similar for both sounders, and describe the features of the two models.

3.1.1 Measurement Principle

Measuring a $m \times n$ MIMO channel requires to measure the transfer function between all combinations of transmit and receiver antennas. This can be done in a serial or parallel manner. Measuring all channels in parallel has the advantage that synchronization is less critical. On the other hand it requires much more hardware (one transmit chain for each transmit antenna and one receive chain per receive antenna). An additional drawback is the reduction in SINR at the transmit side. Measuring in parallel requires differently coded (preferably orthogonal) transmit signals for all antennas. The loss in SINR is due to the imperfect cross- and autocorrelation characteristics of that signals. It is, of course, possible to find orthogonal sequences at the transmitter but due to the multi-path propagation and resulting inter-symbol-interference the sequences do not remain orthogonal at the receiver. Parallel sounding at the receiver actually improves the SNR, because one gets rid of the attenuation of the switches.

In addition very stable transmit and receive chains are needed. A phase drift between the power amplifiers of two transmit antennas during the measurements makes DOD estimation nearly impossible whereas a phase shift at the receive side prohibits DOA estimates.

Nowadays most commercially available products use a serial measurement principle, with a single TX and RX chain, where each antenna combination is measured after each other. For this measurement principle it has to be assumed that the channel is constant during the time interval of one complete MIMO measurement to correctly measure the channel. If I assume a measurement duration of a single antenna link of $5 \mu\text{s}$, which corresponds to a maximum path delay of 1500 m ¹, a set of 15 transmit and 8 receive antennas takes $15 \times 8 \times 5 \mu\text{s} = 600 \mu\text{s}$ of measurement time at minimum.

¹A maximum path length of 1500 m sounds very short but due to the power limitations of such equipment (maximum of 2 W spread over about 100 MHz) the range of the equipment is limited as well.

Assuming that the time required for switching the RF chain from one antenna to the next is also 5 microseconds, the required measurement time is doubled.

The antenna multiplexing for a MIMO snapshot is given in Figure 3.1 for a measurement setup of eight receive elements and 15 transmit elements. This is a typical setup for most of my measurements. Starting with the first Tx and Rx antenna the Rx antennas are switched on a fast time scale whereas the Tx antennas are switched with lower frequency. Figure 3.1 also shows the guard intervals between the measurements. These guard intervals are of the same duration as the measurement intervals to allow for an easy switching scheme with one clock providing the timing for the multiplexers.

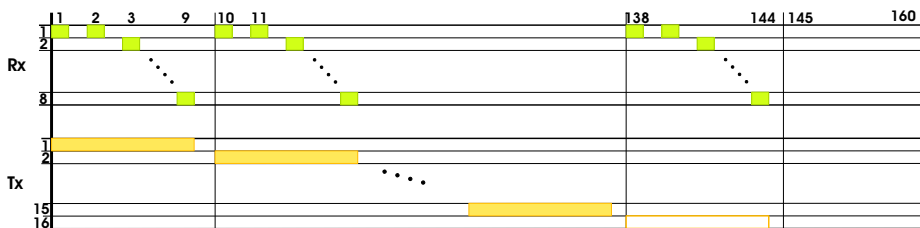


Figure 3.1: Channel multiplexing.

Synchronization

For the measurements transmitter and receiver are typically not connected to each other. A cable connection would limit the flexibility during measurements a lot. First, the maximum measurement range is limited to the length of the synchronization cable and second dynamic measurements with a fast moving transmitter are nearly impossible. For measurements in public areas additional people are required for the measurement campaigns how take care of such a synchronization cable. Therefore usually heated Rubidium clocks are used for synchronization of the terminals. In the case of the Sintef channel sounder they are assisted by a GPS clock. For the RUSK ATM the two Rubidium references have to be adjusted to each other in the beginning of each measurement day. Since synchronization between the two clocks is never perfect the receiver will slightly drift away from the transmitter clock resulting in a drift of the delay of the measured channel. I typically observed a drift of about

$1 \mu\text{s}$ within 8 hours of measurements². Therefore there is no absolute time reference for the measurement evaluation and the distance between transmitter and receiver may not be computed using the delay information of the measurement data.

3.1.2 Medav RUSK-ATM Channel Sounder

Medav is a well known company in the field of channel sounding and their MIMO capable RUSK-ATM Vector Channel Sounder is a state-of-the-art equipment. I have performed measurements at a center frequency of 2 GHz and for some additional measurements a center frequency of 5.2 GHz was used. The equipment consists of a mobile transmitter and a more or less fixed receiver, acting as a base station (Figure 3.2). The individual channel transfer functions between all pairs of transmitting

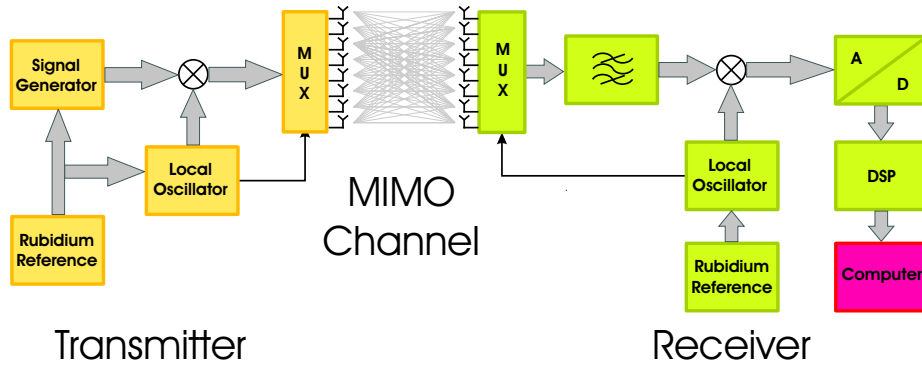


Figure 3.2: Channel sounder block diagram.

and receiving antenna elements are measured over a total bandwidth of 120 MHz. The transmit signal is a multitone signal with constant envelope. In the receiver the input signal is filtered and correlated with the transmitted one using a DSP resulting in the specific transfer functions. The signals are then stored in the frequency domain.

The measurements between all pairs of elements are multiplexed in time: every channel impulse response is recorded over a duration of $3.2 \mu\text{s}$. The time over which the impulse response is recorded may differ for some measurement runs within a range of 0.8 to $6.4 \mu\text{s}$ depending on the demands of the specific scenario, whereas $0.8 \mu\text{s}$ was used for indoor measurements only. To ensure correct switching of the antenna multiplexors the first receive element is measured twice to ensure that the correct antennas

²The actual version of the Medav sounder seems to have much more precise clocks which preserve the absolute time reference.

are measured. This principle can be exploited during the evaluation of the measurement data to check if the multiplexers worked properly. As long as synchronization is correct the first two receive signals have to be the same. Furthermore, the 16th transmit antenna port of the transmit multiplexer is terminated with $50\ \Omega$ resulting in an additional noise measurement for each snapshot.

The transmit power of the channel sounder is 2 W in the 2 GHz band and 0.5 W for the 5.2 GHz equipment. The power can be reduced by using a 20 dB attenuator for indoor measurements. A power of 2 W sounds quite a lot but since the power is spread over 120 MHz the range of the equipment is limited to some 100 m in urban areas due to the noise power collected over the whole bandwidth. The limiting factor for the transmit power are the PIN-diode switches of the transmit multiplexer.

Measurement Setup

I was using the equipment for three types of measurements:

- measurements with an omni-antenna at one link end and a physical array at the other link end (SIMO measurements),
- measurements with physical arrays at both link ends (MIMO measurements), and
- measurements using a positioning table to create a virtual array at one link end.

For all measurements the smaller transmit unit was chosen as the moving part (MT) whereas the receiver acted as the fixed BS.

SIMO measurements The principle of the SIMO measurements is shown in Figure 3.3. A single transmit antenna transmits the reference signal continuously. At the receiver the antenna elements of the receive antenna array are connected to the channel sounder via a multiplexer. The receive signal is bandpass filtered, downsampled, analog–digital converted, and stored on a computer.

MIMO measurements This measurement setup is an extension of the SIMO case. Additional hardware is required for the switching of the transmit antenna array (Figure 3.2). As mentioned above, the measurement does not take place continuously, a starting time for the transmitter and the receiver for a MIMO snapshot has to be

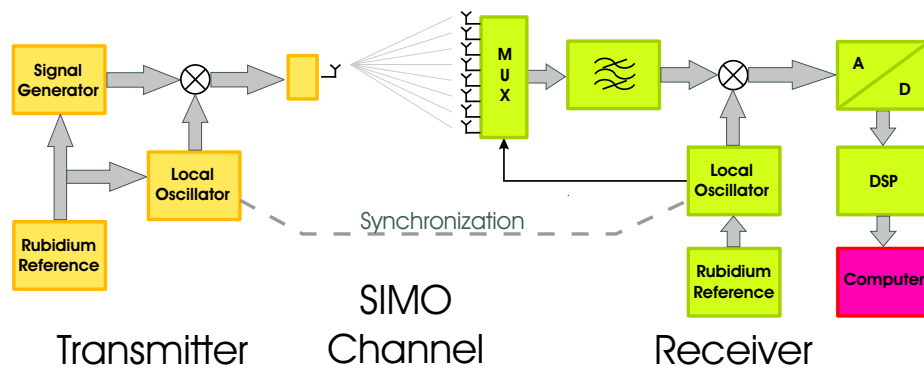


Figure 3.3: SIMO measurement mode

defined. For this purpose a second clock of about 3 kHz is used. This clock is synchronized to the Rubidium references. The second time normal drives the additional hardware which ensures the proper multiplexing of the antenna elements.

Like the SIMO measurements, transmitter and receiver have to be synchronized at the beginning of a measurement day. A typical measurement setup is shown in Figure 3.4 and 3.5 for the transmit and receive side respectively.



Figure 3.4: The RUSK-ATM transmitter mounted on a trolley.

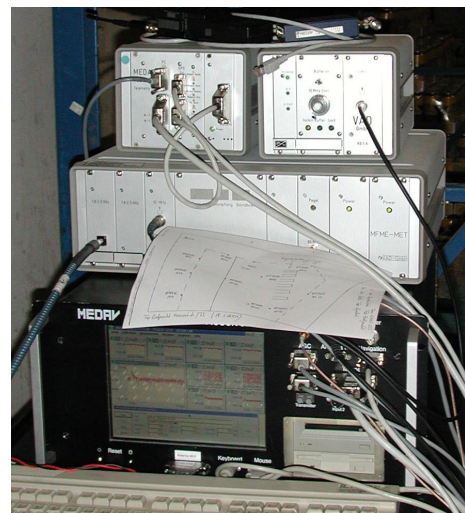


Figure 3.5: The RUSK-ATM receiver acting as the BS.

Measurements using the positioning table Antenna arrays are a very expensive component of a channel sounder. One alternative is a single, omnidirectional antenna element mounted on a positioning equipment. I have used a positioning table allowing for arbitrary movements of the antenna on a horizontal plane of about $80 \times 80 \text{ cm}^2$. This allows to create a virtual array. The clear drawback of such equipment is the the long time (on the order of several minutes) it takes to measure one MIMO snapshot. Therefore one is limited to static environments. On the other hand this equipment allows to create different array geometries (note that the antenna geometry is fixed). One can even measure array geometries that could not be realized with real antennas due to the physical dimensions of each antenna element. I have performed measurements with up to 1000 elements and antenna spacings down to 5 mm. Such measurements last for about 40 minutes. One additional advantage is the lack of mutual coupling in between adjacent antenna elements.

The used positioning table is shown in Figure 3.6. Due to the size and material of the table additional shielding of the ground plane of the table is required since the table itself may influence the environment. I have adapted the table by placing plates of absorption material around the antenna to at least exclude ground reflections on the table itself.

SIMO and MIMO measurements do not need a wired link between transmitter and receiver. A link between Tx and Rx is essential for the measurements with the table to synchronize transmitter and receiver and to operate the table itself.



Figure 3.6: The positioning table with one omni-directional antenna on top.

Antennas

The antennas are one, or maybe even the most important part of channel sounder measurements. Their design defines the characteristic of the measurement. The goal of the measurements is to explore the spatial structure of the channel and therefore multiple antenna elements are needed. For measurement purposes the size of the array does not matter (at least for center frequencies from 2 GHz onwards) whereas the array size for user equipment is one of the limiting factors for the application of antenna arrays. In combination with the RUSK-ATM three different antenna arrays were used:

Omnidirectional Tx-/Rx-antenna This antenna has a gain of about 3 dBi in the azimuthal plane. It is mainly used for the SIMO outdoor measurements during my first measurement campaign³ and as transmit antenna for the measurements using the positioning table. It is shown in Figure 3.7.

Circular 15 element Tx-array The circular array (Figure 3.8) is especially designed for the purposes including high speed measurements on a racing track. It consists of 15 monopoles spaced 0.43λ apart and mounted on a very stable ground plane and is shown in Figure 3.8. The antenna was manufactured by Fa. Krenn [76] under the supervision of Univ. Prof. Arpad Scholz from Vienna University of Technology.

Linear eight element patch array The array was provided by T-Nova, Deutsche Telekom. It consists of eight single polarized patches with a spacing of $\lambda/2$ at the center frequency of 2 GHz. The antenna is vertically polarized and has an aperture of about 120° in azimuth and 60° in elevation. It is shown in Figure 3.9.

3.1.3 Sintef Channel Sounder

In addition to the measurements with the RUSK ATM in Vienna I have carried out a measurement campaign in the Oslo region using the SINTEF channel sounder. These measurements were conducted as part of the EU-IST project FLOWS [77].

The measurement principle of the Sintef sounder is very similar to the RUSK-ATM and I therefore limit this section to a description of the differences of the two devices.

³During the first measurement campaign MIMO measurements were only possible using a wired link between transmitter and receiver. An improved version of the channel sounder enabled MIMO measurements without a wired connection for all later campaigns.



Figure 3.7: The omni-directional transmit and receive antenna.



Figure 3.8: The circular transmit antenna array.



Figure 3.9: The linear receive antenna array.

SINTEF Telecom and Informatics in Trondheim, Norway, manufactured the channel sounder on assignment from Telenor R&D in 2001. It consists of one transmitter part and one receiver part that can be placed arbitrarily apart from each other. The channel sounder operates at either 2 GHz or 5.2 GHz with a bandwidth of up to 100 MHz. As transmit signal a chirp with variable length is used and the transmit power is up to 2 W. For the measurements it was reduced to 0.5 W (27 dBm) due to limitations of the transmit antenna multiplexer. The real part of the chirp sequence in the base band is shown in Figure 3.10. The sequence has a length of 512 symbols and consists of one or several chirp sequences. One chirp sequence has a length of 256 symbols. To realize larger sequence lengths several chirps may be transmitted one after each other. In order to achieve a smooth transition, every second chirp is time-inverted (mirrored). In Figure 3.10 the total chirp signal consists of two identical copies of one sequence where the second one is mirrored. The principle of the Sintef

channel sounder is shown in Figure 3.12 for the transmit part and in Figure 3.11 for the receive chain.

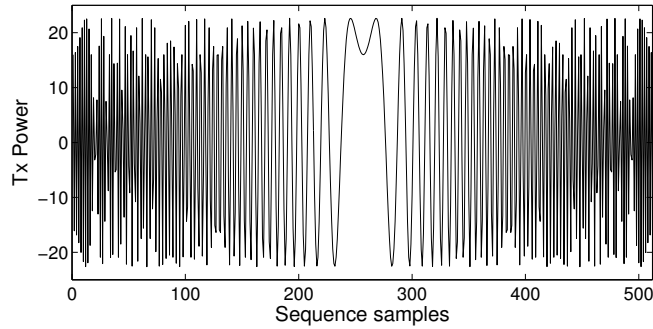


Figure 3.10: Measurement chirp of the Sintef channel sounder.

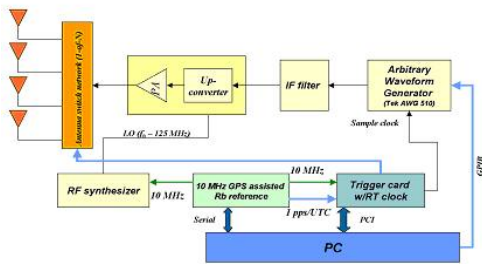


Figure 3.11: The measurement principle of the Sintef channel sounder, Tx part.

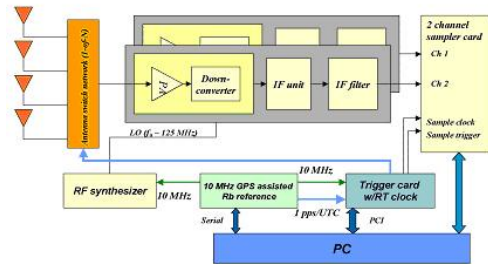


Figure 3.12: The measurement principle of the Sintef channel sounder, Rx part.

The receiver is equipped with two parallel receiver chains. For my measurements, only one of them is used. During the measurements, the transmitter is the stationary part (BS). For the indoor measurements the receiver (MT) is put on a lab trolley while in the outdoor case it is vehicle mounted. In the latter case power is provided from a battery bank via a DC-AC converter.

Synchronization

Since the Sintef sounder uses GPS support for the Rubidium clocks frame synchronization is based on the GPS signal as well and no frame synchronization clock is

needed. To start a MIMO measurement transmitter and receiver have to be set by hand to the same starting time. The measurement itself starts automatically at the given time stamp. This is somehow more difficult than with the RUSK-ATM where a measurement can be started at any time without inputs at the transmit side. Sometimes this system leads to failures due to a misunderstanding over the walkie-talkies of the people operating transmitter and receiver.

Antennas

8 Element Dual Polarized Patch Array This antenna acts as the receive antenna array and is an 8 element uniform linear array (ULA). The center frequency is 2.1 GHz and each element has a bandwidth (VSWR < 2.0) of 330 MHz ($\sim 15\%$) [78]. Each element is a rectangular patch and has two ports, one for each polarization. Typical element diagrams (E- and H-plane) are shown in Figure 3.13. They also show that the 3 dB beam width is approximately 80° ($\pm 40^\circ$). The diagrams also show the cross polar discrimination.

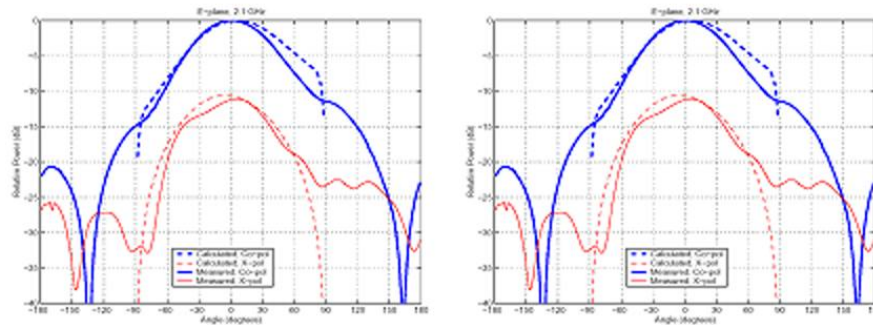


Figure 3.13: The patch element diagrams of the Rx antenna. Left: E-plane diagram. Right: H-plane diagram [78].

It limits the usable sector to less than 180° because of reduced signal to noise ratio at large angles. The element spacing is 71.4 mm corresponding to 0.5λ at 2.1 GHz. Because each element has two ports, the array in total has 16 ports which can be connected arbitrarily to a 1-of-8 multiplexing network. For all the measurements the 4 center elements are used with both polarization ports connected. In this way, it is possible to investigate the effects of polarization on the performance. The specification for the coaxial switches used in the multiplexing networks made it necessary to limit

the transmit output power to 0.5 W (27 dBm). A photo of the antenna is shown in Figure 3.14.

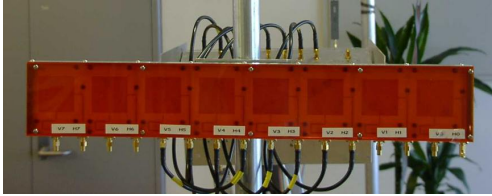


Figure 3.14: The Rx antenna.



Figure 3.15: The Tx antenna.

8x4 Elements Planar Array The transmit antenna follows the same concept, but this is a planar array organized as a matrix, i.e. with 8 elements horizontally and 4 vertically, giving a total of 32 elements. The elements are identical to the ones of the receive array, however the element spacing is slightly different: 73 mm (0.51λ). The individual ports of the antenna elements are not available on this antenna. A duplicated multiplexing network is integrated giving access to the multiplexed signal from both polarizations. This means that only one polarization can be measured at a time. For the measurements, only vertical polarization is investigated. The transmit antenna is mounted on a tripod as shown in Figure 3.15.

Antenna multiplexing

In order to be able to analyze the data correctly, knowledge about the multiplexing order of the antenna arrays is necessary. The receive antenna is connected using the 4 center elements with both polarizations. The multiplexing order is the following, when referring to the labelling in Figure 3.14, i.e. from right to left (front view)⁴:

$$H2 - V2 - H3 - V3 - H4 - V4 - H5 - V5.$$

The transmit antenna uses all elements and is multiplexed row-wise. The rows are numbered A, B, C and D, and the elements in each row from 1 to 8, as shown in Figure 3.16.

⁴The antenna numbering starts with zero.

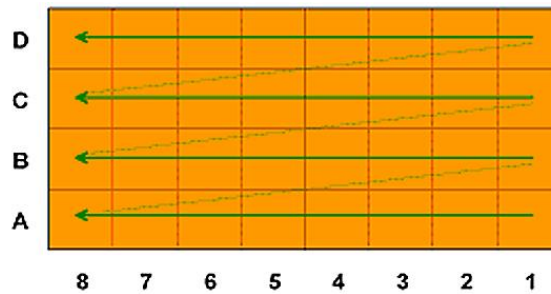


Figure 3.16: The transmit antenna multiplexing scheme.

Measurement Setup

In contrast to the RUSK-ATM the receiver of the Sintef sounder is always the moving part. This setup facilitates the documentation of the measurements since most measurement parameters vary due to the movement of the mobile part and can be documented by the same people as who perform the measurements. In principle it is possible to perform the measurements the other way round as well, but the measurements with the RUSK-ATM have shown that a moving receiver is beneficial. The measurement setup for the 2 GHz case is shown in Figure 3.17. The transmitter is mounted inside a car (Figure 3.19) for the urban area measurements and on a small laboratory trolley for the indoor measurements whereas the receiver is always mounted on a big trolley (Figure 3.18). The picture shows also 3 colleagues from Telenor who helped with the measurements. In the outdoor case, power is provided from a petrol-powered generator which is lighter than the set of batteries of the RUSK-ATM and allows for longer measurement days.



Figure 3.17: The Sintef transmitter acting as an indoor base station.



Figure 3.18: The Sintef receiver mounted on a trolley for outdoor measurements.



Figure 3.19: The transmitter of the Sintef channel sounder mounted inside a car. The photo shows the measurement setup for an urban microcell.

3.2 Measurement Scenarios

The measurement equipment described in the previous section was used for several measurement campaigns in various environments. I have picked out a subset of these measurements for the evaluations given in the next section. The chosen environments are described in more detail in the following including a rough classification according to the COST 273 environments (Section 2.3.4).

3.2.1 Suburban area - Weikendorf measurements

About 50 km north of Vienna I found a suburban area at the village of Weikendorf. The measurement area covers one-family houses with private gardens around them. The houses are typically single-storey buildings. Such an area is typical for small villages around Vienna. In addition there is a rail track in this area, which intersects the region of single placed houses. To get a typical BS position I have used a lift to wind up the receiver to a height of about 20 m which is much higher than anything in the surroundings. Therefore the probability for the occurrence of an LOS component is very high. The most interesting measurement run within this area includes a walk through a small pedestrian tunnel below the railway. By entering the tunnel the propagation paths will change significantly. A map of the scenario is given in Figure 3.20 where the receive position is called *RC* and the measurement runs are numbered from 37 to 47. A view from the receiver towards the tunnel is given in Figure 3.21 where also the start and stop position of route 46 (route through the tunnel) are marked.

3.2.2 Urban area - Oslo Kvadraturen

This site is in a part of Oslo with a regular street grid. The building mass is homogenous and materials used are mostly brick and concrete. Some of the buildings are quite old. The building height varies from 20 to 30 m. The area is often referred to as "Kvadraturen". Measurements at this site were taken twice, once with the receiver antenna at street level (BS height 2 m) and once with the antenna at rooftop level on top of a hotel building (BS height 25 m). Thus, these two antenna positions will cover typical micro cellular BS scenarios. According to the COST 273 specification this area classifies for the SMC and LUM environments for the high BS position and the MCC environment for the low BS position. Some impressions of the area are given

in Figure 3.22 including the view in the direction of the maximum of the antenna pattern from the roof level position and a view at street level. The measurement routes used are shown on the maps in Figure 3.23.

3.2.3 Picocell Indoor - Telenor Headquarter Fornebu

The new Telenor headquarter located in Fornebu, west of Oslo, is a modern office building with open indoor areas. The building materials used are mostly glass and steel. Floors are wood covered computer floors or stone tiles. There are very few cubicle offices, but work zones with large open spaces are used. The building has an irregular structure.

For the first indoor campaign the transmitter was placed inside the office area (Figure 3.24) at a height of about 2m above the floor and the receiver was moved around the corridors on the same floor. The whole set of measured paths is shown in Figure 3.25. In accordance to the COST 273 specification this area covers the POL and PON environments.

In addition to this office environment, measurements in a large atrium area were conducted. The atrium is a metal and glass covered hall, seven floors height. It also has similarities with a hall in an airport or a modern shopping area and qualifies for the PCH environment of COST 273. Measurements were performed on different floor levels. The measurement routes are shown in the map in Figure 3.26, while a cross section drawing is shown in Figure 3.27. Figure 3.28 shows a photo of the receiver position.

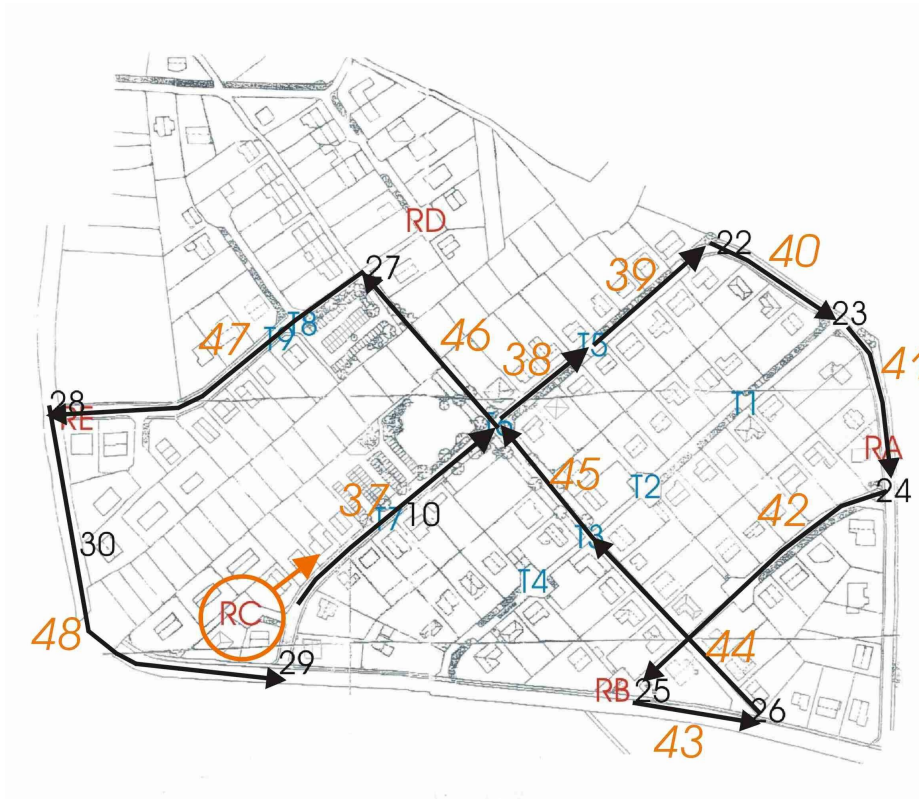


Figure 3.20: Map of the Weikendorf measurement area.



Figure 3.21: The BS view at the Weikendorf scenario.



Figure 3.22: The Kvadraturen measurement area: a view from the BS and the area at street level.



Figure 3.23: Measurement routes at Kvadraturen.



Figure 3.24: Photo of the office area at Fornebu.



Figure 3.25: Map covering all measurement routes of the office area.

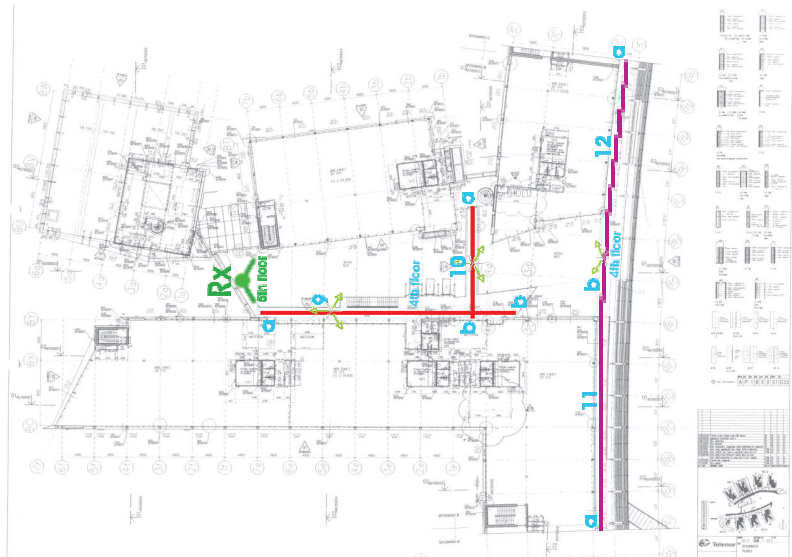


Figure 3.26: Map of the measurement routes for the atrium measurements

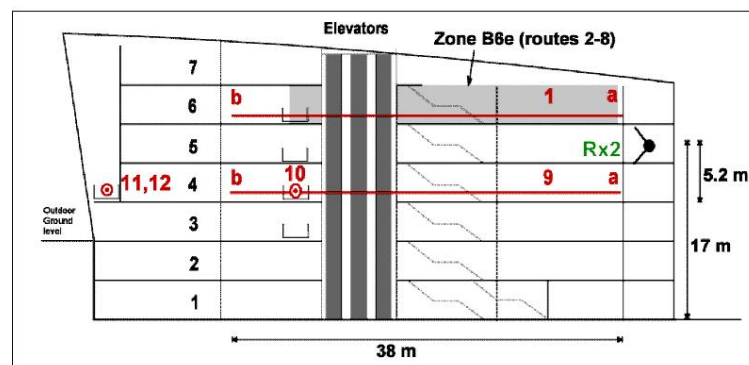


Figure 3.27: Cross section drawing of the atrium area including the measurement routes.



Figure 3.28: Photo of the atrium area.

3.3 Measurement Evaluation

The major part of my thesis is the MIMO channel model I will introduce in Chapter 4. Therefore I will investigate in this section in some channel measures relevant for my channel model. In the following I will evaluate the MIMO mutual information and the large-scale properties of some of my measurements. My channel model is one among very few which can deal with large-scale movements of the MT and therefore the validation of this behavior is of special interest.

3.3.1 Mutual Information

The information theoretic MIMO capacity[79] for the flat fading MIMO channel is defined by the well known equation

$$Cap = \mathbf{E} \left\{ \log_2 \left[\det \left(\mathbf{I}_{n_R} + \frac{\rho}{n_T} \mathbf{h} \mathbf{h}^H \right) \right] \right\}, \quad (3.1)$$

where $\mathbf{E}\{\cdot\}$ defines the expectation over the ensemble, \mathbf{I}_{n_R} denotes a diagonal matrix of size $n_R \times n_R$ and n_R is the number of receive antennas. ρ denotes the signal to noise ratio, n_T is the number of transmit antennas and finally \mathbf{h} describes the transfer function of the channel having dimension $n_R \times n_T$ which has to be normalized to ensure the correct SNR. A requirement for calculating the MIMO capacity is the full knowledge of the statistics of \mathbf{h} . Information theoretic MIMO capacity is defined as the **expectation** of the logarithm of the determinant of the channel impulse response. This full knowledge on the statistics of the channel can usually not be obtained from measurement data. Since the full information of the channel is not available averaging over different spatial measurement points, and/or temporal measurement points is a common solution

$$C = \frac{1}{K} \sum_{k=1}^K \left\{ \log_2 \left[\det \left(\mathbf{I}_{n_R} + \frac{\rho}{n_T} \mathbf{h}(k) \mathbf{h}(k)^H \right) \right] \right\}, \quad (3.2)$$

where K denotes the number of samples of the channel matrix. It has to be ensured that the second-order statistics (in the case of Gaussian channels), or second-and-higher order statistics (for non-Gaussian channels) of the channel do not change over the different measurement points [80].

The size of the measurement area that is used for obtaining the ensemble is crucial. Choosing it too small, the number of measurements is insufficient; choosing it too large, one violates the stationarity assumption. [4] proposes the local region

of stationarity (LRS) as an abstract region of movement for the MT, where local stationarity of the channel holds approximately, and it is entirely defined upon measurement data. The LRS ranges from 2 to 20 m for outdoor environments [4]. In indoor environments it will be about 0.5 m [12].

The estimate of the MIMO capacity will always remain an estimate based on limited information of the channel. I therefore prefer, in consonance with [81] (page 72 and 155), the term *mutual information* to describe the estimate of the MIMO capacity obtained from measurement data. For the frequency selective case (3.2) can be extended using an OFDM like scheme, as Shannon has shown. The mutual information for frequency selective channels yields

$$C = \frac{1}{B} \frac{1}{K} \sum_{b=1}^B \sum_{k=1}^K \left\{ \log_2 \left[\det \left(\mathbf{I}_{n_R} + \frac{\rho}{n_T} \mathbf{h}(k, b) \mathbf{h}(k, b)^H \right) \right] \right\}, \quad (3.3)$$

where B denotes the number of carriers in frequency domain and $\mathbf{h}(k, b)$ is the frequency selective transfer function. Equation (3.3) (and also Equation (3.2)) calculates the mean mutual information of the MIMO channel. It also is approximately (depending on the channel statistics) the 50% outage capacity as introduced in [2]. The outage capacity describes the minimum capacity achieved in $x\%$ of all cases where x denotes an arbitrary chosen number. Typical values for the outage capacity are the 99% outage capacity and the 95% outage capacity. The relative capacity increase of MIMO systems compared to single antenna systems for the outage capacity is typically higher than the one for the mean capacity values since multiple antennas make the system more robust against fading dips. This effect is also visible in the CDFs of the capacity where curves for higher numbers of antenna elements become steeper. For the illustration of the capacity [2] uses complementary cumulative distribution functions (CCDFs) whereas I prefer CDFs for the visualization of the capacity.

In [82] a strategy is described on how to calculate mutual information based on a single measurement snapshot. It is based on the extraction of the MPCs and adds random phases to all paths for achieving different realizations of the channel. The accuracy of this method strongly depends on the accuracy of the path estimates. Furthermore, components like diffuse scattering [83] can not be taken into account. This method gives good estimates of the mutual information if only static measurement samples of the channel are available. If dynamic measurements with a moving MT are possible I prefer to estimate the mutual information via averaging over several snapshots within the LRS. In the following I will describe the influence of the

measurement noise.

The Impact of Measurement Noise on the Mutual Information

Every measured impulse response $\tilde{\mathbf{h}}$ covers not only the information on the channel \mathbf{h} but also some measurement noise \mathbf{n}

$$\tilde{\mathbf{h}} = \mathbf{h} + \mathbf{n}. \quad (3.4)$$

[84] studies analytically how the channel estimation error appears in the capacity formula, and derives mathematical expressions for the first- and second-order approximations of the error. [85] investigates in the measurement errors for low rank channels and derives error bounds for the capacity and eigenvalue distributions due to measurement imperfections such as finite signal-to-noise ratio and multi-path leakage.

Using the measured samples $\tilde{\mathbf{h}}$ of the channel influences the calculation of the mutual information

$$C_{\text{meas}} = \frac{1}{B} \frac{1}{K} \sum_{b=1}^B \sum_{k=1}^K \left\{ \log_2 \left[\det \left(\mathbf{I}_{n_R} + \frac{\rho}{n_T} \tilde{\mathbf{h}}(k, b) \tilde{\mathbf{h}}(k, b)^H \right) \right] \right\} \quad (3.5)$$

$$= \frac{1}{B} \frac{1}{K} \sum_{b=1}^B \sum_{k=1}^K \left\{ \log_2 \left[\det \left(\mathbf{I}_{n_R} + \frac{\rho}{n_T} (\mathbf{h}(k, b) + \mathbf{n})(\mathbf{h}(k, b) + \mathbf{n})^H \right) \right] \right\} \quad (3.6)$$

which results in an overestimation of the mutual information of the channel $C_{\text{meas}} \geq C$. In the following I will investigate the effect of the measurement noise on the mutual information using my channel model (as described in the next chapter). I add white Gaussian noise to the simulated impulse responses to simulate noisy measurements.

The results for three different parameter sets of my model are shown in Figure 3.29 for $\rho = 10$ dB. A measurement SNR of 0 dB means that the measurement noise on the channel keeps as much power as the channel impulse response itself. ρ is kept constant over all values of the measurement SNR whereas the noisy channel impulse response $\tilde{\mathbf{h}}$ is normalized to a power of one for each value of the measurement noise. Therefore the maximum capacity does not change for different values of the added noise level. For low measurement noise levels (around -30 dB) the calculated mutual information denotes the correct value for the given channel. If measurement noise increases also the mutual information increases. The increase of mutual information is upper bounded by the case when only measurement noise is left. White Gaussian

noise has the same *virtual* capacity⁵ as the i.i.d. channel and is plotted as upper bound in the Figure 3.29. The lower bound on the mutual information is given by a rank-one channel matrix.

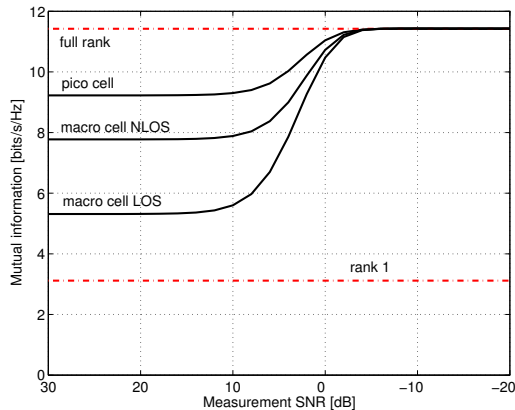


Figure 3.29: Influence of the measurement SNR on the mutual information for $\rho = 10$ dB and three types of channels: macrocell LOS, macrocell NLOS, picocell (highest capacity).

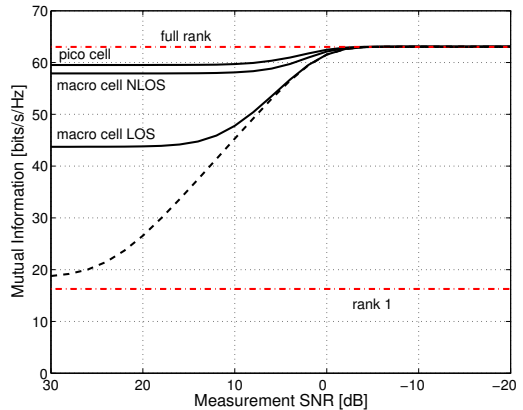


Figure 3.30: Influence of the measurement SNR on the mutual information for $\rho = 50$ dB and three types of channels: macrocell LOS, macrocell NLOS, picocell (highest capacity). In addition a pure LOS channel (one single path) is plotted for comparison (dashed line).

It is important to distinguish between the measurement noise and the ρ , which I will call *analytic SNR* in the following, used for the calculation of the mutual information. The measurement SNR is given by the measurement itself. The measurement noise directly influences the channel impulse response \mathbf{h} . In contrast the SNR for calculating the mutual information is a multiplicative factor outside of the channel impulse response. It can be seen in Figure 3.29 that the required measurement SNR depends on the rank of the channel matrix itself. For low rank channels a slightly higher measurement SNR is required. This is intuitively clear since adding white noise to a low rank channel modifies the channel matrix stronger than adding noise to a high rank channel. Figure 3.29 shows that for an analytic SNR of 10 dB the required measurement SNR has to be greater than 13 dB to ensure correct estimates of the mutual information. In addition to the results for an analytic SNR of 10 dB I have investigated the high SNR case as well. The results for an analytic SNR of

⁵I call this capacity value *virtual* capacity since one can not transmit information over noise.

50 dB are shown in Figure 3.30.

The first effect visible for the high SNR case is that the differences in mutual information for the three scenarios are getting smaller. Due to the high SNR smaller eigenvalues of the channel itself have significant contribution to the mutual information which is not seen in the low SNR case. I have therefore added a pure LOS case (dashed line in Figure 3.30) to show the low rank case as well.

Normalization of the Channel Transfer Matrix

As stated in Section 3.3.1 the channel transfer matrix obtained from measurements has to be normalized for the calculation of mutual information. There are several possibilities of normalizing the MIMO channel transfer matrix. If I am interested in the mutual information of a specific MIMO channel I will normalize over all sets of transfer functions within a specific LRS [4] I have measured.

For the evaluation of measurements it is useful to distinguish between two normalization approaches [86]: (i) constant transmit power (CTP), and (ii) constant receive power (CRP) (averaged over a LRS). In the former case, large-scale effects like shadowing and pathloss changes influence the capacity. Furthermore, several important practical systems do not have power control (e.g., IEEE 802.11). Finally, the CTP case allows a fair comparison of different MT positions from a system point of view.

The case of constant receiver SNR corresponds to systems with power control; many practical systems (like 3GPP, GSM, IS-95) use power control. Furthermore, constant receive SNR is a situation that has been investigated extensively in the theoretical MIMO literature.

Both normalization methods have their benefits and drawbacks. To illustrate the effect of the normalization on the mutual information I have plotted the mutual information and the receive power level for two specific measurement runs taken at Kvadraturen (low BS position) in Figure 3.31. The black curves denote results for the CTP normalization whereas the red curves show the CRP case. The left figures show measurement run no.17 (see Figure 3.23) starting closer to the BS and moving away. The MT antenna is pointing towards the BS position. The receive power level is nearly constant and therefore also the capacity stays within the same order of magnitude.

The properties of measurement run no.8 are different. In this case the MT starts at the street of the BS and moves into the side road. In the beginning there is an LOS between the BS and the MT and with the movement of the MT the LOS becomes diffracted at the edge of the building at the street crossing. The antenna is pointing

towards the main road. As one would expect, the receive power decreases significantly during the movement. The change in pathloss over about 70 m of movement is around 20 dB. In addition a bypassing tramway is visible in the receive power graph which results in a strong drop of the receive power after a movement of about 5 m. This shadowing of a substantial part of the energy can be watched in the capacity plot as well. The capacity plot shows two overlapping effects: first, the high power in the beginning results in high capacity values for the CTP case. Second, applying some kind of power control results in lower mutual information values in the presence of a dominant path.

This example of the two measurement runs also explains why a lot of people think LOS is bad for MIMO communications. If I normalize the channel matrix to CRP, the mutual information in the LOS case is smaller than in the NLOS case. But this normalization eliminates the huge gain of the mutual information for the LOS case due to its higher receive power level. As one can see in Figure 3.31(d), the highest mutual information for CTP is achieved in the LOS case. From a system level point of view it might be of more interest to perform a normalization of all matrices since this reflects the case of CTP.

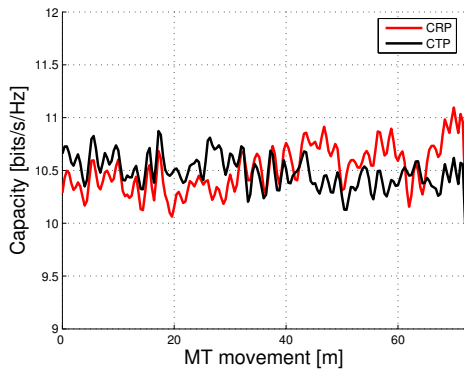
Mutual Information in Urban Areas using Dual Polarized Receive Antenna Elements

The results of this section are obtained from the measurements at Kvadraturen, Oslo. The principal idea is to compare the mutual information of different antenna element combinations of the receive antenna array at the MT side. The orientation of the MT antennas is due to the position and movement of the user and usually varies over time. I therefore want to study the performance of dual polarized antenna arrays in comparison to single polarized (vertically or horizontally) arrays. The set of 4 dual polarized receive antennas at the MT allows to chose several different combinations of 4 antennas to build a 4×4 MIMO system. Out of all possible antenna combinations I have chosen 5 antenna combinations to form the receive array. These 5 combinations are depicted in Figure 3.32. They include a purely vertically array, the horizontally polarized counterpart and three different combinations of two vertically and two horizontally polarized antenna elements. The transmit polarization at the BS is vertical.

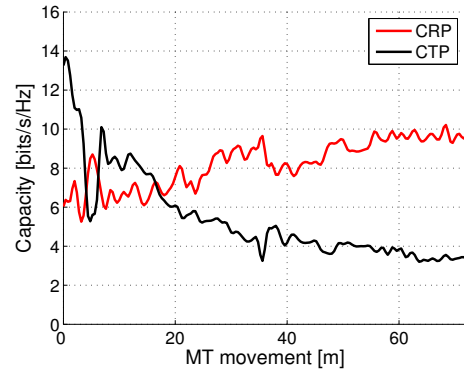
Figure 3.33 shows the mutual information of all the antenna combinations for the two measurement runs I have already used for the discussion on the normalization. For both measurement runs the purely vertically polarized antenna array performs

best. The worst result in terms of mutual information is obtained by the horizontally polarized receive array. The mismatch in polarization and the therefore resulting loss in receive power explains the loss of about 1 bit/s/Hz on average. The three dual-polarized antenna arrays result in nearly the same performance and are slightly worse than the vertically polarized array. But they are all better than the horizontally aligned array. At this point I want to stress that perfect co-polarization, as can be observed for these measurements, rarely occurs in practical systems. Scattering by a user, and tilting of the arrays by the user, lead to cross-polarization.

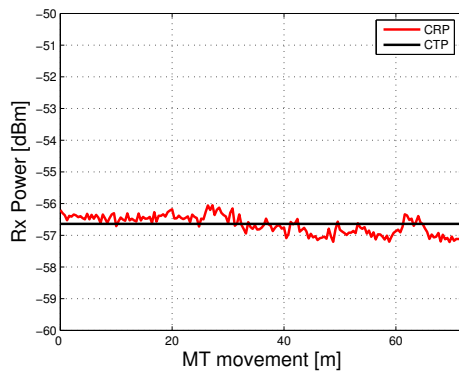
To obtain more quantitative results I plot the CDFs of all antenna combinations in Figure 3.34. If the polarization of the transmit and the receive antenna are perfectly aligned, the highest overall mutual information is obtained. All three dual polarized antenna combinations behave nearly equal and loose about 0.4 bits/s/Hz of mutual information compared to the vertically polarized antenna combination. The worst case is a complete mismatch in polarization of the transmit and receive antenna. In this case one loses additional 0.4 bits/s/Hz or about 8% of the average mutual information. In terms of outage capacity at the 5% level of the CDF the loss of mutual information of the horizontally polarized antennas compared to the vertically polarized ones is about 0.6 bits/s/Hz.



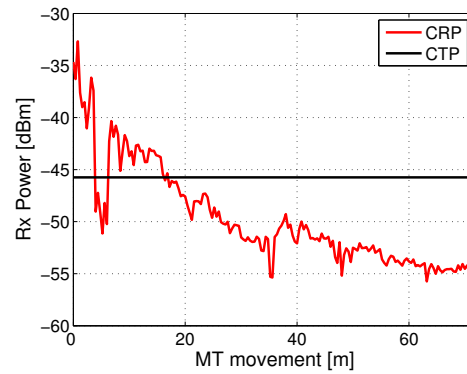
(a) Mutual information, run 17.



(b) Mutual information, run 8.



(c) Receive power, run 17.



(d) Receive power, run 8.

Figure 3.31: The mutual information and the receive power for two different power normalization strategies. Left: measurement route 17, moving away from the BS; right: measurement run 8, moving away from the BS.

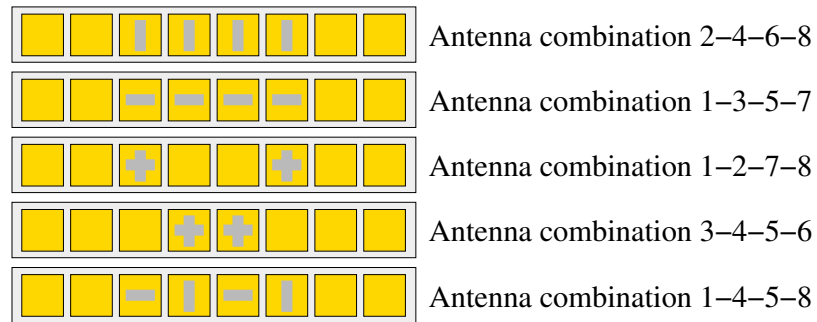


Figure 3.32: The 5 antenna combinations at the MT side. Only the inner 4 antenna elements out of 8 were used. Antenna elements 2,4,6,8 are vertically polarized and antenna elements 1,3,5,7 are horizontally polarized.

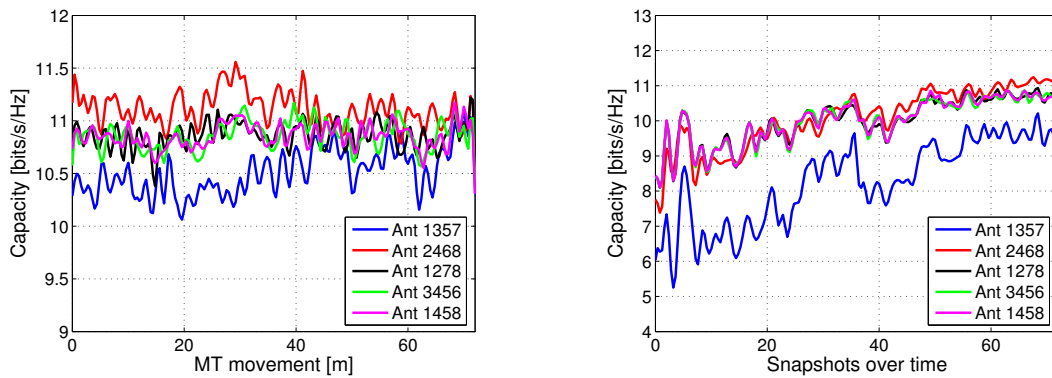


Figure 3.33: Mutual information over time for two measurement runs at Kvadraturen (low BS position).

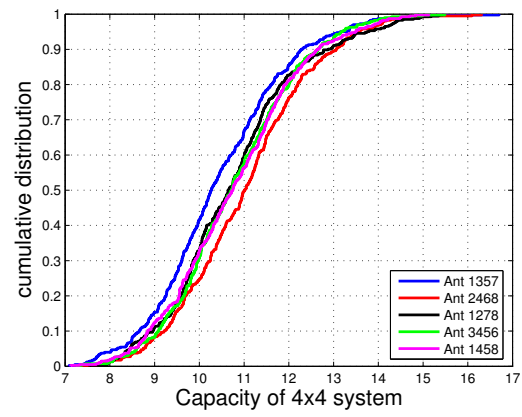


Figure 3.34: CDF of the mutual information of the five antenna combinations for all measurement runs at Kvadraturen.

3.3.2 Long Term Properties of the Channel

Many beam forming methods proposed for mobile communication systems [87] are based on the assumption, that the spatial properties of the channel change very slowly. This is strongly related to the wide sense stationarity assumption [80] which says that second order statistics can be viewed as constant over certain time intervals.

Whereas a lot of algorithms apply this assumption inherently, [88] explicitly distinguishes between short-term and long-term properties. The spatial properties are often considered as spatial covariance matrices [89].

I have chosen two dense urban area scenarios to quantify the long term effects by usage of the F-eigen-ratio [14]. In the following I briefly review the F-eigen-ratio and show results of the Kvadraturen measurements campaign (Section 3.2.2) and from the Weikendorf measurements (Section 3.2.1).

F-eigen-ratio

In [14] the *F-eigen-ratio* is introduced. It is a measure describing the discrepancy between two covariance matrices. The name emphasizes the fact, that the eigen structure of the matrices is considered [88]. Translated to the spatial long-term variations, the MIMO channel is measured at time $t_0 - \Delta t$ and a spatial covariance matrix $\mathbf{R}(t_0 - \Delta t)$ is calculated for that time. Formally, it can be written as

$$\mathbf{R}(t_0) = \sum_{k=1}^{n_T} \sum_{s=S_0}^{S_0+\Delta_S} \sum_{\tau=1}^{n_\tau} \vec{h}_k(s, \tau) \cdot \vec{h}_k(s, \tau)^H, \quad (3.7)$$

where n_T and n_τ are the number of Tx antennas and the number of delay values, and $S_0, S_0+1, \dots, S_0+\Delta_S$ are the snapshot numbers in the time interval $[t_0; t_0 + \Delta t_{avg}]$. The elements of $\vec{h}_k(s, \tau)$ are the τ th impulse response values from transmit antenna k to all receive antennas of snapshot s . This covariance matrix is then applied, for e.g. downlink beamforming [90], at time t_0 , where the spatial structure of the channel might have changed. In real systems it is not possible to use the actual covariance matrix since it takes time to estimate it out of measurement data. The changed channel is described by its covariance matrix $\mathbf{R}(t_0)$ at time t_0 . The F-eigen-ratio accounts for the resulting SNR loss due to the usage of an outdated covariance matrix. The considered covariance matrices are members of the complex space $\mathcal{C}^{n_R \times n_R}$ where n_R is the number of receive antennas. At first the eigenvalue decompositions

$$\mathbf{R}(t_0 - \Delta t) = \hat{\mathbf{W}} \cdot \hat{\mathbf{\Lambda}} \cdot \hat{\mathbf{W}}^H \quad ; \quad \mathbf{R}(t_0) = \mathbf{W} \cdot \mathbf{\Lambda} \cdot \mathbf{W}^H \quad (3.8)$$

are computed where $\hat{\mathbf{\Lambda}}, \mathbf{\Lambda} \in \mathcal{R}^{n_R \times n_R}$ are diagonals with the eigenvalues of $\mathbf{R}(t_0 - \Delta t), \mathbf{R}(t_0)$ as entries, and the columns of $\hat{\mathbf{W}}, \mathbf{W} \in \mathcal{C}^{n_R \times n_R}$ are the corresponding eigenvectors. The hat stresses the outdated nature of the eigenvectors $\hat{\mathbf{W}}$ and eigenvalues $\hat{\mathbf{\Lambda}}$, whereas \mathbf{W} and $\mathbf{\Lambda}$ are the correct values, which are assumed to be unavailable. Furthermore, the reduced versions $\hat{\mathbf{W}}_F, \mathbf{W}_F \in \mathcal{C}^{n \times F}$ of the matrices $\hat{\mathbf{W}}, \mathbf{W}$ are introduced, which contain the eigenvectors corresponding to the F largest eigenvalues of the covariance matrices $\mathbf{R}(t_0 - \Delta t)$ and $\mathbf{R}(t_0)$, respectively. Then, the F-eigen-ratio is defined as

$$q_{eigen}^{(F)}(\Delta t) = \frac{\text{tr} \left\{ \hat{\mathbf{W}}_F^H \cdot \mathbf{R}(t_0) \cdot \hat{\mathbf{W}}_F \right\}}{\text{tr} \left\{ \mathbf{W}_F^H \cdot \mathbf{R}(t_0) \cdot \mathbf{W}_F \right\}} \quad (3.9)$$

with the properties $0 \leq q_{eigen}^{(F)}(\Delta t) \leq 1$, $q_{eigen}^{(F=n_R)}(\Delta t) = 1 \forall \Delta t$ and $q_{eigen}^{(F)}(0) = 1 \forall F$.

In other words, the F-eigen-ratio expresses the loss in SNR for a beamforming system due to the application of outdated antenna weights $\hat{\mathbf{W}}_F$ instead of the correct weights \mathbf{W}_F .

The F-eigen-ratio gets higher with rising F values, since with a higher-rank approximation it is more likely to match the signal carrying dimensions. It is not a monotone function due to the side lobes of the beam patterns corresponding to the eigenvectors in $\hat{\mathbf{W}}$. With a higher angular spread, the curves flatten out. However, the F-eigen-ratio is a sensible measure in the range down to approximately -12 dB [14].

Extraction of the Covariance Matrices I extract spatial covariance matrices from the measurements as described in [14], which will be reviewed in the sequel. I use only a bandpass-filtered version of the impulse response, applying a brickwall filter with center frequency 2 GHz and bandwidth 5 MHz. A 5 MHz bandwidth is typical for 3rd generation mobile communication [91]. For all investigations in this section only one row (8 elements) of the receive antenna elements is used. The spatial covariance matrix is set up by incoherently averaging over all delay values, all transmit antennas and a time interval Δt_{avg} . A covariance matrix is initiated each Δt_{new} seconds.

Special attention is paid to the choice of the parameters Δt_{avg} . On one hand, it should be large enough that all short-term effects are eliminated by averaging. Otherwise, the rank of the matrices would decrease. On the other hand, a too large value violates the WSS assumption already within a single covariance pretending a higher rank than the true one.

The chosen values of $\Delta t_{avg} = 6$ sec result in relatively smooth F-eigen-ratio curves

over time⁶. This suggests that the averaging is long enough to achieve stable matrices. On the other hand the rank of the matrices is even smaller than expected, so that the choice of Δt_{avg} seems to be reasonable.

The parameter Δt_{new} is set to a slightly smaller value than Δt_{avg} to establish a small temporal overlapping between the matrices.

Figure 3.38 shows an example for the F-eigen ratio derived from a measurement run of the Weikendorf measurements (Section 3.2.1). In Figure 3.37 the corresponding movement of the MT is depicted. For this example I have chosen a measurement run where the transmitter moves through a pedestrian tunnel. The run covers more or less a LOS scenario with diffraction over the rooftops. However, changes of the propagation parameters occur in the tunnel. The Rx-position is marked with a red dot whereas the blue arrow gives the movement of the transmitter. Impulse responses of the measurement scenario at $t = 0$ and with the trolley in the tunnel are shown in Figure 3.35 and Figure 3.36 respectively. The attenuation in the tunnel is about 25 dB higher than in the LOS case out of the tunnel.

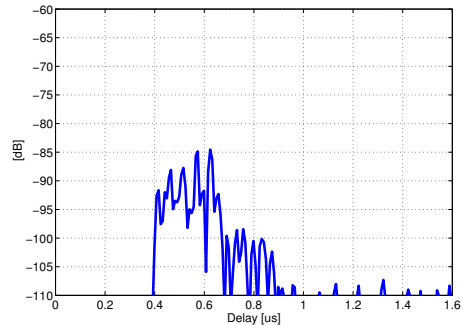
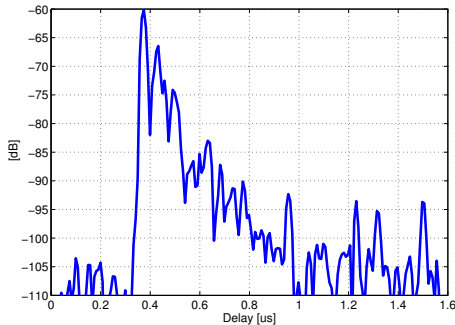


Figure 3.35: Impulse response at the start position of the MT (from [13]). Figure 3.36: Impulse response with trolley in the tunnel (from [13]).

The covariance matrixes are averaged over a window of $\Delta_s = 50$ snapshots, which is equivalent to $\Delta t_{avg} = 1 \text{ sec}$. The covered distance during that interval is in the range of about $5\lambda = 0.75 \text{ m}$. In addition to the F-eigen ratio for one and two eigenvalues also the antenna beam formed for the start position of the MT at $t = 0$ is plotted as dashed line in Figure 3.38 over the movement of the MT. For this strong LOS-case the F-eigen-ratio for one eigenvalue fits quite well with the beams at $t = 0$ till

⁶Note that the time Δt_{avg} itself depends on the speed of the movement of the MT and is therefore measurement run specific.

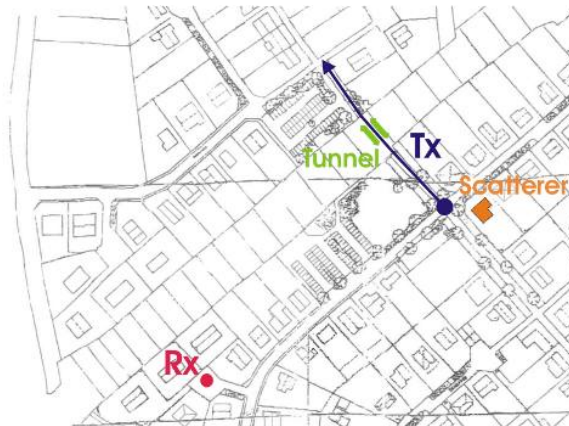


Figure 3.37: Map of the measurement route in Weikendorf.

the trolley disappears in the tunnel. This implies that during the first seconds the F-eigen ratio just describes the loss of signal energy due to the movement of the MT out of the antenna beam at $t = 0$. In the tunnel the LOS is obstructed. The strongest path appears now from nearly the same direction as at the start position of this measurement run which is used as the reference for the F-eigen ratio. This path results from a scattering process⁷ at the single family house depicted in orange in Figure 3.37. Since the strongest eigenvalue is always normalized to one, the pathloss does not influence the F-eigen ratio. This results in a strong increase of the F-eigen ratio for the time the trolley is in the tunnel.

Statistics of the F-eigen-ratio To get comparable results for different measurement campaigns I will use two additional measures introduced in [14].

In the following I consider all occurring pairs of covariance matrices $\{\mathbf{R}(t_0 - \Delta t); \mathbf{R}(t_0)\}$ for a certain value of Δt . The values of Δt are multiples of Δt_{new} for the following investigations. For each pair, the F-eigen-ratio $q_{eigen}^{(F)}(\Delta t)$ is evaluated using $F = 1$. To get comparable results to the evaluation of my channel model⁸ I have now chosen the Kvadraturen measurement campaigns 3.2.2 carried out in downtown Oslo. Each curve in the Figures 3.39 depicts the CDF of the F-eigen-ratio $q_{eigen}^{(F)}(\Delta t)$ for a

⁷Since there is no wall in the right direction to obtain a reflection towards the BS and also the receive power of that component is very low, I assume a scattering process for this propagation component, maybe including diffraction on the edge of the house.

⁸My channel model is described in Section 4 in detail and the evaluation of my model can be found in Section 5.

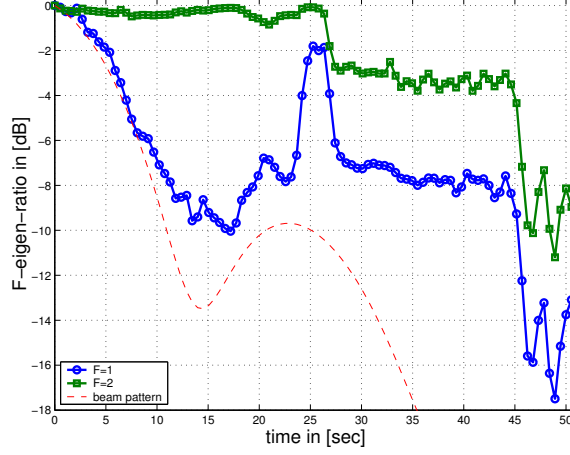


Figure 3.38: F-eigen-ratio for Weikendorf measurement over time (from [13]).

single value of Δt .

In addition to the F-eigen-ratio I define the *long-term time constant* τ_{LT} as in [92]:

Definition: *The spatial long-term time constant τ_{LT} is the time difference Δt for which the ($F = 1$)-eigen-ratio $q_{eigen}^{(F=1)}(\Delta t)$ is less than 1 dB in 90% of all cases.*

This time constant corresponds to the CDF curve crossing the point (1dB; 90%). Other definitions of the long-term time constant would change the following results quantitatively, but not qualitatively.

The long-term time constant depends on the speed of the movement of the MT. To be able to compare results obtained in different environments I use another measure, the spatial wide sense stationarity quality Q_{WSS} [92]. The Q_{WSS} compares the long-term time constant τ_{LT} with the coherence time τ_{coh} of the channel. The coherence time and the maximum Doppler frequency are inversely related. I use the most simple definition of the coherence time being the duration of one cycle of the maximum Doppler frequency

$$\tau_{coh} = \frac{c_0}{f_C v_{MT}}. \quad (3.10)$$

This is a very simple and rough estimate of the coherence time since there is an uncertainty relationship between the coherence time and the maximum Doppler

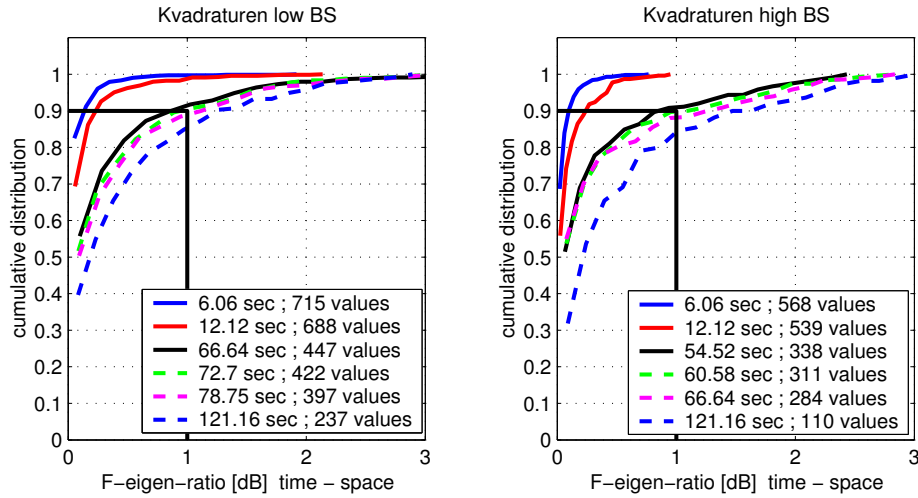


Figure 3.39: The CDF of the F-eigen-ratio for several values of Δt . Left: the high BS, right: the low BS position (from [45]).

frequency [93], [94]. However, for the usage of the coherence time within my thesis this simple definition based on the maximum Doppler bandwidth is appropriate since it is used for the comparison of different measurement results only.

The velocity of the mobile is about 1 km/h translating to a Doppler frequency of 2 Hz for a carrier frequency of 2.1 GHz and a coherence time of 500 ms.

To get a measure for the spatial WSS quality Q_{WSS} the quotient

$$Q_{WSS} = \frac{\tau_{LT}}{\tau_{coh}} \quad (3.11)$$

is defined as described in [92] which is a number expressing over how many multiples of the coherence time the spatial properties can be considered constant.

Environment	low BS	high BS	Vienna
Long-term time constant τ_{LT}	73sec	61sec	22.6sec
Coherence time τ_{coh}	500ms	500ms	180ms
WSS Quality Q_{WSS}	146	122	126

Table 3.1: Long-term time constant, coherence time and WSS Quality

Table 3.1 summarizes the results for the WSS quality and compares them to a measurement taken in Vienna [92]. The WSS quality is in the range of 100 which seems to be a typical value for outdoor environments.

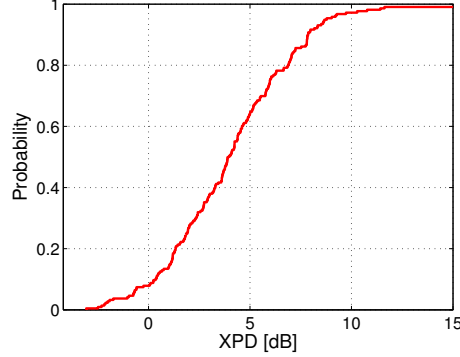


Figure 3.40: The CDF of the XPD for the Kvadraturen measurements using the low BS position.

3.3.3 Polarization

Due to the dual polarized receive antenna at the MT I was able to measure the XPD ratio

$$\text{XPD}_{VV \rightarrow VH} = \frac{P_{V \rightarrow V}}{P_{V \rightarrow H}} \quad (3.12)$$

as well. Figure 3.40 shows the CDF of the XPD for the urban Kvadraturen scenario. The XPD has a mean of $\mu_{\text{XPD}} = 3.9$ dB and a standard deviation of $\sigma_{\text{XPD}} = 3.1$ dB. These values are comparable to the suggestions of [60] and [6]. The mean value I have extracted is smaller (3.9 dB vs. 6 dB), but my value of the standard deviation is slightly larger (3.1 dB vs. 2 dB). This may result from the BS position in combination with the directional view of the BS array of my measurements which precluded the reception of a LOS component. In case of a LOS the XPD is higher than in the NLOS case due to the co-polarized LOS path. There is substantial energy in the cross polarized path component and dual polarized antennas, especially at the MT seem to be beneficial.

This result also gives an explanation for the lower values of the mutual information for the horizontally polarized receive array. The SNR for calculating the mutual information for the horizontally polarized antennas is nearly 4 dB lower than for the vertically polarized ones. The high values of mutual information for the dual polarized receive array lead to the conclusion that differently polarized antennas *see* different propagation paths which results in more visible propagation components and therefore higher mutual information. Therefore dual polarized antenna arrays are a promising

way of increasing the throughput of a channel. Especially at the MT side, where the orientation of the antenna varies due to the movement of the user, dual polarized antennas can increase the data throughput substantially [95].

I have also extracted the XPD ratio for the indoor Atrium area at Fornebu. The XPD has a mean of $\mu_{\text{XPD}} = 0.45$ dB and a standard deviation of $\sigma_{\text{XPD}} = 1$ dB. The values here deviate significantly from the COST 273 suggestions for the PCH environment which are $\mu_{\text{XPD}} = 9$ dB and a standard deviation of $\sigma_{\text{XPD}} = 2$ dB. The very small mean XPD value for the Atrium area sounds reasonable due to the irregular structure of metal and glass covered walls. On the other hand the COST 273 values might be a good choice for LOS scenarios.

Chapter 4

A new MIMO Channel Model

In the following I will describe the channel model I have developed and implemented. It is based on the GSCM approach [41]. The model was originally designed for the smart antenna case with a single transmit antenna and several receive antennas. The principle of the GSCM is shown in Figure 4.

In the original GSCM three propagation components are assumed: a line-of-sight component, a local cluster around the MT, and far clusters. The model performs simple ray tracing, each MPC interacts with one IO. The delays are given by the spatial placement of the MPCs, however the path gain of the paths is based on stochastic considerations and not on the distances between antennas and IOs¹. Multiple interactions are not considered to limit computational complexity.

Since MIMO became more and more important I have extended the model to the MIMO case using approaches found in literature for the following extensions

- polarization diversity, as introduced in COST 259,
- double scattering [42], [44], and
- multi-user scenarios [6] with several MTs and BSs.

Furthermore I have introduced the twin cluster concept [58], [96] to allow for independent DOA and DOD modelling without the complexity of conventional double-scattering models. The next section will describe the structure of the model, followed by a discussion about the features of the model I have implemented.

For ease of notation the time-dependence of all the parameters is not explicitly written in the following.

¹A description of all these parameters will be given in the following sections of this chapter.

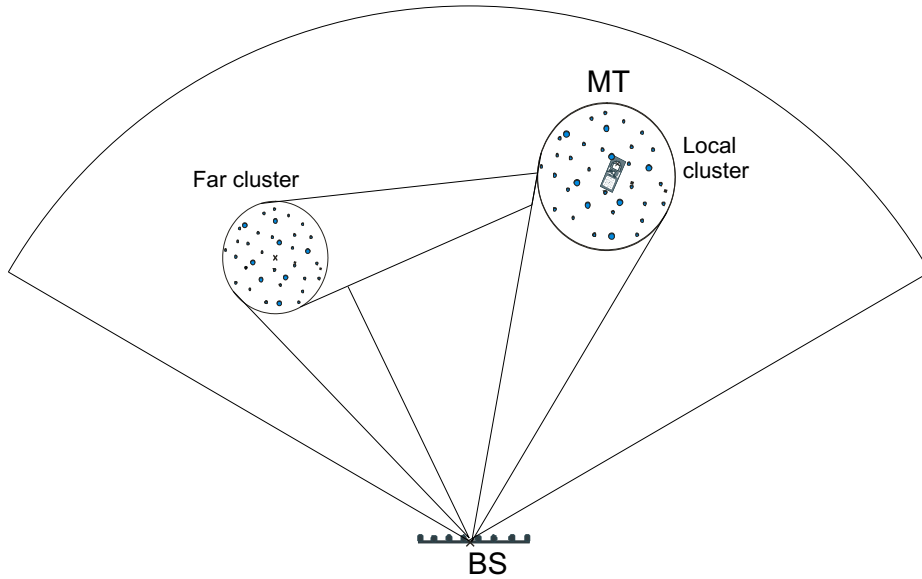


Figure 4.1: Principle of the GSCM. One local cluster around the MT and additional far clusters in the cell.

4.1 Interfaces and Modules

One goal of the concept of my model is to keep it flexible. A modular structure takes care of the strict separability of the different channel model components and allows for later interchange of separate parts. Similar approaches can be found in [97],[98]. My model consists of three modules:

- the Propagation Module,
- the Antenna Module, and
- the Convolution Module.

The model structure is shown in Figure 4.2. All relevant interfaces and signals are labelled with lower case letters and summarized in Table 4.1. A closer description on the interfaces is given in the sequel. In [98] the Mascaraa channel model proposes another structure which divides the model into a configuration, a pre-processing, and a simulation part. Each part consists of several submodules. The first difference to my approach is that I do not use a separate configuration module. In my structure the specifications are part of the depending modules and the Antenna Module is a discrete part of the whole model whereas in the Mascaraa approach the antennas are part of

Symbol	Description
b	PA-Interface
c	AC-Interface
h	unfiltered channel impulse response
h_F	channel impulse response
u	filtered input signal
v	unfiltered output signal
x	unfiltered input signal
y	filtered output signal

Table 4.1: The interfaces and signals of my model.

the pre-processing module. I prefer to have the antennas separated from all other computations. Changing the model, e.g. implementing a new standardized model, may affect the pre-processing part of the model. Keeping the Antenna Module as a separate module with clearly defined interfaces eases the reuse of the already existing code.

The biggest difference between the two approaches from a computational point of view is the way the convolution of the input signal with the channel is performed. Mascaara uses a convolution of the impulse response with the input data in frequency domain whereas I perform a convolution of the MPC parameters, which can be seen as the impulse responses of the single MPCs, in time domain. Both approaches have computational advantages, my approach is specifically designed for the usage of FPGAs in real time systems.

The Propagation Module covers all the computations and specifications that are often called a channel model by itself. It has a specified interface to the Antenna Module which I call the Propagation-Antenna(PA)-Interface. This interface presents the information on all MPCs and also handles global simulation parameters like the center frequency or the sampling rate. A closer description is given in Section 4.1.1. The Propagation Module updates all the information periodically to allow for continuous simulation. I have chosen a two step update procedure since the fluctuation of the various parameters differs. In the *small-scale update* (SS-update) process the fast changing parameters like the MT position are recomputed whereas the *large-scale update* (LS-update) modifies parameters like the pathloss. A more detailed description of the update process is given in Section 4.10.

The Antenna Module takes the antenna geometries and the antenna patterns at both

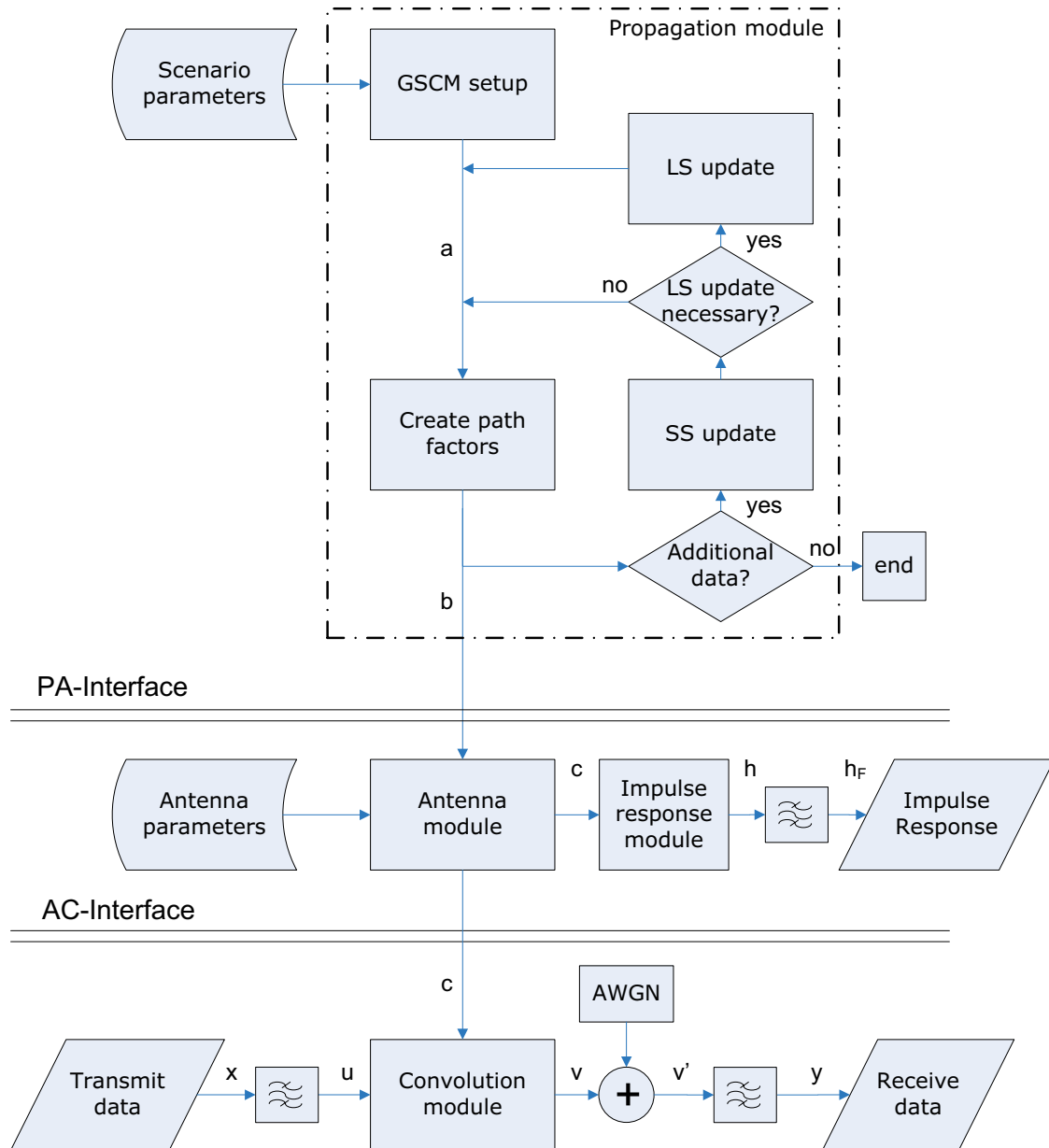


Figure 4.2: Model structure.

link-ends into account. In this part the geometrical information is reduced to the MPC gain factor and a delay value for each MPC. The interface to the Convolution Module is called Antenna-Convolution(AC)-Interface. The Convolution Module computes the output signal for each receive antenna by summing up all contributions resulting from a convolution of the transmit signals and the corresponding MPC impulse responses.

To keep the simulation time within manageable limits the values of the MPCs are computed after defined time intervals but not on symbol level. It has to be ensured that during this interval the movement of the mobile is not more than half a wavelength.

A description of the modules and interfaces will be given in the following subsections.

4.1.1 PA-Interface

I have chosen a set of nine parameters that describes the propagation properties of a single MPC including polarization. The nine parameters are given in Table 4.2. The interaction of the MPCs with the IOs is traced in the same sequence as it would

Parameter	Description
$A_{VV,s}$	Path gain of the vertical co-polarized part of the s^{th} MPC
$A_{VH,s}$	Path gain of the cross-polarized part of the s^{th} MPC (from V to H)
$A_{HH,s}$	Path gain of the horizontal co-polarized part of the s^{th} MPC
$A_{HV,s}$	Path gain of the cross-polarized part of the s^{th} MPC (from H to V)
τ_s	Path delay of path s
$\phi_{DOD,s}$	Direction of Departure in Azimuth of path s
$\theta_{DOD,s}$	Direction of Departure in Elevation of path s
$\phi_{DOA,s}$	Direction of Arrival in Azimuth of path s
$\theta_{DOA,s}$	Direction of Arrival in Elevation of path s

Table 4.2: Parameters of the PA-Interface.

occur in an actual (physical) propagation environment: from the Tx antenna towards the first IO and from the last IO towards the Rx antenna. There is no difference between single-bounce and multiple-bounce paths at the PA-Interface and the following modules.

For the whole simulation I define a global coordinate system reflecting the simulation scenario in analogy to the real world. To include polarization I have decided to define horizontal and vertical polarization using this global coordinate system and not to rely on any polarization orientation of the antennas. These global coordinate system is also used for the PA-Interface. The orientation of the antennas and their influence on the polarization is taken into account in the Antenna Module. If an antenna is rotated in space compared to the global coordinate system (x, y, z) , all propagation components are divided into the global vertical and the global horizontal parts as illustrated in Figure 4.3. The transmitted vertically polarized component $V1$ is transformed to the reference system components V and H . The IO may cause depolarization and at the receive antenna V and H are transformed to $V2$ and $H2$ which denote vertical and horizontally polarized components for the receive antenna. The antenna coordinate systems $(x1, y1, z1; x2, y2, z2)$ are local coordinate systems around the antenna and their orientation depends on the (time-varying) orientations of the antennas. A pure vertically oriented propagation path at the Tx antenna is immediately transformed into a global vertical and a global horizontal path component. At the IO additional depolarization effects may occur and the impinging components at the receive antenna are locally transformed into the corresponding components.

At the PA-Interface all the parameters of all MPCs are grouped together resulting in a 2-dimensional matrix for each MT-BS combination where the parameters of each MPC denote one row. The whole matrix for several BSs and MTs has 4 dimensions where the third dimension is spanned over the corresponding BSs and the fourth dimension over the MTs. In addition the rotation of the MT and BS antennas $(\phi_{DOD,a}, \phi_{DOA,a}, \theta_{DOD,a}, \text{ and } \theta_{DOA,a})$, where a denotes the antenna index, and the number of samples between the updates are part of the PA-Interface. The impulse response can now be written as

$$\mathbf{h}(\tau, \theta_{DOA}, \theta_{DOD}, \phi_{DOA}, \phi_{DOD}) = \sum_{s=1}^S \Xi_s \delta(\tau - \tau_s) \delta(\theta - \theta_{DOD,s}) \delta(\theta - \theta_{DOA,s}) \delta(\phi - \phi_{DOD,s}) \delta(\phi - \phi_{DOA,s}), \quad (4.1)$$

where S denotes the number of paths, \mathbf{h} keeps the impulse responses of all four main polarization combinations

$$\mathbf{h} = \begin{bmatrix} h_{VV} & h_{VH} \\ h_{HV} & h_{HH} \end{bmatrix}, \quad (4.2)$$

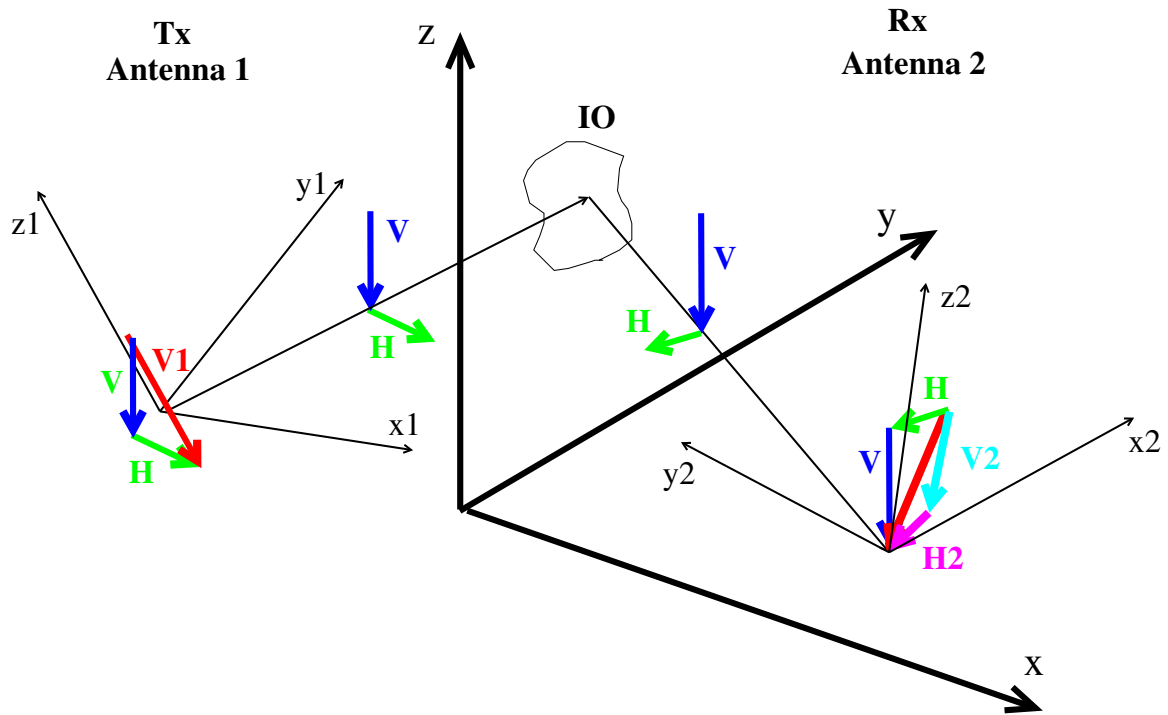


Figure 4.3: The GSCM coordinate systems. x, y, z denote the reference coordinate system where x_1, y_1, z_1 and x_2, y_2, z_2 are the antenna coordinate systems.

and Ξ is the polarization matrix of the path gain coefficients:

$$\Xi_s = \begin{bmatrix} A_{VV,s} & A_{VH,s} \\ A_{HV,s} & A_{HH,s} \end{bmatrix}. \quad (4.3)$$

The elements of Ξ are typically complex valued allowing for independent phase shifts of polarization components of each path. Note that all the parameters are time-dependent. To keep the formula readable the time-index is omitted for all the parameters.

The detailed properties of the antennas remain unspecified at this point. The directivity and orientation of the antennas will have strong influence on the radio channel. In the simplest case of vertically polarized antennas at both link ends, with perfect cross polarization discrimination, h_{VV} is the only relevant quantity and all the other parameters can be neglected since none of the antennas can 'see' the corresponding

contributions. The influence of the antennas will be discussed in Section 4.1.6 in more detail.

Summed up, the PA-Interface describes the propagation scenario.

4.1.2 AC-Interface

The interface between the Antenna Module and the Convolution Module is defined in the same way as the PA-Interface. Each MPC is reduced in the AC-Interface to its MPC gain coefficient and its MPC delay for every single antenna port

$$h(\tau) = \sum_{s=1}^S A_s \delta(\tau - \tau_s), \quad (4.4)$$

where I suppress the port index in order to simplify notation. The polarization matrix Ξ_s of each MPC is reduced to the MPC gain factor A_s and includes the influence of the antenna pattern. A more detailed description on the computation of A_s can be found in Section 4.1.6.

4.1.3 Convolution Module

This module uses the MPC gain and delay coefficients of the AC-Interface and calculates the delayed and attenuated convolution of the input signal and the channel impulse response:

$$y = h(\tau) * x, \quad (4.5)$$

where $*$ denotes the convolution. To keep computational effort within limits, the AC-Interface updates the channel only after a specified time interval and not for each sampling value of the input signal. To ensure a one-to-one mapping of the movement to the phase an update after a movement of the MT of $\lambda/2$ has to be performed².

Most fluctuation of the single MPCs is due to the movement of the MT in space. Each MPC denotes a HPW in space which is described by a complex vector rotating over 2π per wavelength in space. If the MT moves by $\lambda/2$ in the direction of the MPC, the magnitude of this vector can be assumed as constant, but the phase of the vector describing the MPC changes by π . Linear interpolation of this vector using supporting points spaced at $\lambda/2$ results in an interpolation trajectory which

²For linear movements, larger update intervals in the range of several wavelengths are possible. The one-to-one mapping of the movement to the phase does no longer exist but there is a linear relationship between the two measures. I have not included this feature to my model since I want to keep the Convolution Module as simple as possible.

goes through the origin of the coordinate system. Such an interpolation contradicts reality since the principle of the conservation of energy is violated. The energy of the MPC is proportional to the squared magnitude of the complex propagation vector. Therefore the magnitude of the interpolated signal has to be (nearly³) constant. An interpolation using magnitude and phase of the signal reflects the physical basis of the MPC in a much better way and is therefore chosen.

Discrete Delay Samples and Oversampling

To compute the convolution of the channel with the transmit signal the delay values of the computed MPCs have to be quantized at a given rate. There are two possibilities for this quantization:

- sinc-interpolation of each MPC at the Nyquist rate,
- linear interpolation of each MPC at a higher sampling rate.

The sinc-interpolation method has the advantage of the lower (Nyquist) sample rate but the drawback that the sinc-function has several nonzero sampling points which have to be taken into account. Only a finite number of them can be used in real systems resulting in a calculation error.

The linear interpolation requires a higher sampling rate but quantizes each MPC to only one sampling point. An error occurs here as well and the difference between the two approaches is minor.

I have chosen the linear interpolation approach which seems better suited to real time processing in FPGAs due to the simpler structure (of course at higher sampling rate). The sample rate has to be high enough to reflect nature with minor deviations. On the other side it should be as low as possible to limit the computational effort. It is important to note that the sample rate of the channel model has to be higher than the sample rate of the receiver. I will now discuss this topic in more detail.

If I assume a very simple channel with just one MPC corresponding to one Dirac pulse as the channel impulse response, the sampling effect can be illustrated. Since each channel, and also each system, is band-limited the Dirac impulse is broadened by the receive filter. For the following investigations I assume a rectangular receive filter with a bandwidth equal to the system bandwidth. If the Dirac position is synchronized to the sampling rate, the filtered signal is a sinc-function with zero

³Of course the energy of the wave changes over the distance of the point of interest to the transmit antenna but this change is on a much larger scale than $\lambda/2$.

value at all sampling positions except the position of the Dirac. This is shown in Figure 4.4.

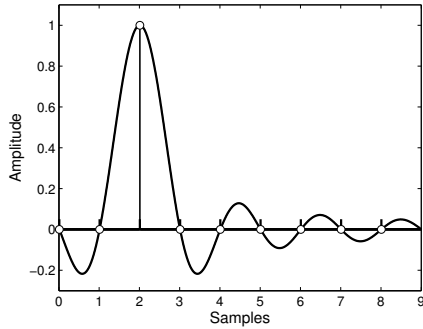


Figure 4.4: Dirac at sampling position.

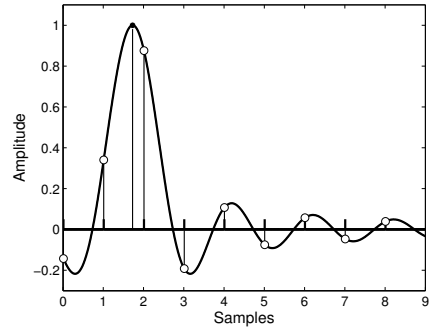


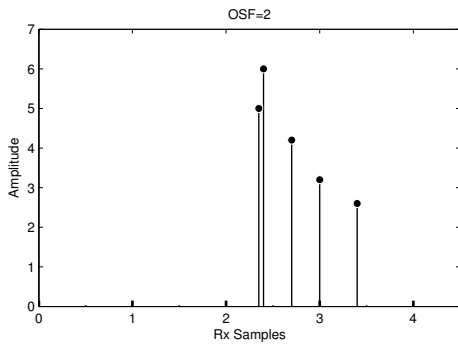
Figure 4.5: Dirac at arbitrary position.

If the MPC does not arrive exactly at a sampling position, the energy of the MPC is spread over infinitely many sampling points (see Figure 4.5). Note that the sampling points in this section denote the sampling points of the receiver. The sampling rate of the channel has to be higher to take this effect into account⁴.

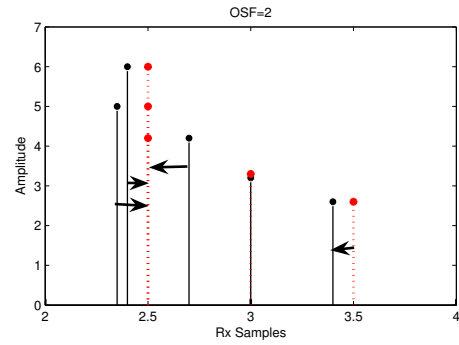
To overcome the effect, the channel has to be computed at a higher sampling rate than the receiver. The effect of the oversampling factor on the channel impulse response is shown in Figure 4.6. In the first plot an arbitrary set of MPCs is shown (Figure 4.6(a)). The delays of the MPCs are defined by their path lengths. As a first step the channel model quantizes the delays of the MPCs to the sample rate of the channel model (Figure 4.6(b)). For an oversampling factor of 2 the quantization allows all full and half-width values on the sampling scale of the receiver. Figure 4.6(c) includes the sinc-functions of the MPCs due to the filter function of the receiver for all sampling points. Due to the small oversampling factor the sinc-functions look more like triangles. Summed up the receive signal of all MPCs is shown in Figure 4.6(d). Due to the receive filter each receive sample covers signal contributions of all MPCs.

Figure 4.7 illustrates the effect of the oversampling for the same impulse response of 6 paths as in Figure 4.6 and an oversampling factor of 1, 2, 4 and 100. Comparing Figure 4.6(d) and Figure 4.7(d) reveals that a high oversampling factor renders the receive signal best. High oversampling factors decrease the performance of a channel model and therefore a measure for the minimum required oversampling factor is

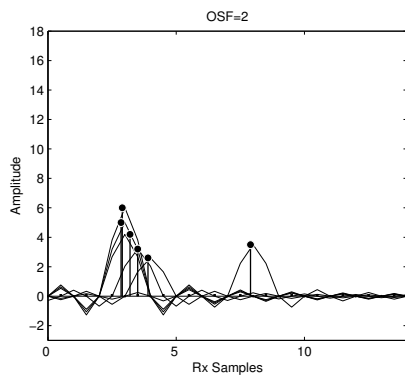
⁴A sample-spaced channel model eases the design of the receive algorithm significantly since the whole energy of a MPC is included in one delay bin only. However such an assumption is unrealistic and has to be avoided.



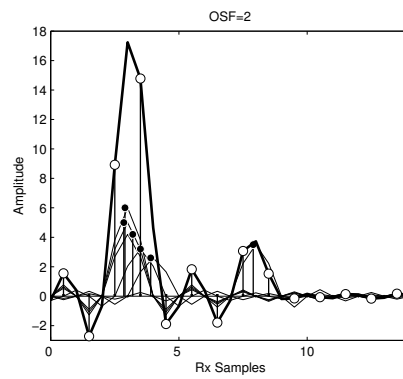
(a) MPC components at arbitrary positions.



(b) Quantization of the MPC delays to the sample values.



(c) The sinc-functions of the MPCs due to the receive filter.



(d) The whole receive signal (large open circles).

Figure 4.6: The quantization of the MPC delays.

needed.

To get such a quantitative measure I make the following assumptions: the channel consists of a set of S paths with an amplitude $A \in [0, 1]$ and a delay $\tau \in [0, 5]$. I define the oversampling factor as the quotient of the sample rate of the channel model to the sample rate of the receiver:

$$\text{OSF} = \frac{t_{S,\text{channelmodel}}}{t_{S,\text{receiver}}}. \quad (4.6)$$

The channel impulse response can now be calculated by

$$h(k) = \sum_{s=1}^S A_s \delta(k - k_s), \quad (4.7)$$

where k denotes the sample points of the discrete signal. In a next step I reduce the sampling rate to the rate of the receiver

$$h(k_{\text{OSF}}) = h(k \cdot \text{OSF}). \quad (4.8)$$

and use a quadratic distance measure to quantize the results:

$$d^2(\text{OSF}) = \mathbf{E} \left\{ \sum_{k=1}^K \frac{h(k_{\text{OSF}})^2 - h(k_{\infty})^2}{h(k_{\infty})^2} \right\}. \quad (4.9)$$

For the computations I have chosen an oversampling factor of 100 as a reference realization. In Figure 4.8 the resulting error for several oversampling factors of interest is shown. Already a two times over-sampled channel model is a great advantage compared to a model running at the symbol rate of the receiver. The error curve flattens out very rapidly and, taking complexity issues into account, I have chosen an oversampling factor of 4 for my model.

The Convolution

The traditional way of computing the receive signal is to compute the channel impulse response and perform a convolution with the input signal [99]. For a geometry-based channel model this approach has several drawbacks. For every update of the impulse response all the MPC parameters have to be recalculated. In my case this is performed in the SS-update process. An exact computation of all the MPCs for every

⁵The sample rate of the receiver is not necessarily the symbol rate of the system.

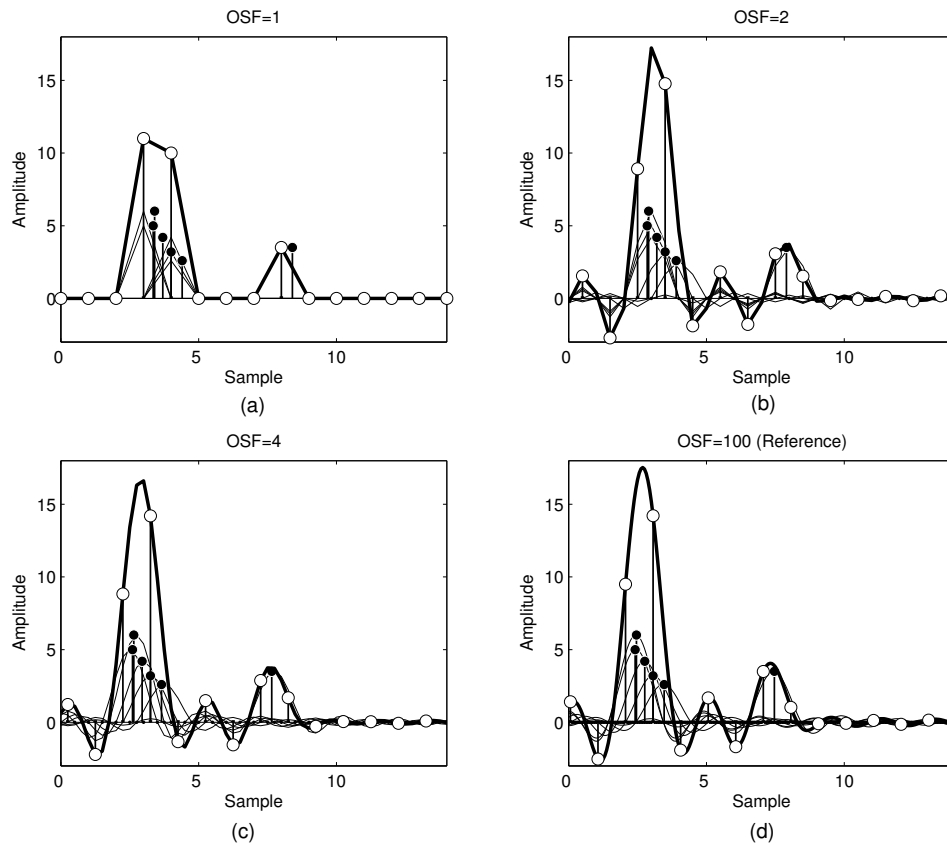


Figure 4.7: Effect of the oversampling factor of the channel model on the impulse response at the receiver. Large open circles denote the sample values of the receiver and small black dots denote the original paths. The amplitude is drawn in linear scale.

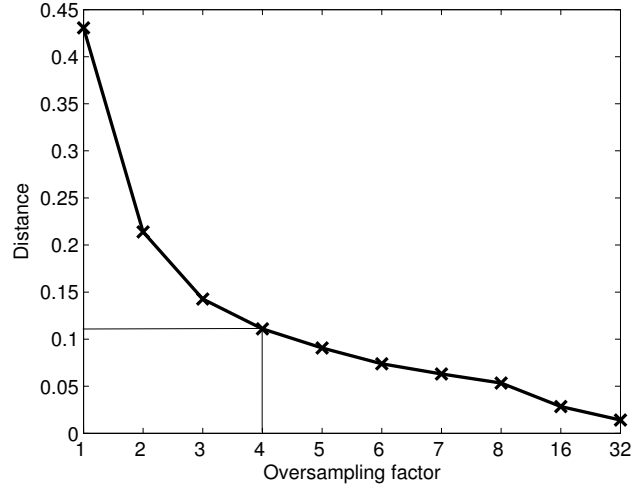


Figure 4.8: Error, induced by finite OSF of model and linear interpolation, in the modelled receive signal.

transmit symbol would increase simulation times tremendously and is not necessary⁶. To reduce the number of updates I have decided to perform the convolution of the filtered input signal $u(t)$ with the channel based on the MPC parameters A_s and τ_s themselves

$$v(t) = \sum_{s=1}^S A_s(t) \delta(\tau_s) u(t - \tau_s). \quad (4.10)$$

The interpolation is performed in amplitude and phase as discussed in Section 4.1.3 in more detail.

One additional implementation aspect is to disregard weak MPCs that are below a certain threshold. Weak MPCs occur in the case of weak IO weights or in the case of directional antennas. This step helps keeping computational cost within manageable limits.

⁶Due to the multi-path fading the impulse response itself changes very quickly and several parameter updates within half a wavelength are required.

Synchronization

As the GSCM is based on ray-tracing, physically the resulting delay of the channel impulse response corresponds to the lengths of the propagation paths. The impulse response starts at a delay equal to the LOS delay and not with zero delay. Therefore a synchronization algorithm is mandatory for any receive algorithm test which is the main purpose of my model. But engineers would like to study their receive algorithms independently from any synchronization issues. A newly developed receive algorithm does not necessarily include synchronization capabilities at an early stage. For this reason I have included a possibility to modify the MPC delays to emulate various synchronization states of the receiver. I have identified three synchronization modes of interest including multi-user scenarios:

1. no synchronization,
2. synchronization of the first MT to the first BS, and
3. perfect synchronization of all MTs to all BSs.

The three synchronization modes are illustrated in Figure 4.9. The first synchronization mode performs no synchronization and all the signals keep their delays as calculated by geometric considerations.

The second mode subtracts the delay of the (quasi-)LOS component of the first MT to the first BS from all propagation paths. Therefore only the signal of the first transmitter is synchronized to the receiver, all other signals keep their relative time offset.

The third synchronization mode now assumes that all transmit signals arrive at the receivers at the same time. The delay of the (quasi-)LOS component is subtracted from all corresponding paths. This mode reflects a perfect synchronization between all transmitters and receivers⁷ and allows testing of multi-user receive algorithms without any synchronization capability.

⁷Note that such perfect synchronization between multiple transmitters and multiple receivers is not possible in real life since different delays are subtracted from the same signal for different receivers. However, this mode helps testing simple algorithms where a frame based processing of receive data is performed. As soon as the frames of several transmit signals are not synchronized a multi-user receiver has to store data in between adjacent frames to be able to decode the pilot sequences and estimate the channel.

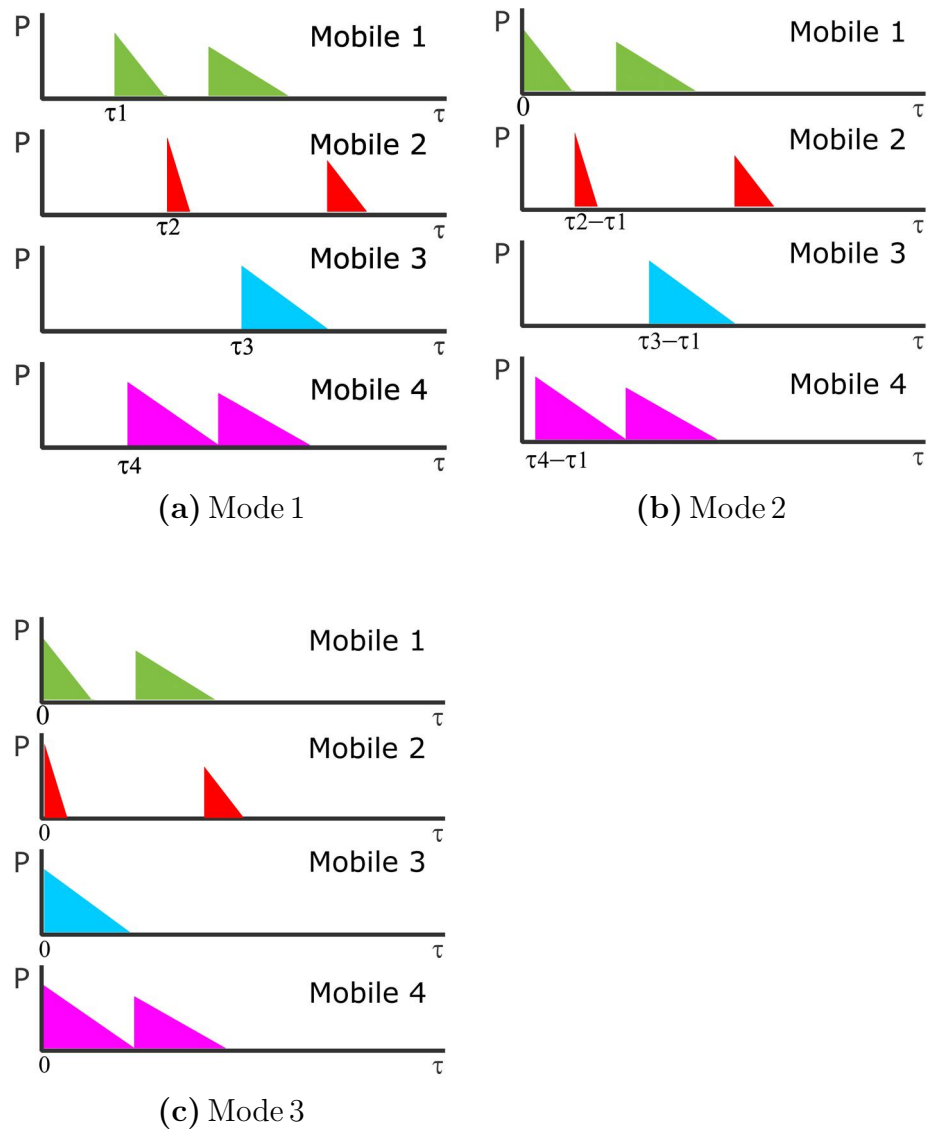


Figure 4.9: The three synchronization modes of the GSCM.

4.1.4 Receive and Transmit Filter

All the input parameters and specifications of the GSCM are obtained from measurements. The typically used measurement equipment [8], [9] supports bandwidths of up to about 100 MHz, which specifies the reasonable bandwidth of the channel model as well. For wide-band and ultra-wide-band channels other channel models may perform better. I have designed the GSCM mainly for UMTS applications. The receive and transmit filters of UMTS are root-raised-cosine filters with roll-off factor $\alpha = 0.2$:

$$H_{\text{Tx}}(f) = H_{\text{Rx}}(f) = \begin{cases} 1 & 0 \leq f \leq \frac{1-\alpha}{T_s} \\ \sqrt{\frac{1}{2}(1 + \cos(\frac{T_s\pi}{\alpha}(f - \frac{1-\alpha}{2T_s})))} & \frac{1-\alpha}{T_s} \leq f \leq \frac{1+\alpha}{T_s} \\ 0 & \frac{1-\alpha}{T_s} \leq f \leq \infty \end{cases} . \quad (4.11)$$

4.1.5 Impulse Response Module

The impulse response of the channel can be computed in addition to the convolution of the transmit signal with the MPCs. The stand-alone impulse response is not necessary for the channel model itself but provides additional information for the user of the model. The computed impulse response allows to test the performance of algorithms under the constraint of perfect channel knowledge. On the other hand investigations on the performance of a channel estimator without a receiver can be performed.

Each time a new set of parameters is computed by the Propagation Module the MPC information is used to generate the impulse response of the channel

$$h(\tau) = \sum_{s=1}^S A_s \delta(\tau_s - \tau), \quad (4.12)$$

whereas h denotes the unfiltered impulse response. Usually the filtered impulse response is required and therefore the transmit and receive filter has to be applied on h :

$$h_F(\tau) = h_{\text{Tx}(\tau)} * h(\tau) * h_{\text{Rx}}(\tau). \quad (4.13)$$

4.1.6 Antenna Module

The Antenna Module has two inputs. One is the PA-Interface (see Section 4.1.1) and the other input is the specification of the antenna parameters. If antennas other than omni-directional antennas are taken into account, the information on the antenna

pattern and orientation has to be applied to the MPC information. Since the MPC information covers information on azimuth and elevation, spherical antenna patterns are required. One definition for such two-dimensional antenna patterns (joint azimuth and elevation) is provided by the *GAI Antenna Measurement File Format* from Aalborg University [100]. This file format was originally designed to exchange information on spherical antenna measurements. The data of the file is organized in a matrix of floating point numbers, where the matrix has six columns and a number of rows, depending on the number of sampling points. Each row represents the antenna gain in a specific direction, as specified in Table 4.4. In principle, the definition of directions can be chosen arbitrarily but has to be consistent through out the whole channel model. I have decided to define zero degree in azimuth and elevation as the broadside direction of the antenna array (Figure 4.10). The antennas might be placed arbitrary in space. If an antenna is rotated in space the coordinate system of the antenna and the global coordinate system, which is used for the definition of the angles of the MPCs, are not aligned. This misalignment is described by the antenna angles in azimuth $\phi_{\text{DOD},a}, \phi_{\text{DOA},a}$ and elevation $\theta_{\text{DOD},a}, \theta_{\text{DOA},a}$ in the global coordinate system for the transmit and receive side respectively. For the calculation of the antenna gain for each MPC the MPCs have to be rotated to the coordinate system of the antenna

$$\phi'_{\text{DOD},s} = \phi_{\text{DOD},s} - \phi_{\text{DOD},a}, \quad (4.14a)$$

$$\phi'_{\text{DOA},s} = \phi_{\text{DOA},s} - \phi_{\text{DOA},a}, \quad (4.14b)$$

$$\theta'_{\text{DOD},s} = \theta_{\text{DOD},s} - \theta_{\text{DOD},a}, \quad (4.14c)$$

$$\theta'_{\text{DOA},s} = \theta_{\text{DOA},s} - \theta_{\text{DOA},a}, \quad (4.14d)$$

where the prime denotes the relative angles as seen in the antenna coordinate system.

Additional information on the antenna and the measurement is provided in the end of the GAI measurement files (see Table 4.3).

Using this file format for the antenna pattern does allow for a variety of different antennas. Synthetic antenna patterns can be used as well as measured antenna patterns.

The antenna pattern $\Omega_{\text{Tx},\text{Rx}}$ are now applied to the MPC information provided by the PA-Interface. Including the antenna pattern into (4.1) yields

$$\mathbf{h}(\tau, \theta_{\text{DOA}}, \theta_{\text{DOD}}, \phi_{\text{DOA}}, \phi_{\text{DOD}}) = \sum_{s=1}^S \Omega_{\text{Tx},s} \Xi_s \Omega_{\text{Rx},s} \delta(\tau - \tau_s), \quad (4.15)$$

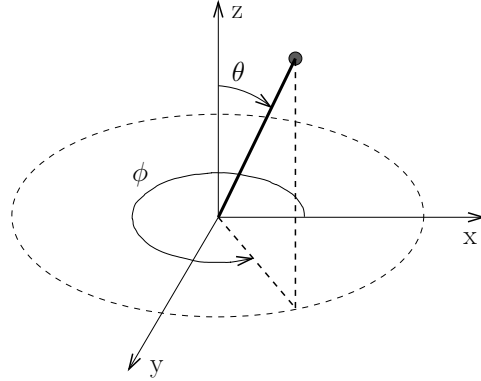


Figure 4.10: The antenna directions for the GAI measurement file format.

Parameter	Description
Dir:	Link direction of measurement; uplink: Dir= 1, downlink: Dir= 2, unspecified direction: Dir= 0.
MeasID:	A number identifying the measurement, for example the measurement time in the form 'yyymmddhhmm'.
Frequency:	Measurement frequency in Hz.
N:	The number of samples in the θ -angle.
M:	The number of samples in the ϕ -angle.
Δ_θ	The angle increment in the θ -domain.
Δ_ϕ	The angle increment in the ϕ -domain.

Table 4.3: Additional information of the GAI measurement file format.

where the information on the directions is now included in the antenna pattern at the transmitter and receiver

$$\mathbf{\Omega}_{Tx,s} = \begin{bmatrix} \Omega_{Tx,s}^V(\theta_{DOD,s}, \phi_{DOD,s}) & 0 \\ 0 & \Omega_{Tx}^H(\theta_{DOD,s}, \phi_{DOD,s}) \end{bmatrix}, \text{ and} \quad (4.16)$$

$$\mathbf{\Omega}_{Rx,s} = \begin{bmatrix} \Omega_{Rx}^V(\theta_{DOA,s}, \phi_{DOA,s}) & 0 \\ 0 & \Omega_{Rx}^H(\theta_{DOA,s}, \phi_{DOA,s}) \end{bmatrix} \quad (4.17)$$

respectively. Summing up the four elements of $\mathbf{\Omega}_{Tx,s} \mathbf{\Xi}_s \mathbf{\Omega}_{Rx,s}$ gives the MPC gain

coefficients A_s of the single MPC

$$\begin{aligned}
A_s = & \Omega_{\text{Tx},s}^V(\theta_{\text{DOD},s}, \phi_{\text{DOD},s}) A_{\text{VV},s} \Omega_{\text{Rx},s}^V(\theta_{\text{DOA},s}, \phi_{\text{DOA},s}) + \\
& \Omega_{\text{Tx},s}^V(\theta_{\text{DOD},s}, \phi_{\text{DOD},s}) A_{\text{VH},s} \Omega_{\text{Rx},s}^H(\theta_{\text{DOA},s}, \phi_{\text{DOA},s}) + \\
& \Omega_{\text{Tx},s}^H(\theta_{\text{DOD},s}, \phi_{\text{DOD},s}) A_{\text{HV},s} \Omega_{\text{Rx},s}^V(\theta_{\text{DOA},s}, \phi_{\text{DOA},s}) + \\
& \Omega_{\text{Tx},s}^H(\theta_{\text{DOD},s}, \phi_{\text{DOD},s}) A_{\text{HH},s} \Omega_{\text{Rx},s}^H(\theta_{\text{DOA},s}, \phi_{\text{DOA},s}). \tag{4.18}
\end{aligned}$$

These are now the MPC gain coefficients of the whole system including the antennas. The impulse response is calculated by

$$h(\tau) = \sum_{s=1}^S A_s \delta(\tau_s - \tau). \tag{4.19}$$

θ_0	ϕ_0	$\text{Re}[E_\theta(\theta_0, \phi_0)]$	$\text{Im}[E_\theta(\theta_0, \phi_0)]$	$\text{Re}[E_\phi(\theta_0, \phi_0)]$	$\text{Im}[E_\phi(\theta_0, \phi_0)]$
θ_0	ϕ_1	$\text{Re}[E_\theta(\theta_0, \phi_1)]$	$\text{Im}[E_\theta(\theta_0, \phi_1)]$	$\text{Re}[E_\phi(\theta_0, \phi_1)]$	$\text{Im}[E_\phi(\theta_0, \phi_1)]$
\vdots	\vdots	\vdots	\vdots	\vdots	\vdots
θ_0	ϕ_{M-1}	$\text{Re}[E_\theta(\theta_0, \phi_{M-1})]$	$\text{Im}[E_\theta(\theta_0, \phi_{M-1})]$	$\text{Re}[E_\phi(\theta_0, \phi_{M-1})]$	$\text{Im}[E_\phi(\theta_0, \phi_{M-1})]$
θ_1	ϕ_0	$\text{Re}[E_\theta(\theta_1, \phi_0)]$	$\text{Im}[E_\theta(\theta_1, \phi_0)]$	$\text{Re}[E_\phi(\theta_1, \phi_0)]$	$\text{Im}[E_\phi(\theta_1, \phi_0)]$
\vdots	\vdots	\vdots	\vdots	\vdots	\vdots
θ_{N-1}	ϕ_{M-1}	$\text{Re}[E_\theta(\theta_{N-1}, \phi_{M-1})]$	$\text{Im}[E_\theta(\theta_{N-1}, \phi_{M-1})]$	$\text{Re}[E_\phi(\theta_{N-1}, \phi_{M-1})]$	$\text{Im}[E_\phi(\theta_{N-1}, \phi_{M-1})]$
Dir	0	MeasID	0	Frequency	0
N	M	Δ_θ	Δ_ϕ	0	0

Table 4.4: The GAI Antenna Measurement File Format.

4.1.7 Propagation Module

This module is the heart of my channel model. It reads the specifications of the environment and the physical parameters as its input.

It was originally designed to fit the COST 259 [6] recommendations for macro- and micro-cells. In addition to the COST 259 channel model I have implemented the COST 273 MIMO channel model. Later on I have broadened my model to include an AWGN channel and a simple Rayleigh fading model. Every receive algorithm is programmed slightly different and uses different interface definitions for the input signal, the impulse responses and so on. Often very simple channel models like an AWGN channel are used during the implementation phase of the algorithm. Such

simple models have the benefit of very short simulation times but inherently neglect realistic behaviors like signal correlations or path dispersion⁸. Having simple models with the same interfaces as the GSCM eases the linkage of the channel model and the receive algorithm. In a first step the receive algorithm is tested with a simple model. As soon as the simple model shows the expected behavior, additional features of the GSCM are added and the performance of the algorithm can be tested again. If the performance gets worse the receive algorithm is not capable of coping with this specific effect and should be adapted accordingly. The GSCM covers many effects related to the real channel which are neglected in simple channel models. Testing a receive algorithm with such a realistic channel model increases the capability of a receive algorithm to work in real life.

The output of the Propagation Module is defined by the PA-Interface (Section 4.1.1). The MPC parameters delay τ_s and transmit and receive angles $\theta_{\text{DOD},s}$, $\theta_{\text{DOA},s}$, $\phi_{\text{DOD},s}$, $\phi_{\text{DOA},s}$ of each MPC are computed from geometric considerations. In contrast, the MPC gain factors Ξ_s of each MPC are computed based on stochastic rules. The MPC gain factors cover all the attenuation effects including the shadow fading, the open air pathloss, and the attenuation due to the interaction at the IOs. These physical effects are the basis for the computation of the polarization dependent matrix entries $A_{\text{VV},s}$, $A_{\text{VH},s}$, $A_{\text{HV},s}$, $A_{\text{HH},s}$, of Ξ_s . I have chosen an approach where small-scale effects are separated from large-scale effects and the individual parameters represent the structure of the model based on clusters and MPCs:

$$\mathcal{A}_{\text{VV},s} = A_{\text{SF},cl} A_{cl} A_{\text{MPC},s} A_{\text{MPC},\text{corr}}, \quad (4.20)$$

where $A_{\text{SF},cl}$ denotes the shadow fading coefficient of cluster cl which is constant for one cluster but varies in between clusters. It is discussed in more detail in Section 4.8. A_{cl} is the average path gain coefficient of the whole cluster which allows for easy inter-cluster power adjustment (Section 4.4). The path gain of the single MPCs $A_{\text{MPC},s}$ influences the intra-cluster delay spread and angular spreads and is discussed in detail in Section 4.5. In addition a correction factor $A_{\text{MPC},\text{corr}}$ is used to adjust the overall receive signal to realistic values (Section 4.11). The vertical-to-vertical polarization is the basis for the whole model. How to cope with the other polarization combinations is discussed in Section 4.7.

In the next sections I will discuss the functionality of the Propagation Module in detail.

⁸Due to the band limitation of the channel each path spreads its energy over several receive samples according to the filter function of the receiver.

4.2 Cluster Distribution

As in COST 273 [60], the GSCM includes three types of clusters:

- Local clusters,
- Single-interaction clusters, and
- Twin clusters.

4.2.1 Local Clusters

Local clusters are positioned around the MT or the BS, which is shown in Figure 4.11. The cluster area is circular and the IOs are depicted as small dots of various size, indicating different weight factors. A closer description of the weighting of the IOs can be found in Section 4.5. The size of the cluster is determined by its angular spreads in azimuth and elevation and its delay spread and is discussed in Section 4.5 as well. A local cluster around the base station only occurs for pico-cells and some types of micro-cells. For macro-cellular environments the BS antenna is typically exposed on a mast and there is no physical reason for IOs close to the BS. In contrast, a local cluster around the MT exists for any environment, since I assume that the user is surrounded by several objects interacting with the wave propagation. In the COST 259 macro-cellular model, for example, the local cluster around the MT is the major propagation component. By definition, the local cluster around the MT has a large angular spread at the MT since there are IOs all around the MT. I have chosen to define the cluster around the MT to be obligatory. However, it seems possible that a propagation environment can be described by twin clusters only since twin clusters reflect the results from measurements and a local cluster can be described as a set of twin clusters, each having a small angular spread, grouped around the MT. Latest results [101], [23] have shown that all MPCs can be grouped into clusters with small angular spreads.

4.2.2 Single-interaction Cluster

The local cluster around the MT is the main propagation component for many different environments. However, measurements have shown that propagation components with larger delays occur as well [5]. Such large delays cannot be modelled with local clusters unless the local cluster becomes very large (several 100 m or even some kilometers) which contradicts the concept of a local cluster.

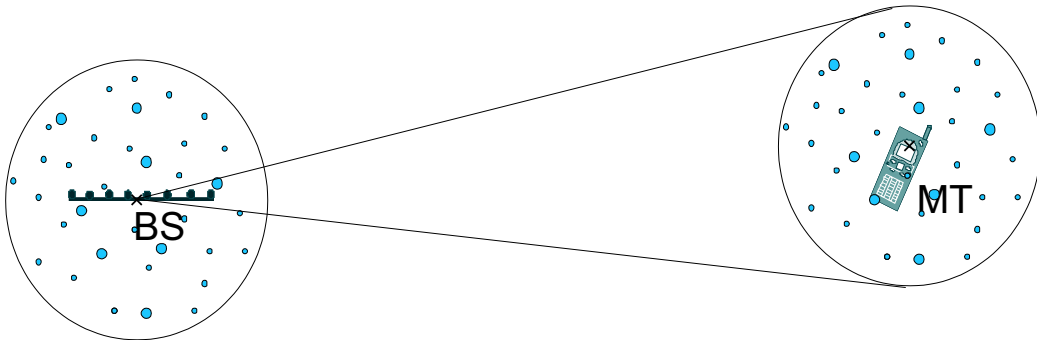


Figure 4.11: Local clusters around the MT and the BS. The different size of the IOs will be discussed in Section 4.5

To extend the concept of the local cluster and to allow for larger delay spreads, single-interaction clusters can be used. In literature they are often called *far-clusters* (e.g. [6]) but I prefer to call them single-interaction clusters to set a clear border to the twin cluster concept. The concept of the single-interaction cluster is shown in Figure 4.12. Each ray that propagates from the transmitter, bounces once at an IO of the single-interaction cluster and is received at the receiver. Each ray interacts with exactly one IO, multiple bounces are neglected to keep computational complexity within limits.

Two approaches for the placement of single-interaction clusters can be found in literature. The first and simplest approach is to distribute them uniformly over the whole simulation area [6],[102]. In [66] an alternative distribution algorithm is discussed and briefly summarized in the following. Their analysis of measurements has shown that the occurrence of clusters, as seen from the BS, depends on the LOS direction. The position of the cluster relative to the position of the BS and the cluster center, is determined by the following geometric approach: draw a line from the BS to the MT. The cluster position will be determined relative to that connection line. The radial distance from the BS is determined from an exponential distribution

$$f(r) = \begin{cases} 0 & r < r_{\min} \\ (1/(\sigma_r)) \exp(-((r - r_{\min})/(\sigma_r))) & \text{otherwise} \end{cases} \quad (4.21)$$

The angle of the cluster center is then drawn at random from a Gaussian distribution with a standard deviation σ_ϑ . This fixes the position of the cluster for one certain

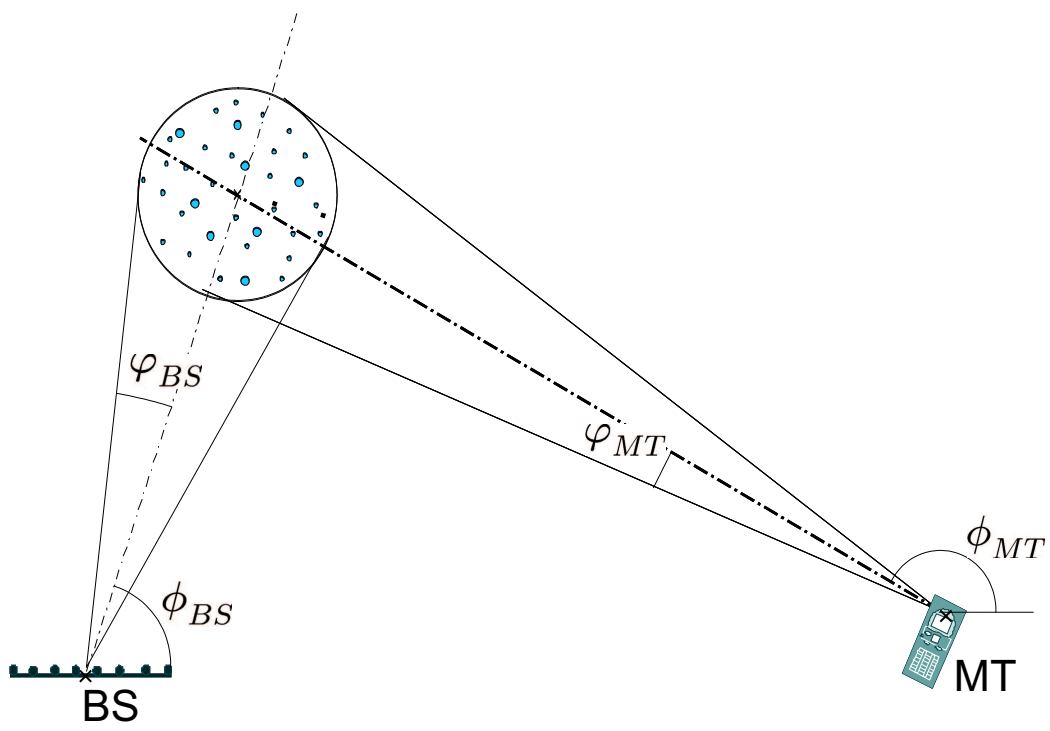


Figure 4.12: Single-interaction cluster.

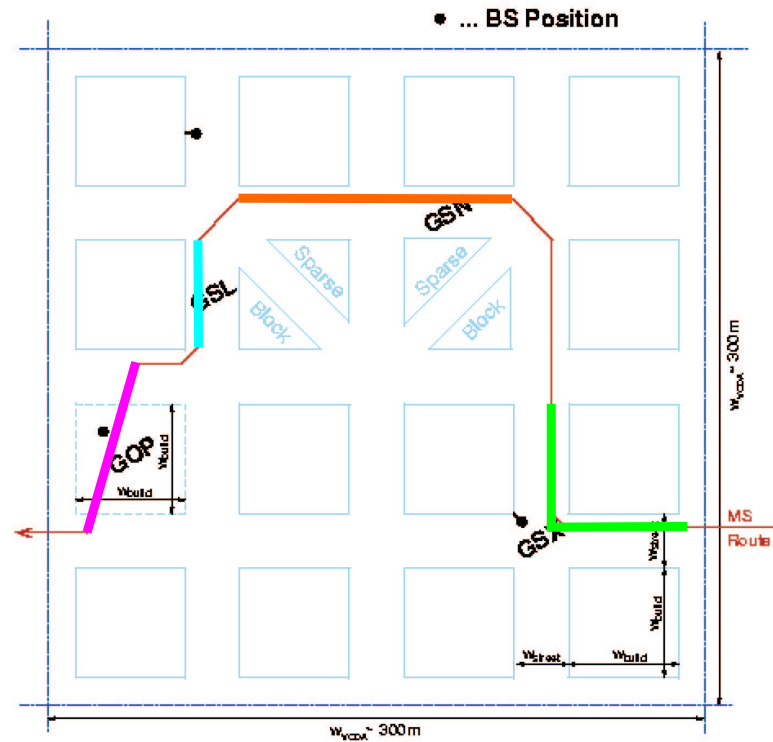


Figure 4.13: Virtual cell deployment area of the COST 259 microcells (from [6]) and the corresponding MT routes.

MT position. In Section 4.3 the cluster placement is extended for large MT movements within the whole simulation environment. As for the local cluster, the size is determined by the angular and delay spreads of the cluster.

COST 259 Microcells: In contrast to all other models I have investigated, the COST 259 microcell approach is based on a virtual cell deployment area⁹ which is shown in Figure 4.13. The MT follows a predefined route on this map and enters several scenarios. In my opinion a simulation covering different scenarios is not useful. It would just mix different properties of them and one can not quantify the result. For the simulations I have defined additional MT movements that cover only one specific scenario each. For the GOP, GSX, and GSL scenario there is a single MT track whereas there are three different BSs possible for the GNL scenario. The definition

⁹I am referring to the COST 259 final report [6]. In [103] this approach was changed.

of the tracks is color coded in Figure 4.13.

The distribution of single-interaction clusters¹⁰ is based on this virtual map and demands for clusters in all the streets which can be seen by the MT. Additional clusters may occur randomly in any direction. I have chosen to keep the cluster shape circular as all my other clusters, in which the cluster itself is not limited to the width of the street but also covers areas of houses on the virtual map¹¹. An example of the cluster distribution for the GNL scenario is given in Figure 4.14. Every street in the vicinity of the BS keeps one cluster and all clusters with a LOS connection to the MT are visible. Two additional clusters are placed at an arbitrary position in azimuth. They cover additional MPCs of, e.g., high rise buildings. The concept of visibility regions in space is used for the arbitrary microcell clusters (see Section 4.3). I personally dislike the concept of virtual cell deployment maps. For different environments different maps are required resulting in additional implementation effort without significant benefits. As the COST 259 model has shown, many people have implemented the macrocell approach but the microcell and picocell approaches were mostly neglected.

4.2.3 The Twin Cluster Concept

The drawback of single-interaction clusters is their rigid relationship between delay, angle of departure and angle of arrival. It is possible only to choose two of the three parameters and the third follows inherently. For a smart antenna system choosing the delay and the angle of arrival at the antenna array is sufficient. In MIMO systems, however, this approach is insufficient. Geometry-based channel models are an abstract representation of measured scenarios and the obtained parameters. Measured parameters are quantized to PDFs and these PDFs are taken to generate single realizations for the model. Even, if in real life the propagation is dominated via single bounce MPCs, it cannot be assured that the mapping of clusters based on individual statistics of delay, DOA, and DOD gives meaningful results. Joint statistics of these three parameters would be necessary to model an environment dominated by single-bounce MPCs via single-interaction objects only. Such joint statistics are currently not available. In [55] a first description of joint angular–delay statistics for the MPCs is given. Such joint statistics allow a more realistic modelling of single-interaction

¹⁰In COST259 only single-interaction clusters are specified.

¹¹One can assume that single-bounced waves from IOs placed inside houses on the virtual map reflect multiple-bounced wave guided MPCs through the street canyon with the last interaction occurs at the corresponding angle of the single-bounced MPC.

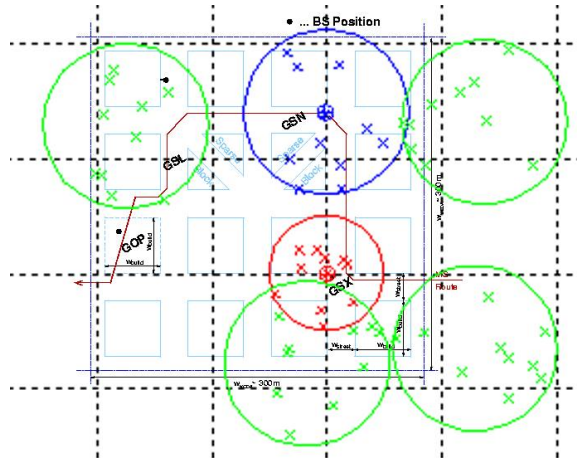


Figure 4.14: The cluster distribution of the COST 259 micro-cellular GSX scenario. The local MT cluster is depicted in blue, the local BS cluster is shown in red and the single-interaction clusters are in green. Each cluster covers 10 MPCs.

processes via single-interaction clusters. Multiple bounced MPCs demand different solutions anyway.

To avoid the limitations of single-interaction clusters researchers have started to include double-bounce MPCs in their models [43], [42]. Each MPC interacts with an IO related to the transmitter and an IO related to the receiver. The increase in complexity of such a model is tremendous. For a set of S_N objects at the transmitter and S_M objects at the receiver the total number of MPCs S , which have to be evaluated, is the product of both values:

$$S = S_N S_M. \quad (4.22)$$

To overcome the limitations of the double-bounce approach I have introduced the twin cluster concept in [58], [96]. A cluster is split up into two representations of itself: one that represents the cluster as seen by the BS and one as it is seen by the MT (Figure 4.15). The two representations are linked via a stochastic cluster link delay $\tau_{C,\text{link}}$ which is the same for all IOs inside a cluster. The cluster link delay ensures realistic MPC delays as, for example, derived from measurement campaigns, whereas the placement of the clusters is driven by the angular statistics of the cluster as observed from BS/MT respectively. The angular dispersion at the BS and MT can

therefore be modelled independently¹². The cluster is placed twice on the map and both realizations look identical, like twins. Each ray propagated at the transmitter is bounced at each IO in the corresponding cluster and reradiated at the same IO of the twin cluster towards the receiver. In between the two representations of the cluster only the cluster link delay is added.

The shape of the cluster is an ellipsoid, where the main axis are positioned according to the position of the cluster in relation to the BS/MT (see Figure 4.15). One axis points away from the BS/MT, one stays normal to this axis in azimuth and the third axis covers inherently the elevation. The lengths of the main axes are defined by the delay spread (the axis pointing away from the BS/MT) and the angular spreads in azimuth and elevation.

Due to different angular spreads at MT and BS the cluster at the MT might be a scaled version of the BS cluster twin. Such a scaling affects the positions of the IOs inside the cluster as well. Furthermore each IO at the BS side cluster has exactly one counterpart at the MT side. Therefore the total number of MPCs is equal to the number of IOs. The distribution of IOs within a cluster will be discussed in Section 4.4.

In the following the concept of how to model a cluster based on the above assumptions is developed. The large-scale behavior is an essential part of the model. All components of the model are placed on a map covering the simulation environment. This simplifies modelling the movement of the MTs and clusters compared to an approach in the delay-azimuth plane.

In a first step the start positions of the BS and MT are assigned (Figure 4.15). The spreads $\varphi_{\text{BS/MT}}$ and directions $\phi_{\text{BS/MT}}$ of a cluster in azimuth are assigned at random from the corresponding distribution functions

$$\phi_{\text{BS}} = f(\Phi_{\text{BS}}), \quad (4.23\text{a})$$

$$\phi_{\text{MT}} = f(\Phi_{\text{MT}}), \quad (4.23\text{b})$$

$$\varphi_{\text{BS}} = f(\Phi_{\text{BS}}), \quad (4.23\text{c})$$

$$\varphi_{\text{MT}} = f(\Phi_{\text{MT}}). \quad (4.23\text{d})$$

The distance of the cluster from the BS and MT are obtained from the corresponding distribution functions $d_{\text{BS}} = f(D_{\text{BS}})$ and $d_{\text{MT}} = f(D_{\text{MT}})$ (Figure 4.15). If this distribution functions are not available I use the following geometric approach. The goal is to get a circular cluster shape in the azimuth-delay plane. The size of the cluster

¹²Note that this approach is different from any multi-bounce model [44] since the twin-cluster is only one cluster having a defined shape and placement of IOs inside.

in delay direction $d_\tau = \frac{1}{2}\tau c_0$ (following the line away from the BS/MT) and the size in azimuth direction $d_C^{\text{BS}} = d_{\text{BS}} \tan(\varphi_{\text{BS}})$ and $d_C^{\text{MT}} = d_{\text{MT}} \tan(\varphi_{\text{MT}})$ are by definition the same: $d_C^{\text{BS}} = d_C^{\text{MT}} = d_C = d_\tau$, and the index for the BS and MT for the size of the cluster is therefore omitted in the following. The position of the cluster in space is computed by

$$d_{\text{BS}} = \frac{d_\tau}{2 \tan(\varphi_{\text{BS}})}, \quad (4.24a)$$

$$d_{\text{MT}} = \frac{d_\tau}{2 \tan(\varphi_{\text{MT}})}. \quad (4.24b)$$

Note that the parametrization is not based on any physical argument. The size of the cluster in elevation is now straight-forward using the angular spreads in elevation

$$\vartheta_{\text{BS}} = f(\Theta_{\text{BS}}), \quad (4.25a)$$

$$\vartheta_{\text{MT}} = f(\Theta_{\text{MT}}), \quad (4.25b)$$

of the cluster. Geometrical considerations lead to

$$h_C^{\text{BS}} = d_{\text{BS}} \tan \vartheta_{\text{BS}}, \quad (4.26a)$$

$$h_C^{\text{MT}} = d_{\text{MT}} \tan \vartheta_{\text{MT}}. \quad (4.26b)$$

The angular directions of the cluster in elevation

$$\theta_{\text{BS}} = f(\Theta_{\text{BS}}), \quad (4.27a)$$

$$\theta_{\text{MT}} = f(\Theta_{\text{MT}}), \quad (4.27b)$$

are now obtained from their corresponding distribution functions as the last step to fix the cluster in space.

When talking about spreads and the resulting dimensions of clusters, I always mean the σ -RMS spread. A cluster should cover an area of about 3σ for simulations. Figure 4.15 shows the cluster definition for the 2-dimensional case. It is obvious that the position of a cluster as seen from the BS is not the same as it is seen from the MT. An additional cluster-link delay $\tau_{\text{C,link}}$ is introduced, which ensures that the total delay of the cluster corresponds to the definitions of the scenario

$$\tau_{\text{C}} = \tau_{\text{C,BS}} + \tau_{\text{C,link}} + \tau_{\text{C,MT}}. \quad (4.28)$$

It may happen that the cluster link delay $\tau_{\text{C,link}}$ of a cluster becomes negative. A negative link delay occurs if the delay of the propagation path from the BS to the IO

plus from the IO to the MT together is larger than the total MPC delay. Note that the distance of the cluster from BS/MT and the cluster delay are chosen from independent distribution functions. As long as there are no joint distribution functions of the inter cluster delay spread and the angular spreads defined this effect may happen but has no influence on the validity of the model. In [55] joint angular and delay statistics are proposed. This new approach avoids negative cluster link delays. In principle, a negative cluster link delay has no influence on the validity of my model. It is a computational artefact which in fact ensures that the total delay of the cluster is correct. However, a negative cluster link delay is somehow non physical and describes a situation where the cluster is too far away from the BS and/or the MT. It can be avoided via replacing the corresponding cluster.

For a better illustration of the idea of the twin clusters Figure 4.16 shows a simulation scenario covering 4 twin clusters. Each cluster has the shape of an ellipsoid. The IOs are depicted as small spheres. Due to different angular spreads at the MT and the BS the corresponding twins of one cluster look different. This is the same as in real life: if you look at a twin from another perspective it may look different. But the distribution of IOs inside the cluster remains the same, it is just distorted. The clusters are numbered from 1 to 4 and the cluster #1 at the BS side corresponds to its twin #1 at the MT side.

At first sight this separation of clusters to the BS and the MT excites a Kronecker structure. Note that this is not the common Kronecker model that assumes the angular statistics to be independent at BS and MT. There can be significant coupling between DOAs and DODs due to the overlapping of clusters. Two or more clusters may have overlapping DODs but different DOAs. In the given example in Figure 4.16 the clusters #1 and #3 overlap at the MT side but do not overlap at the BS twin resulting in the uplink case in the same DOD directions but different DOAs which contradicts the Kronecker assumption.

4.3 Cluster Visibility

In contrast to the local clusters all other clusters are visible in certain regions only. In literature two different approaches can be found: the placement of visibility regions [6] and a more stochastic approach using a birth-death process [104].

I have chosen the approach using visibility regions since it fits naturally into the geometric description of the simulation environment. The visibility regions are placed uniformly within the simulation area. Each visibility region corresponds to exactly

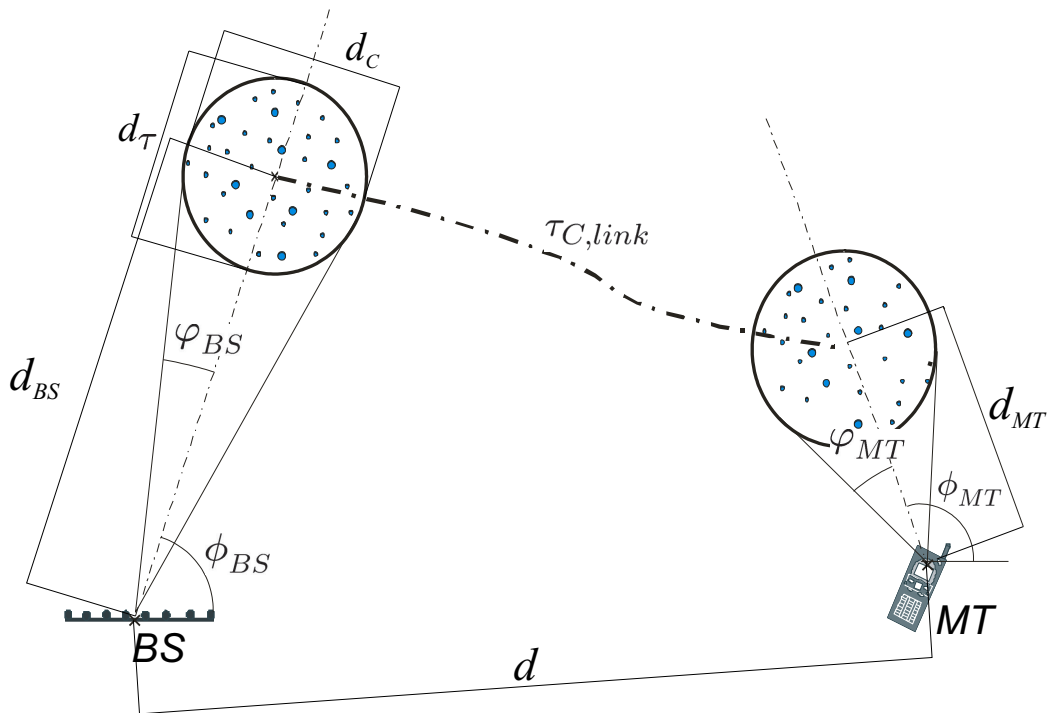


Figure 4.15: Placement of the twin cluster in the xy -plane. d denotes the distance between BS and MT, d_τ and d_c represent the lengths of the axis of the cluster, φ_{BS} and φ_{MT} are the cluster spread in azimuth, and ϕ_{BS} and ϕ_{MT} denote the angle of the cluster in azimuth. $\tau_{C,link}$ is the cluster link delay. This figure shows the case of unknown distribution functions for the distance of the cluster from the BS/MT and therefore the lengths of d_τ and d_c are per definition identical and the projection of the ellipsoid on the azimuth plane becomes a circle.

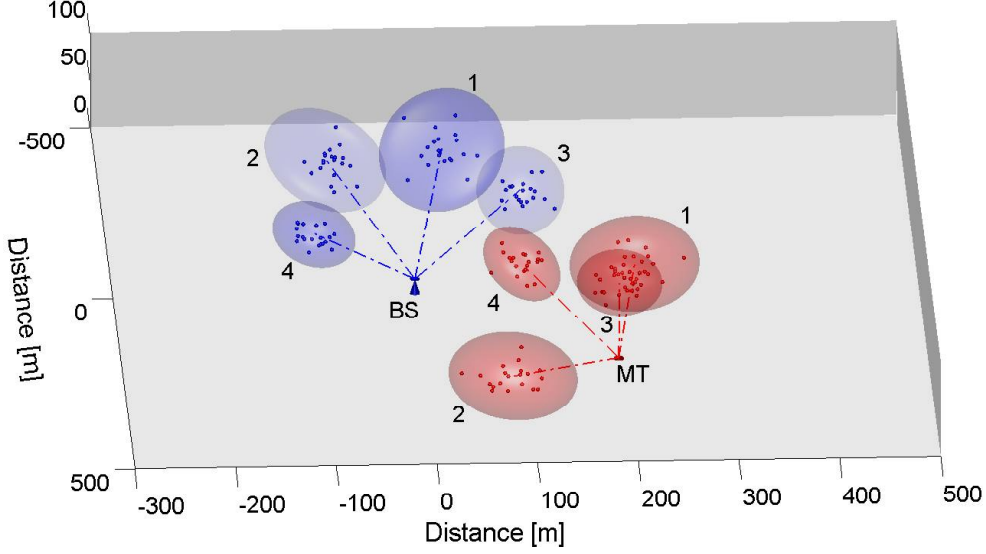


Figure 4.16: Example for the distribution of 4 twin clusters.

one cluster and determines the position of the cluster. This may result in a huge set of clusters but only few of them are visible at a time and have to be considered for the computations.

If the MT is inside a visibility region, the corresponding cluster is active and contributes to the impulse response; if the MT is outside the visibility region, the cluster does not contribute. The visibility region is characterized by

R_C : diameter of the visibility region [m].

L_C : length of the transition region [m].

The size of a visibility region depends on the simulation environment and is in the range of a few meters for pico-cells and up to several hundred meters in rural areas. A smooth transition from non-active to active clusters is achieved by scaling the MPC gain of the cluster by a factor A_m^2 [6]. The transition function used is

$$A_m(\bar{r}_{MT}) = \frac{1}{2} - \frac{1}{\pi} \arctan\left(\frac{2\sqrt{2}y}{\sqrt{\lambda L_C}}\right) \quad (4.29)$$

with

$$y = L_C + |\bar{r}_{MT} - \bar{r}_m| - R_C. \quad (4.30)$$

where \bar{r}_m is the center of the circular visibility area and λ is the wavelength.

Furthermore, the visibility region is characterized by the probability density function of its location, which depends on the distance between the visibility region and

the BS. In order to give a constant expectation for the number of clusters that equals n_C , the area density of the visibility regions needs to be [66]

$$\rho_C = \frac{n_C - 1}{\pi (R_C - L_C)^2} \quad [m^{-2}]. \quad (4.31)$$

The position of the cluster belonging to one visibility region is discussed below. The positions of the clusters should be fixed only once the MT enters a visibility region. Note that the resulting cluster is fixed in space and stays fixed as long as it is visible.

4.3.1 Single-interaction Cluster

Section 4.2.2 describes the placement of clusters in accordance with the MT position and Section 4.3 the cluster visibility. Since the MT is moving through the visibility region but the cluster is fixed in space, the MT position is not taken into account for the cluster placement. Instead the center of the visibility region is used for the cluster placement. This approach allows to place all the clusters before the start of the simulation, which is a benefit for real-time channel simulators since the real-time computational effort is reduced.

4.3.2 Twin Cluster

In accordance to the single-interaction clusters each twin cluster has one visibility region. Again, the center of the visibility region is taken for the cluster placement.

4.4 Cluster Power Model

The power contained in each cluster is a function of the delay (with respect to the LOS or quasi-LOS component). The longer the delay, the smaller is the power that it carries. However, the cluster attenuation is limited. If the attenuation becomes too high, the cluster does not have an impact on the impulse response, and is thus dropped from the considerations. Therefore the maximum attenuation of a (simulated) cluster is bounded. The power of the m -th cluster depends exponentially on the cluster delay and is

$$P_m = P_0 \max \{ \exp [-a_\tau(\tau_m - \tau_0)], \exp [-a_\tau(\tau_B - \tau_0)] \} \quad . \quad (4.32)$$

The parameters describing this equation are

- a_τ : attenuation coefficient given in units of [dB/ μ s],
- τ_0 : delay of the LOS component given in units of [μ s],

τ_B : cut-off delay given in units of $[\mu s]$.

P_0 : the reference power level for the clusters¹³.

4.5 Interacting Object Distribution and Weighting

This section describes various strategies for a proper placement and weighting of the IOs inside a cluster. The combination of the positioning and the weighting of the IOs results in specific angular-delay power-spectra (ADPS) for each cluster. Such ADPS are, for example, defined for the COST 259 and COST 273 channel model. Usually the intra-cluster delay spread is defined as single-exponentially decaying whereas the azimuth-spread has a Laplacian shape [6]. While an exponential shape of a cluster in delay is well accepted, the Laplacian shape in azimuth is questionable. The Laplacian shape of the angular spectrum is often assumed (e.g. in [105]) but it has been shown in [106] that the azimuth estimates obtained from high resolution algorithms show a heavy-tailed distribution. This affects the accuracy of the azimuth spread estimation. I therefore focus in the following on the PDP for my investigations on the IO distribution and weighting rules.

4.5.1 Local Clusters

A disk around the MT defines the local cluster region. The center of the disk is the position of the MT. The local cluster consists of IOs around the MT. When the MT moves, the IOs remain static. These IOs correspond to objects in the surrounding of the MT like houses or vegetation, and are therefore fixed in space. In a first step the IOs are placed inside the cluster based on a distribution function. In a second step the IOs are weighted according to specific rules. The simplest distribution function for the placement is a uniform distribution. Other distribution functions like a von Mises distribution or a Gaussian distribution can be applied as well. However there are convincing arguments for a uniform placement of IOs inside the local cluster:

To ensure a local cluster around the MT even after large movements of the MT, the IOs that drop out of the vicinity of the MT have to be replaced. This replacement has to be a continuous process to avoid discontinuities of the receive signal. Already the replacement of a single IO may cause discontinuities. To get a smooth signal gradient I first set the weight of an outdated IO to zero. Therefore the corresponding

¹³see Section 4.11 for more details on the power normalization of the whole model.

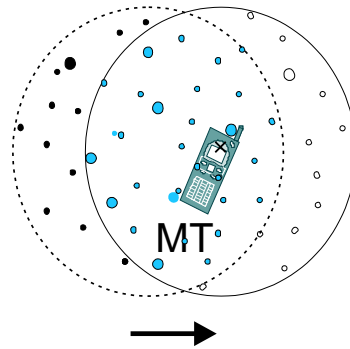


Figure 4.17: Replacement of IOs within the local cluster. Old (black) IOs are dropped and new (white) IOs are placed within the new area [39].

MPC fades out over one LS-update which corresponds to several wavelengths. Then I reposition the IO but keep its weight at zero. In a third step I set the weight factor of the IO to its proper value. Only one step is performed per LS-update and therefore these three steps represent a smooth fade-out of outdated IOs and a fade-in of new IOs like in reality. For a uniform distribution the principle of the repositioning of the IOs is illustrated in Figure 4.5.1.

IOs which drop out of the cluster area are replaced inside the new area. The new area for distributing the new IOs has the shape of a sickle. There is no closed-form solution for a uniform distribution of objects within a sickle. To get uniformly distributed IOs inside a sickle I use a uniform distribution within a circle and omit all the IOs which are not inside the sickle.

If I take a different distribution function for the placement of the IOs, the replacement of IOs dropping out of the cluster is not sufficient. The cluster position changes and therefore also the origin of the IO distribution. To retain the distribution function additional IOs inside the whole cluster area have to be replaced. A placement according to, e.g., a Gaussian distribution requires additional IOs close to the new cluster center and less IOs around the old center of the distribution function. I am not aware of any algorithm which handles this task. Even if such an algorithm exists, the number of repositioned IOs would increase dramatically. Such a replacement would also contradict the previous assumption of IOs fixed in space. I have therefore chosen

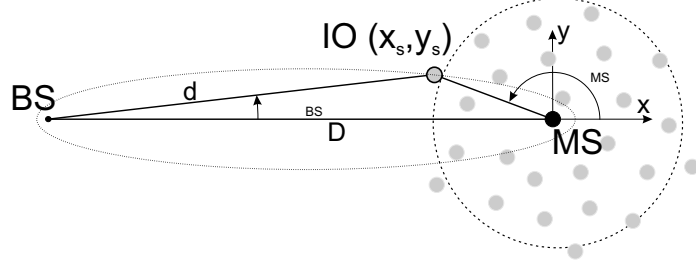


Figure 4.18: Definition of distances for the PDP-ADPS transformation.

the uniform distribution for the local cluster¹⁴. The only exception, where other distributions of IOs for the local cluster seem possible, are simulations that cover only minor movements of the MT which do not require any repositioning of the IOs.

In the following I will discuss various weighting strategies for the local cluster. The weighting of all the IOs of a cluster has to be performed after each repositioning of IOs.

Weighting of IOs using the Jacobi-determinant

To realize a predefined ADPS the IOs have to be weighted according to their positions. The Jacobi-determinant is used to transform probability densities [41]

$$PDF_2(x_s, y_s) = PDF_1(\tau(x_s, y_s), \phi_{BS}(x_s, y_s)) J(x_s, y_s), \quad (4.33)$$

where x_s and y_s denote the position of the IOs in space, τ is the delay of the MPCs, ϕ_{BS} is the receive angle of the MPC in azimuth, and J is the Jacobian-determinant:

$$J(x_s, y_s) = \begin{vmatrix} \frac{d}{dx} \phi_{BS}(x_s, y_s) & \frac{d}{dx} \tau(x_s, y_s) \\ \frac{d}{dy} \phi_{BS}(x_s, y_s) & \frac{d}{dy} \tau(x_s, y_s) \end{vmatrix} \quad (4.34)$$

Figure 4.18 shows the corresponding geometric relations and describes the case in which the ADPS at the BS is transformed into the weights of the IOs according to their distribution in space.

¹⁴I recommend the uniform IO distribution for all moving clusters of a channel model. However, I do not use other moving clusters since the movement of clusters over time is not explored up to now.

I will illustrate the idea of the Jacobi-determinant for the local MT cluster in the uplink case. After some manipulations the relation between the variables can be written as

$$x_s(\tau, \phi_{\text{BS}}) = \frac{D^2 - (\tau c)^2}{2D - 2\tau c \sqrt{1 + \tan^2(\phi_{\text{BS}})}} - D, \quad (4.35)$$

$$y_s(\tau, \phi_{\text{BS}}) = \frac{(D^2 - (\tau c)^2) \tan(\phi_{\text{BS}})}{2D - 2\tau c \sqrt{1 + \tan^2(\phi_{\text{BS}})}}. \quad (4.36)$$

and the Jacobi-determinant becomes

$$J(x_s, y_s) = \frac{x\Delta D + x^2\Delta + \Upsilon D^2 + 2\Upsilon D x + \Upsilon x^2 + y^2\Delta + y^2\Upsilon}{\Delta^3\Upsilon}, \quad (4.37)$$

where $\Delta = \sqrt{D^2 + 2Dx + x^2 + y^2}$, and $\Upsilon = \sqrt{x^2 + y^2}$. Equation (4.33) can now be rewritten as

$$A(x_s, y_s) U(x_s, y_s) = \text{ADPS}(\tau(x_s, y_s), \phi_{\text{BS}}(x_s, y_s)) J(x_s, y_s). \quad (4.38)$$

To calculate the IO-weights the inverse function of the IO-distribution is required. This implies that the distribution function of the IOs is nonzero over the whole xy-plane, which contradicts the assumption that IOs only occur within a limited area around the cluster center. As long as the Jacobi-determinant is small outside the cluster the resulting error in the ADPS will be small as well. But the Jacobi-determinant for the ADPS-transformation has a pole at the position of the BS. Therefore IOs in the vicinity of the BS have significant impact on the resulting ADPS. But the MT cluster has no IOs close to the BS¹⁵.

Figure 4.20 shows the weighting factors for a uniform IO distribution, exponential decay in delay and double-sided Laplacian shape in azimuth.

If IOs are now limited to a cluster around the MT and one applies the Jacobi transformation, the resulting ADPS has significant deviation from the required ADPS. The required weight factors for uniformly distributed IOs and an ADPS defined by an exponential decay in delay and double-sided Laplacian shape in azimuth is shown in Figure 4.20. The highest weight factors occur for the IOs around the BS and close to the LOS between BS and MT.

To obtain the required shape of the ADPS the cluster definition of the GSCM has to be adapted. If I assume still a channel model using single-interaction clusters only,

¹⁵It may happen that the BS is positioned inside the MT cluster if the MT moves close to the BS. However, this is not the usual case.

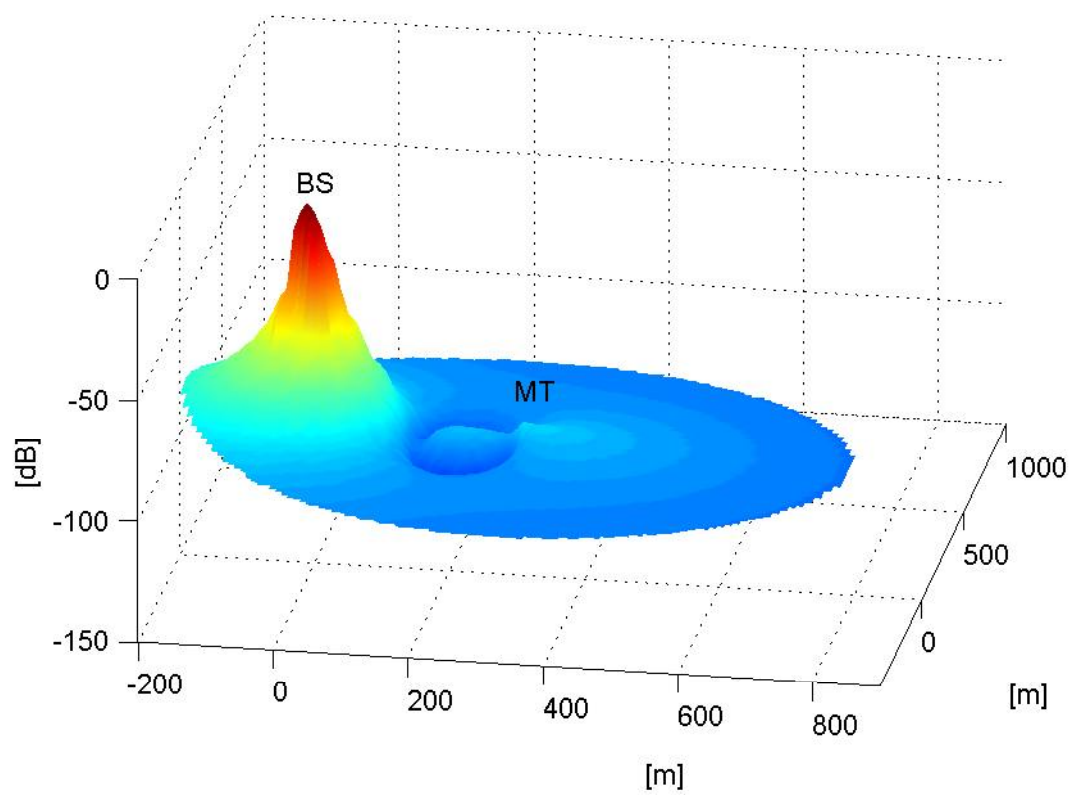


Figure 4.19: An example of the Jacobi-determinant in space.

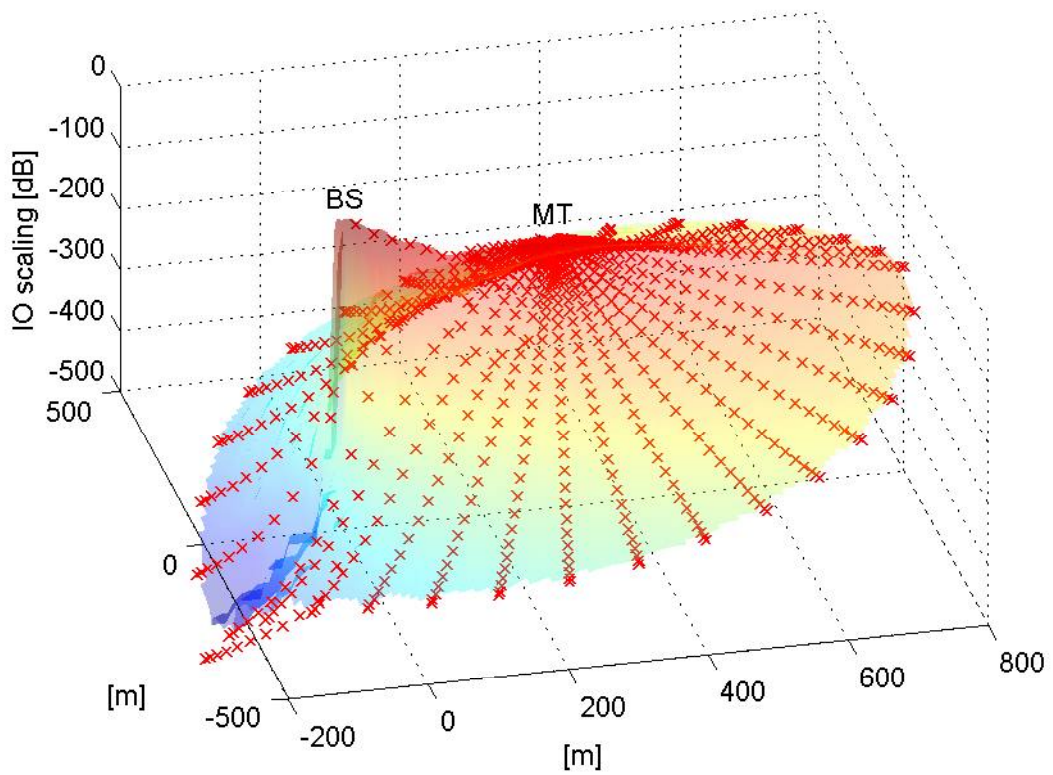


Figure 4.20: Weighting of uniformly distributed IOs for an exponential decay in delay and double-sided Laplacian shape in azimuth.

MPCs interacting around the MT, as in the standard model, plus around the BS and in the surrounding of the LOS have to be taken into account. The resulting PDP then shows the predefined exponential decay. Grouping the whole area covering IOs of significant strength results in a new, extended cluster. But I prefer clusters which are limited in space. With this new definition of a cluster a cluster is no longer a separate region and all clusters overlap at the BS. IOs in the vicinity of the BS sound reasonable for picocells and microcells but there is no reason for interacting objects around a macro-cellular BS. Even though the resulting PDP looks very promising this approach is not continued since it contradicts my definition of a cluster.

The exact match of the ADPS is not possible for clustered IOs. In [107] some other weighting strategies are discussed and analytical results are given for a uniform distribution, a Rayleigh-distribution and a one-sided Gaussian distribution. The uniform distribution performs worst but requires the smallest computational effort. In the following I will describe the IO-distributions I have tested.

Uniform Weight Distribution

A uniform distribution of IOs inside a cluster and uniform weighting of the IOs is the easiest possible solution. The resulting ADPS depends on the size of the cluster and the distance between MT and BS.

As an extension, the weighting of the IOs can be performed following a Ricean distribution which gives more realistic results especially for small sets of IOs inside a cluster. For only very few IOs and large bandwidths the impulse response tends to look like a rectangular function resulting from just one IO contributing to each delay bin. It may get even worse and the PDP rises for larger delays since the probability of IOs inside a delay bin increases with increasing delay due to increasing cluster area contributing to larger delays. Figure 4.21 shows the PDP of such a uniform IO weighting of a 4-times oversampled UMTS signal. This distribution is a too strong simplification and should not be used.

Exponential Weighting in Delay

This is my preferred weighting strategy for the local cluster around the MT. It combines limited complexity with quite accurate matches of an exponentially decaying PDP.

I assume a uniform IO distribution in space, and the IOs are weighted according to their delay

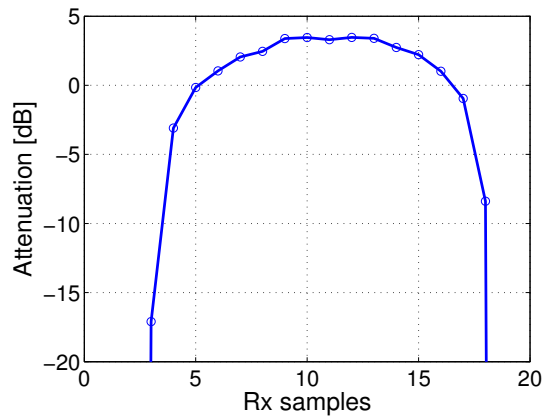


Figure 4.21: PDP of a cluster for the uniform IO weighting of a 4-times oversampled UMTS signal.

$$A(\tau) = A_0 e^{-\tau/\tau_0}, \quad (4.39)$$

where A_0 denotes the basis weight and τ_0 is the decay constant for the weighting process. In Figure 4.22 a result for the GTU environment [6] and a UMTS system is given. The PDP is slightly steeper than exponential. The drop off after about 5 UMTS symbols is due to the size of the cluster which does not allow for larger delays since the delay of the MPCs is based in geometric considerations. However, taking the low complexity of this approach into account, the resulting PDP matches the exponential decay quite well.

Figure 4.23 shows the distribution of the weighting factors for the IOs of the local cluster around the MT for a set of 100 IOs. In logarithmic scale the CDF is nearly linear over several decades of dB. IOs with a very low weight factor do not contribute to the impulse response. Thus, the number of contributing IOs to the impulse response is smaller than the number of IOs within the cluster.

In [108] a set of 20 IOs per cluster was extracted out of measurements. A set of 20 IOs per cluster is also defined in the COST273 channel model. I have chosen to double the number to 40 IOs for the local cluster to account for the strong imbalance of the cluster weights for this weight distribution¹⁶. This set of 40 IOs can be seen

¹⁶For all other clusters smaller numbers of IOs are sufficient due to a different distribution and weighting approach which will be discussed in detail in the next section.

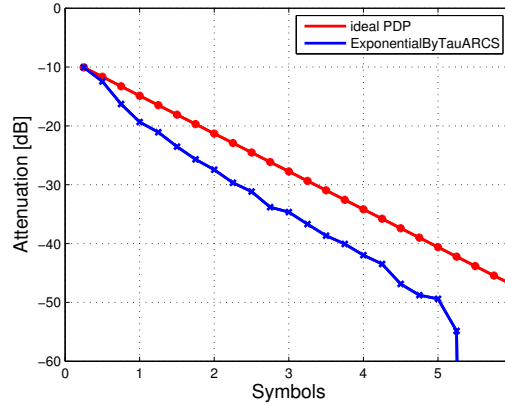


Figure 4.22: PDP for the exponential weighting of the IOs according to their delay.

as a lower bound for simulations. In Section 5 I will show that this setting provides reasonable results.

Exponential Weight Distribution in Space

An additional alternative is to use exponential weighting according to the distance of the IOs to the cluster center

$$A(\tau) = A_0 e^{-r/r_0}, \quad (4.40)$$

where r_0 is the standard deviation of the radius of the cluster (according to the delay spread and angular spread) and r denotes the distance of the IOs to the cluster center. This distribution is described in [107] as well. The method is very simple but obtains worse results than the weighting in delay. From my point of view the enhanced simplicity is not worth to favor this weighting law.

4.5.2 Single-interaction Cluster

The weighting of the IOs of a single-interaction cluster is done in analogy to the local clusters. In principle, the Jacobian determinant can be computed by an update of the geometric behavior using the path across the cluster center as the reference path and neglect all shorter paths. This means that the weights of all MPCs shorter than the path through the center are set to zero. For all other MPCs the weights are computed using the Jacobian determinant. Since the single-interaction clusters are

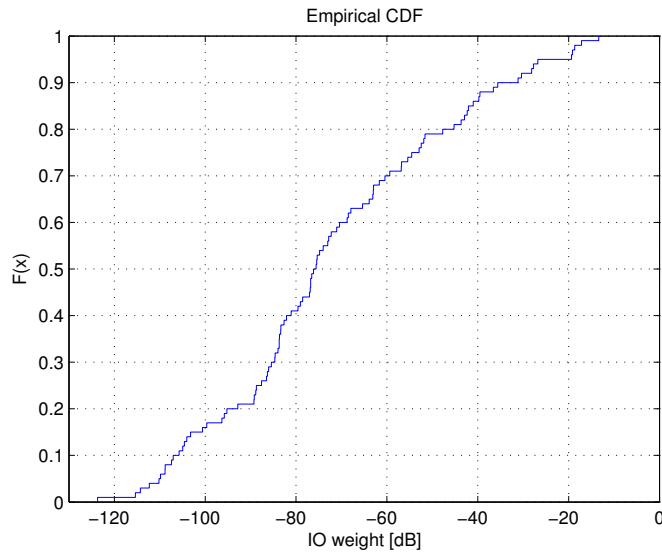


Figure 4.23: IO weights of the local MT cluster for the exponential weight distribution in delay.

fixed in space no repositioning of the IOs is necessary. Due to the movement of the MT the MPCs change, and therefore the weights change as well. They are calculated by the Jacobian-determinant, which requires a periodic update.

In principle, all other IO distribution and weighting algorithms, as described for the local clusters, can be applied as well. Since the single-interaction clusters are fixed in space one is not limited to uniformly distributed IOs in space but can use other distribution functions as well. I will now describe the distribution and weighting of IOs as it is specified in COST 273.

In COST 273 the ADPS of a cluster is defined as in COST 259 as an exponential function in delay and Laplacian shape in azimuth. In addition there is a recommendation to distribute the IOs inside a cluster as truncated Gaussian and weight them according to a Ricean distribution. This is, of course, only a rough approximation of the ADPS but gives realistic results. Since I have shown that an exact match of the ADPS using the Jacobi-determinant is not possible, the truncated Gaussian distribution in space plus a Ricean distribution of the MPC weights is my preferred distribution for single-interaction clusters. From my point of view, a truncated Gaussian distribution of IOs for the local cluster is not possible due to the necessary repositioning of the IOs. In contrast to the local cluster all IOs contribute substantially to the impulse response due to the Ricean distribution of their weights. Therefore

the required minimum number of IOs for the single-interaction cluster is smaller. If a cluster is so small that all its IOs contribute to the same delay bin of the impulse response 6 – 7 IOs are sufficient to ensure Rayleigh fading [6]. If a cluster is larger it has to be ensured that at least 6 – 7 IOs contribute to each delay bin of the impulse response. As a rule of thumb one can say that 20 IOs per single-interacting cluster show realistic results.

4.5.3 Twin Cluster

For the twin clusters I use a placement of the IOs inside the cluster following a specific rule to ensure the predefined size of angular and delay cluster spreads. First, IOs are distributed according to a three-dimensional Gaussian distribution with variance $\sigma = 1$ inside a sphere

$$\vec{r} = \mathcal{N} \left(0, \begin{pmatrix} 1 & 0 & 0 \\ 0 & 1 & 0 \\ 0 & 0 & 1 \end{pmatrix} \right), \quad (4.41)$$

where \mathcal{N} denotes a Gaussian distribution. This distribution of IOs is then transformed separately to the BS-side cluster and the MT-side cluster by

$$\vec{r}_{C,IO}^{\text{BS}} = \vec{r} \begin{pmatrix} d_C \\ d_C \\ h_C^{\text{BS}} \end{pmatrix} \mathbf{T}(\phi_{\text{BS}}, \theta_{\text{BS}}), \quad (4.42)$$

$$\vec{r}_{C,IO}^{\text{MT}} = \vec{r} \begin{pmatrix} d_C \\ d_C \\ h_C^{\text{MT}} \end{pmatrix} \mathbf{T}(\phi_{\text{MT}}, \theta_{\text{MT}}), \quad (4.43)$$

where \mathbf{T} denotes the rotation matrix in space:

$$\mathbf{T}(\phi, \theta) = \begin{pmatrix} \cos(\phi) \cos(\theta) & -\sin(\phi) & \cos(\phi) \sin(\theta) \\ \sin(\phi) \cos(\theta) & \cos(\phi) & \sin(\phi) \cos(\theta) \\ -\sin(\theta) & 0 & \cos(\theta) \end{pmatrix} \quad (4.44)$$

The rotation of the cluster is also depicted in Figure 4.24. This approach differs slightly from the COST 273 approach where an additional rotation of the IOs at the

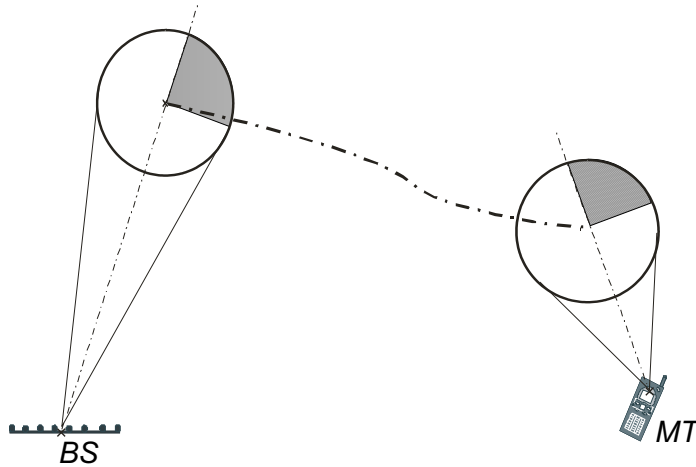


Figure 4.24: The additional rotation of the twin cluster at the MT compared to the BS side.

MT side was proposed. It turned out that the additional rotation, as in COST273, is not necessary for realistic PDPs.

4.6 LOS Component

In addition to the clustered IOs a LOS path exists. This LOS component exists all the time, however it may get very weak. The LOS path is always the component with the shortest delay of the whole link. That there is an omnipresent LOS component does not mean that only LOS scenarios can be modelled. The LOS component included in NLOS environments is very weak. This weak LOS component is mainly used as a reference path for the simulation and has no further influence on the impulse response. In accordance to the computation of the MPC gain factors of the IOs (4.20) the MPC gain factor for the LOS component is based on the same considerations:

$$\mathcal{A}_{VV,LOS} = A_{SF,LOS} A_{LOS,corr} K_{LOS}. \quad (4.45)$$

K_{LOS} denotes the LOS power factor¹⁷. and $A_{SF,LOS}$ is the shadow fading of the LOS component, which is usually set to the same value as the shadow fading of the local

¹⁷Note that the LOS power factor is often called the Rice factor in channel modelling literature (e.g. in COST 259). But the two factors are not necessarily the same. The LOS power factor is defined as the energy of the LOS component divided by all other MPCs. The Rice factor on the other hand is defined by the shape of the Ricean distribution. This is true as long as the receive signal of the MPCs is Rayleigh distributed. However with only view (dominant) MPCs the receive signal is no longer Rayleigh itself but adds an additional Ricean component to the receive signal.

cluster around the MT. A correction value $A_{\text{corr,LOS}}$ is assigned to the LOS component as well. This parameter adjusts the large-scale pathloss of the LOS component. The computation of this parameter is discussed in Section 4.11.

To distinguish between the LOS and the NLOS case, LOS visibility regions according to the concept of the visibility regions for the far clusters (Section 4.3) are used [66]. The major difference is that the probability for an LOS decreases strongly with the distance of the MT from the BS, and is zero after a cutoff distance d_{co} . The LOS visibility regions are thus described by the following parameters:

d_{co} [m]: cutoff distance for LOS,

R_L [m]: radius of visibility region for LOS,

L_L [m]: size of transition region for LOS visibility region.

Depending on the existence of a LOS connection, the LOS power factor varies. In either case it is modelled as a log-normal random variable, but the mean and variance are different whether there is a LOS or a quasi-LOS. The parameters are thus

μ_K is the mean of the LOS power factor, and

σ_K standard deviation of LOS power factor.

4.7 Polarization

Following physical realities, I assume that an IO does not only bounce a MPC but also causes depolarization. My main polarization is vertical polarization and the whole model is based on it. In the following I will describe the computation of the MPC gain coefficients $A_{\text{VH},s}$, $A_{\text{HV},s}$, and $A_{\text{HH},s}$ based on $A_{\text{VV},s}$ of (4.15). I will neglect the IO-index 's' in the following for better readability.

Starting from vertical polarization I define a cross polarization discrimination (XPD) value $\alpha_{\text{XPD,VH}}$ for each IO. This is modelled as a Gaussian process. In addition to the weighting, each cross-polarized component is assigned a random phase shift $\beta_{\text{XPD,VH}} \in [0, 2\pi[$ to ensure receive signals for different polarizations to remain uncorrelated. The MPC gain factors A_{VH} and A_{HV} are now defined as

$$A_{\text{VH}} = A_{\text{VV}}\alpha_{\text{XPD,VH}}e^{j\beta_{\text{XPD,VH}}}, \text{ and} \quad (4.46a)$$

$$A_{\text{HV}} = A_{\text{HH}}\alpha_{\text{XPD,HV}}e^{j\beta_{\text{XPD,HV}}} \quad (4.46b)$$

for each IO. Horizontally polarized components are weighted the same way using

Therefore the Rice factor can be seen as an upper bound of the LOS power factor.

the co-polarization discrimination factor $\alpha_{\text{VV-HH}}$ and, again, a random phase shift $\beta_{\text{VV-HH}} \in [0, 2\pi[$.

This way, the model stays compatible with other models that consider only one polarization. Note that a second polarization component comprises MPCs and therefore signal power, which is not accounted for single polarization attenuation models like the COST-Hata [62] model.

4.8 Shadow Fading

The shadow fading is modelled as a stochastic process depending on the movement of the MT. Only the absolute movement is watched. It is the same approach as in [6] and [60] and is implemented as a first order Markov model with the output sequence A_{SF}

$$A_{\text{SF}}(x + \Delta x) = A_{\text{SF}}(x) \cdot R(\Delta x) + \sqrt{1 - R^2(\Delta x)} \cdot Z, \quad (4.47)$$

where Z is a normally distributed stochastic process with zero mean and variance σ_{SF}^2 .

An exponential shape of the autocorrelation function with a correlation length d_{corr} , depending on the specific scenario, is assumed. Therefore the update function of the Markov model is an exponential function as well

$$R(\Delta x) = e^{-\frac{|\Delta x|}{d_{\text{corr}}} \ln 2}. \quad (4.48)$$

There are different realizations of the shadow fading process for different clusters, all having the same mean value and correlation length.

4.9 Delay/ Azimuth/ Elevation Dispersion

The clusters are characterized by their position, spread, power and shape. In COST 259 and COST 273 the cluster-specific large-scale fading and the delay and azimuth dispersion are correlated stochastic processes. The correlation within a random matrix \mathbf{Y} can be achieved by multiplication of an uncorrelated matrix \mathbf{X} with a Cholesky factorized matrix $\mathbf{\Upsilon}$ [109] under the assumption that \mathbf{X} is a white random sequence with variance $\sigma_{\mathbf{X}}^2$

$$\mathbf{Y} = \mathbf{\Upsilon} \cdot \mathbf{X}. \quad (4.49)$$

In this matrix each sequence (fading, delay and azimuth dispersion) is assigned to one row. In COST 259 the shadow fading, the delay and the azimuth spread at the BS are correlated. For the computation, the correlation matrix

$$\mathbf{\Gamma} = \mathbf{\Upsilon}\mathbf{\Upsilon}^T = \begin{bmatrix} 1 & \rho_{SF,\tau} & \rho_{SF,\varphi_{BS}} \\ \rho_{\tau,SF} & 1 & \rho_{\tau,\varphi_{BS}} \\ \rho_{\varphi_{BS},SF} & \rho_{\varphi_{BS},\tau} & 1 \end{bmatrix} \quad (4.50)$$

with the correlation coefficients $\rho_{SF,\tau} = -0.75$, $\rho_{\tau,\varphi_{BS}} = 0.5$ and $\rho_{SF,\varphi_{BS}} = -0.75$ is used. The correlation matrix $\mathbf{\Gamma}$ is required to be positive semi-definite, otherwise no solution exists. Then $\mathbf{\Upsilon}$ is the Cholesky factorization of $\mathbf{\Gamma}$, and $\mathbf{\Upsilon}$ is a lower triangular matrix. The Cholesky factorization satisfies the requirement $\sigma_X^2 = \sigma_Y^2$.

COST 273: In COST 273 the number of correlated parameters is extended to the MIMO case including the angular spread in azimuth at the MT as well as the elevation spread at BS and MT. Thus the correlation matrix becomes now a 6×6 matrix:

$$\mathbf{\Gamma} = \begin{bmatrix} 1 & \rho_{\tau,\varphi_{BS}} & \rho_{\tau,\varphi_{MT}} & \rho_{\tau,SF} & \rho_{\tau,\vartheta_{BS}} & \rho_{\tau,\vartheta_{MT}} \\ \rho_{\varphi_{BS},\tau} & 1 & \rho_{\varphi_{BS},\varphi_{MT}} & \rho_{\varphi_{BS},SF} & \rho_{\varphi_{BS},\vartheta_{BS}} & \rho_{\varphi_{BS},\vartheta_{MT}} \\ \rho_{\varphi_{MT},\tau} & \rho_{\varphi_{MT},\varphi_{BS}} & 1 & \rho_{\varphi_{MT},SF} & \rho_{\varphi_{MT},\vartheta_{BS}} & \rho_{\varphi_{MT},\vartheta_{MT}} \\ \rho_{SF,\tau} & \rho_{SF,\varphi_{BS}} & \rho_{SF,\varphi_{MT}} & 1 & \rho_{SF,\vartheta_{BS}} & \rho_{SF,\vartheta_{MT}} \\ \rho_{\vartheta_{BS},\tau} & \rho_{\vartheta_{BS},\varphi_{BS}} & \rho_{\vartheta_{BS},\varphi_{MT}} & \rho_{\vartheta_{BS},SF} & 1 & \rho_{\vartheta_{BS},\vartheta_{MT}} \\ \rho_{\vartheta_{MT},\tau} & \rho_{\vartheta_{MT},\varphi_{BS}} & \rho_{\vartheta_{MT},\varphi_{MT}} & \rho_{\vartheta_{MT},SF} & \rho_{\vartheta_{MT},\vartheta_{BS}} & 1 \end{bmatrix} \quad (4.51)$$

Since only very few correlations are already known from literature most entries of the matrix remain zero which means that there is no correlation between these parameters. I have chosen to use the approach of COST 273 since it suits better to my MIMO channel model. COST 259 focuses for this issue on a smart antenna system in the uplink and therefore gives only angular spread correlations at the BS side.

4.10 Parameter Updates

It is not feasible to compute the whole channel for each symbol with the exact values of all MPCs due to the high computational effort. Therefore the convolution of the input signal and the single MPCs is interpolated between sampling points. The interpolation of the MPC coefficients is described in Section 4.1.3. I will now describe

SS Update	
	Reposition MT
	Update shadow fading
	Update Rice factor
	Calculate path delays
	Interpolate attenuation areas
	Create path factors

Figure 4.25: The components of the SS-update.

how several model parameters are updated. In my approach I use a two step update process (Figure 4.2). In the SS-update all the fast changing variables are recalculated. The procedure of the SS-update is shown in Figure 4.25 and includes the repositioning of the MT, the calculation of the MPC lengths, and the interpolation of the parameters updated in the LS-update. The LS-update is illustrated in Figure 4.26 and keeps the slow changing parameters like the shadow fading, the repositioning of the local MT cluster, or the weights of the IOs.

This two-step update process seems to me the best compromise between accuracy and computational effort. Each parameter is updated after a time interval corresponding to its alteration rate.

4.11 Power Compatibility and Pathloss

Estimation of the narrow-band mean pathloss of a scenario can be done using well known pathloss models like the COST231 models [62] of Okumura-Hata, Walfish-Ikegami, and Feuerstein [63]. In this section I will describe a way how to normalize a geometry based model to fulfill the guidelines of such pathloss models.

Due to the multi-path propagation and the constructive and destructive superposition of MPCs the total receive power of a cluster for a single realization is somehow like a random number and depends not only on the power of the single MPCs but also on their phase and therefore their position. As a very simple approach I could

LS Update	
	Compute dispersion
	LOS visibility
	Cluster visibility
	Reposition near MT cluster and near MT IOs
	Compute near MT IO correction area
	Compute near BS IO correction area
	Compute far IO correction area

Figure 4.26: The components of the LS-update.

say: let's normalize each cluster power to the relative cluster power level as given by (4.32). In a next normalization step I can ensure that the total power fulfills the constraints of the pathloss model by normalizing all clusters by the same factor. But how about, e.g., shadow fading? I can take it into account and add it after the normalization procedure. This will work fine for the shadow fading, but only for a single position of the MT. If I assume a moving MT, the superposition of the MPCs will give different results depending on the position of the MT. The delay, and therefore the phase, of the different MPCs changes differently due to different angles of arrival at the MT. This inherent small scale fading is one of the big advantages of the geometry based modelling approach. Would I, in contrast, normalize each single snapshot of the impulse response to fulfill the pathloss model power constraint I would lose the small-scale fading. So this is not the way I want to proceed. I have to find a way that retains the small-scale fading. This implies that the pathloss given by e.g. the Walfish model is not reached by each single realization of my model but on average. As discussed above, normalization of the power of the cluster is difficult since the cluster power depends on the distribution of the MPCs and the position of the MT. Therefore I have to move one step lower in terms of model granularity and normalize the MPCs instead of the whole cluster. The MPCs are the basis of my channel model and the only part useful for the power normalization. Their MPC

gain is not influenced by a moving MT. And their normalization only influences the total power but has no effect on the small-scale fading. As a first conclusion I can say that an appropriate normalization of the power level of a geometry based model has to be performed by the normalization of the MPCs. In this context normalization of the MPCs means a global normalization of all MPCs with the same power correction factor $A_{\text{MPC,corr}}$. This factor was already introduced in (4.20). The only exception in terms of propagation paths in my model is the LOS component. This propagation path is normalized using the LOS correction factor $A_{\text{LOS,corr}}$ which was introduced in (4.45). The separation of the correction factors is the first step to achieve the predefined LOS power factor for the simulations on average¹⁸.

The goal of the normalization is now to ensure that the receive power of my model equals the narrow-band power of the chosen pathloss model on average

$$P_{\text{pathloss}}(d) = \mathbf{E}\left(\sum_{\tau=0}^{\tau_{\text{max}}} |h(\tau)|^2\right), \quad (4.52)$$

where $P_{\text{pathloss}}(d)$ denotes the pathloss given by the pathloss model and $h(\tau)$ is a single realization of the impulse response of my channel model. For a given environment the pathloss model only depends on the distance between the BS and the MT d . All other parameters used for the pathloss model, like the center frequency or the BS and MT height, are fixed by the chosen environment.

Since the pathloss changes over the BS-MT distance, also the MC simulation has to be performed for several possible distances within the simulation environment. The closest possible distance between the BS and the MT is usually given by the minimum distance specified by the chosen pathloss model. More details on the used pathloss models can be found in [62]. The maximum BS-MT distance is given by the cell size. In between I calculate the correction factors for a set of supporting points and use linear interpolation to obtain the correction values for a certain BS-MT distance. Every supporting point demands for a separate MC simulation. In (4.45) and (4.20) I have already introduced signal level correction factors for the calculation of the LOS signal strength and for the signal strength of the MPCs. In the following I will show a way on how to compute these values based on a Monte-Carlo simulation.

Due to the variety of stochastic processes in my model a closed form solution for the weights of the IOs and the LOS-weight is not feasible. I have therefore chosen a Monte-Carlo simulation to estimate the two weight factors based on two physical constraints: First, the sum of all receive power components (LOS plus MPCs) has to

¹⁸Note that the average LOS power factor is inherently given by the environment.

equal the power of the pathloss model

$$P_{\text{pathloss}} = P_{\text{LOS}} + P_{\text{MPC}} \quad (4.53)$$

on average. Second, the LOS power factor

$$K_{\text{LOS}} = \frac{P_{\text{LOS}}}{P_{\text{MPC}}}, \quad (4.54)$$

which is defined as the ratio of the power kept in the LOS component to the power of all the MPCs, has to fit the predefined value. With this two constraints I am able to compute the two unknown values of the weight factors $A_{\text{LOS,corr}}$ and $A_{\text{MPC,corr}}$. Therefore initial weight factors $\tilde{A}_{\text{LOS,corr}}$ and $\tilde{A}_{\text{MPC,corr}}$ are chosen arbitrarily and the receive power of a single realization of an environment is computed as the sum of the receive power of the LOS component plus the power of the MPCs

$$\tilde{P} = \tilde{P}_{\text{LOS}} + \tilde{P}_{\text{MPC}}, \quad (4.55)$$

where \tilde{P} denotes the estimate of the receive power using the initial correction factors $\tilde{A}_{\text{LOS,corr}}$ and $\tilde{A}_{\text{MPC,corr}}$. The correction factors $A_{\text{LOS,corr}}$ and $A_{\text{MPC,corr}}$ have to be adjusted in such a way that the overall pathloss \bar{P} equals the pathloss of the chosen pathloss model. In addition the quotient of the LOS component and the MPC components has to fit the LOS power factor (4.54), which is not the case for the first estimate using $\tilde{A}_{\text{LOS,corr}}$ and $\tilde{A}_{\text{MPC,corr}}$. To calculate these correction factors \tilde{P}_{LOS} is substituted via $\tilde{P}_{\text{LOS}} = K_{\text{LOS}}\tilde{P}_{\text{MPC}}$. Inserting the substitution of \tilde{P}_{LOS} into (4.55) yields

$$\begin{aligned} \tilde{P} &= K_{\text{LOS}}\tilde{P}_{\text{MPC}} + \tilde{P}_{\text{MPC}} \\ &= (1 + K_{\text{LOS}})\tilde{P}_{\text{MPC}}. \end{aligned} \quad (4.56)$$

Now the quotient of the computed receive power level \tilde{P} and the power level of the pathloss model P_{pathloss} equals the quotient of the instantaneous chosen correction values $\tilde{A}_{\text{MPC,corr}}^2$ to the desired correction values $A_{\text{MPC,corr}}^2$

$$\frac{\tilde{P}}{P_{\text{pathloss}}} = \frac{A_{\text{MPC,corr}}^2}{\tilde{A}_{\text{MPC,corr}}^2}. \quad (4.57)$$

Substitution of $\tilde{P} = (1 + K_{\text{LOS}})\tilde{P}_{\text{MPC}}$ yields

$$A_{\text{MPC,corr}}^2 = \frac{P_{\text{pathloss}}}{\tilde{P}_{\text{MPC}}(1 + K_{\text{LOS}})} \tilde{A}_{\text{MPC,corr}}^2. \quad (4.58)$$

The computation of the LOS correction factor $A_{\text{LOS,corr}}$ is now straight-forward in analogy to the MPC correction factor $A_{\text{MPC,corr}}$ and yields

$$A_{\text{LOS,corr}}^2 = \frac{P_{\text{pathloss}} K_{\text{LOS}}}{\tilde{P}_{\text{LOS}}(1 + K_{\text{LOS}})} \tilde{A}_{\text{LOS,corr}}^2. \quad (4.59)$$

For the Monte-Carlo simulation this procedure is performed several times with new realizations of the simulation environment. Equation (4.58) therefore becomes

$$A_{\text{MPC,corr}}^2 = \frac{P_{\text{pathloss}}}{\mathbf{E}\{\tilde{P}_{\text{MPC}}(1 + K_{\text{LOS}})\}} \tilde{A}_{\text{MPC,corr}}^2, \quad (4.60)$$

and (4.59) becomes

$$A_{\text{LOS,corr}}^2 = \frac{P_{\text{pathloss}}}{\mathbf{E}\{\tilde{P}_{\text{LOS}}(1 + 1/K_{\text{LOS}})\}} \tilde{A}_{\text{LOS,corr}}^2, \quad (4.61)$$

where $\mathbf{E}\{\cdot\}$ denotes the expectation. The expectations of the receive power of the LOS component and the receive power of the MPCs have to match the pathloss model and not the expectation of the correction factors since $\mathbf{E}\{x\} \neq \frac{1}{\mathbf{E}\{1/x\}}$.

There is now one additional circumstance I have to consider. Above calculations inherently assume that the LOS component and the MPCs are orthogonal in terms of receive signal power. But this is usually not true since the LOS component and parts of the MPCs slide into the same delay bin of my channel model. All MPC components are characterized by complex values denoting their phase rotation in space, the energy of the total sum of all MPCs is unequal to the energy carried by the single components due to the complex superposition of the signal vectors

$$\tilde{P}_{\text{MPC}} + \tilde{P}_{\text{LOS}} \geq \tilde{P}. \quad (4.62)$$

The effect is illustrated in Figure 4.27. In subplot (a) the total summation of all MPCs is shown. Subplot (b) shows the single LOS component and subplot (c) shows the signal of the MPCs only. It is obvious that the total energy of the LOS component and the MPCs is larger than the total receive power. Even the LOS component itself is larger than the total receive signal due to destructive superposition.

To take this effect in (4.60) and (4.61) into account an additional correction factor \tilde{p}_{corr} is required

$$\tilde{p}_{\text{corr}} = \frac{\tilde{P}}{\tilde{P}_{\text{MPC}} + \tilde{P}_{\text{LOS}}}. \quad (4.63)$$

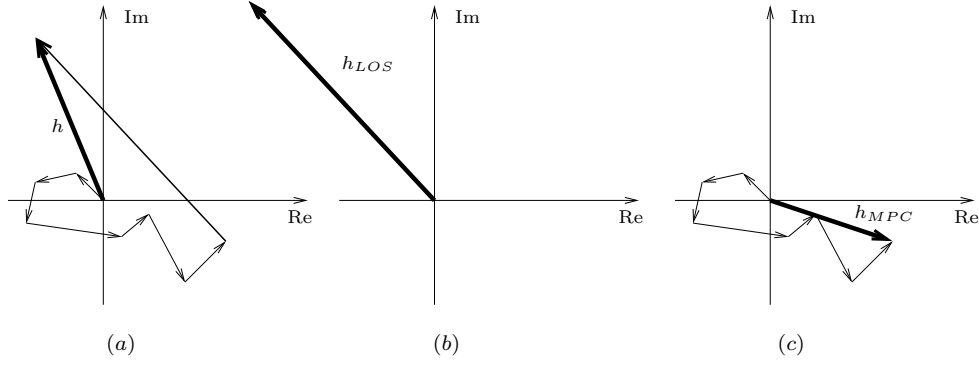


Figure 4.27: The complex summation of the MPCs and the LOS component. (a) the total summation of all MPCs, including the LOS component; (b) the single LOS component; (c) the signal of the MPCs.

Adding the correction factor to (4.60) and (4.61) yields

$$A_{\text{MPC,corr}}^2 = \frac{P_{\text{pathloss}}}{\mathbf{E}\{\tilde{P}_{\text{MPC}}\tilde{p}_{\text{corr}}(1 + K_{\text{LOS}})\}} \tilde{A}_{\text{MPC,corr}}^2, \quad (4.64)$$

and

$$A_{\text{LOS,corr}}^2 = \frac{P_{\text{pathloss}}}{\mathbf{E}\{\tilde{P}_{\text{LOS}}\tilde{p}_{\text{corr}}(1 + 1/K_{\text{LOS}})\}} \tilde{A}_{\text{LOS,corr}}^2. \quad (4.65)$$

Note that the power correction value \tilde{p}_{corr} changes from realization to realization. Therefore it has to be included in the expectation process.

Summed up this Monte-Carlo simulation ensures that the mean pathloss of a specific environment meets the specified pathloss model. Applying this approach to the model requires a new Monte-Carlo simulation each time a parameter of the model (e.g. number of MPCs) changes.

An example of the resulting weight factors for the MPCs is given in Figure 4.28. Simulations have shown that a mean error in the power level of my model compared to the pathloss model of less than 0.5 dB is achieved via a set of 200 realizations of a simulation environment.

There is no distinction between MPC gain factors of different clusters. The only distinction is between the MPCs and the LOS to ensure a reasonable LOS power factor. In addition to the MPC gain factors the mean pathloss of the environment, as given by the COST Walfish-Ikegami model [62], is plotted.

For a given environment the only changing parameter of a pathloss model is the distance between MT and BS. To get valid results over the whole simulation area the

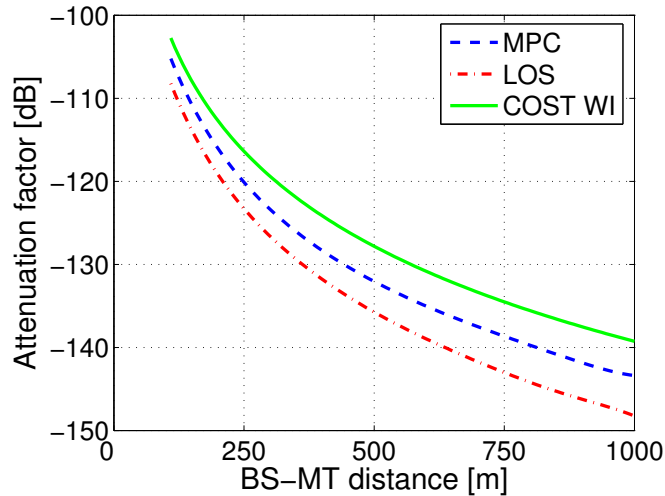


Figure 4.28: The weight factors for the MPCs as a function of the BS-MT distance. The green solid line denotes the COST Walfish-Ikegami reference value for the model. The red curve is the path gain factor for the LOS component whereas the blue curves denotes the MPC gain factor.

Monte-Carlo simulation has to be repeated for a set of all possible BS-MT distances. I use about 100 sampling points for this distance.

For the reader's convenience, all necessary steps for the calculation of the correction values are now summarized:

1. Set the MT to a certain distance from the BS.
2. Compute the pathloss P_{pathloss} for this distance.
3. Use initial values \tilde{A}_{LOS} and \tilde{A}_{MPC} to compute a single realization of the scenario.
4. The result of step 3 are the overall receive power \tilde{P} and the receive power obtained from the LOS, \tilde{P}_{LOS} , and the MPCs, \tilde{P}_{MPC} , for a certain realization of the scenario.
5. Repeat step 4 to get several realizations of the channel and therefore several estimates of the receive power of the scenario.
6. Apply (4.60) and (4.61) on the samples of \tilde{P}_{MPC} and \tilde{P}_{LOS} to get the correct correction factors A_{MPC} and A_{LOS} .
7. Repeat step 1 to 6 for the next BS-MT distance.

I want to stress that the pathloss models I use are specified for vertical polarization and omni-directional antennas which is only a subset of the functionality of the

GSCM. However, for the adjustment of the power levels the GSCM has to be adjusted to these limiting conditions.

I have chosen to normalize the pathloss in such a way that the power of the impulse response equals the power predicted by the pathloss model. This definition helps adjusting the noise floor for the testing of receive algorithms where the SNR is adjusted in accordance to the power of the impulse response.

The proposed power calibration scheme ensures realistic values of the receive power and can cope with any predefined LOS power factor. The model is able to reflect large-scale effects like shadow fading as well and allows for large MT movements in the range of the cell size.

4.12 Multi-User Case

A pure link-level simulation with just one user is not sufficient for a lot of state-of-the-art standards like UMTS. As soon as there is co-channel interference by other users their part should be modelled as well.

In contrast to many other models the GSCM is able to cope with multiple MTs and can model realistic signal interference of all users at the BS. In addition multiple BSs can be simulated as well, which allows the testing of soft-handover algorithms.

Adding several users to a simulation environment results in higher complexity. For the GSCM the complexity increases linearly with the number of terminals. If sets of MTs n_{MT} and BSs n_{BS} are used for one simulation the product $n_{\text{BS}}n_{\text{MT}}$ denotes for the complexity increase. The additional complexity is due to the number of MPCs that have to be computed.

For multi-user scenarios some new parameters have to be parameterized. For the COST 259 version of the GSCM I have chosen a simple approach based on physical considerations. The local environment around the MT is specific for the single MT but the far clusters, which typically result from high-rise buildings are the same for all users. Therefore the correlation of the receive signal depends on the power ratio between the local cluster and the far clusters. If two MTs get overlapping local clusters the MPCs of their clusters do not become the same. Each MT propagates via its own IOs. Additional white Gaussian noise can be added to each BS-MT link. The SNR level can be adjusted for each link separately. This ensures compatibility with, e.g., the 3GPP spatial channel model [59].

Chapter 5

Channel Model Validation

In this chapter I will discuss the validation of my channel model in detail. A Matlab implementation of the core part of my model is available at [110]. This code has been used for most of the computations of this chapter. It covers the distribution of both types of far clusters, namely twin clusters and single-interaction clusters as well as local clusters and an LOS component. The distribution of MPCs inside a cluster is based on a 3-dimensional Gaussian distribution. The available Matlab code does not cover polarization, directional antennas, and does not include any update routines for the channel parameters. Furthermore all impulse responses are normalized to a mean power of unity. Therefore this implementation is only valid for small movements of the MT. Furthermore it covers only the single user case. A real time implementation of the full COST 273 model, covering all the above excluded features, is available from ARCS Austrian Research Centers Seibersdorf [111].

How to Validate a Channel Model

The validation of a channel model has to be done for several aspects. My model covers various parameters and validating a single parameter is not sufficient. A channel model is not built to reflect model parameters but has to reflect nature in a most appropriate way. Therefore the validation of my model is based on the validation of physical properties of the channel.

Figure 5.1 shows a simulated time-varying impulse response of a channel at a center frequency of 2 GHz and a bandwidth of 40 MHz¹. This figure allows a first qualitative test of the channel model. The plot shows several time-varying MPCs with decreasing

¹The bandwidth of 40 MHz was chosen for a better delay resolution of the impulse response compared to a standard UMTS channel with 5 MHz bandwidth.

power for larger delays. It looks very similar to plots known from channel sounder measurements.

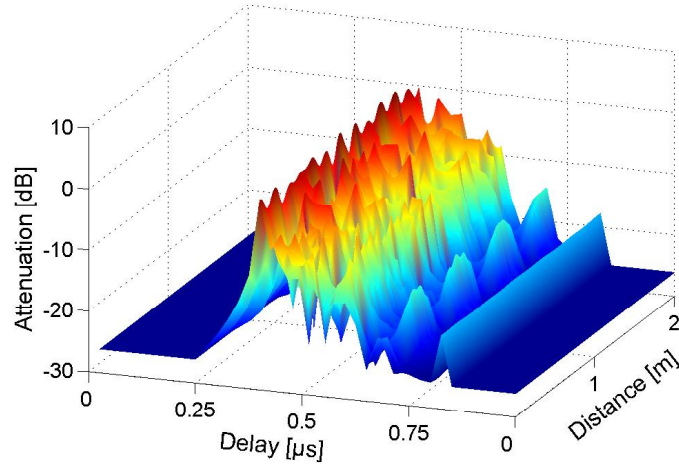


Figure 5.1: Impulse response over time with a channel bandwidth of 40 MHz.

In the following I will give a more detailed analysis of my channel model. I will start with the analysis of the amplitude and phase statistics of the receive signal as well as its transfer function and the Doppler spread. Realistic values of the MIMO capacity are also one important parameter if the model is used for MIMO applications. Testing MIMO capacity is one test among many for the validation of a channel model. It is not sufficient to test MIMO capacity only. As the last part of my model validation I will show results on the BER performance of a receive algorithm using my channel model. As long as not otherwise stated I will use the COST 273 large urban macrocell (LUM) environment and the UMTS [112] specifications for the validation of my model. Table 5.1 summarizes the most important simulation parameters. A comprehensive list of parameters is given in Appendix A for the LUM environment and the PCH environment. These are the two parameter sets I have used for the validation of my model.

5.1 Replacement of IOs

Before starting with the evaluation of propagation relevant parameters I will validate my replacement strategy for the IOs of the local cluster. The proper placement of IOs is crucial for achieving realistic simulation results.

Parameter	Value
Center frequency	2 GHz
Bandwidth	5 MHz
Symbol duration	$1/(3.84e6)$ s
Oversampling factor	4-times
Tx antenna elements	omni-directional, 0 dBi
Rx antenna elements	omni-directional, 0 dBi
No. of Tx antennas	4
No. of Rx antennas	4
MT speed	50 m/s

Table 5.1: Simulation parameters for the validation of the model.

For the local cluster around the MT it is important that the distribution of objects within the cluster remains constant over time. Figure 5.2 shows the IO distribution for a large set of 500 IOs² after a movement of the MT of about 600 m using my implementation of my model. The IO distribution is still uniform, which validates my IO replacement strategy.

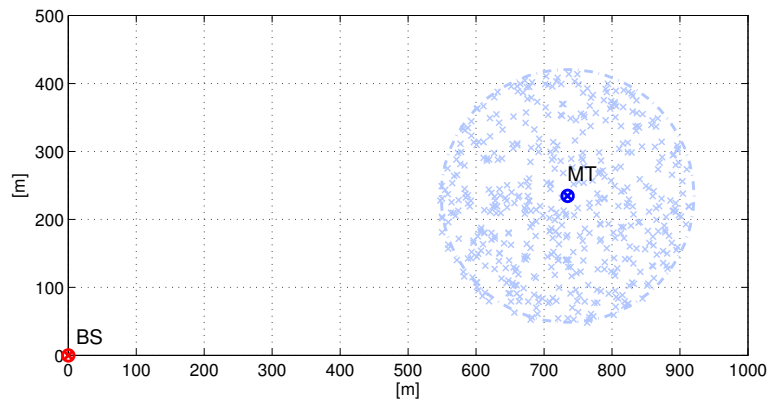


Figure 5.2: IO distribution of the local MT cluster after a movement of about 600 m.

²This large set of IOs was chosen to illustrate the uniform distribution. For usual simulations a set of 40 IOs for the local cluster is sufficient (see also Section 4.5.1 for further discussions).

5.2 Amplitude and Phase Statistics

In the NLOS case a Rayleigh distribution of the receive signal amplitude is assumed due to the multi-path propagation of the channel without any dominant component [24]. Figure 5.3 shows the amplitude distribution in the NLOS case for my model. It fits very well with the Rayleigh distribution, which is depicted as red dash-dotted line, and the two curves nearly overlap all the time.

If there exists an LOS component the amplitude statistics becomes Ricean due to the dominant LOS path. The amplitude statistic of a Ricean channel with a Rice factor of $K = 5.3$ is shown in Figure 5.4. It shows that the amplitude statistics of my model reflect the theoretic guidelines.

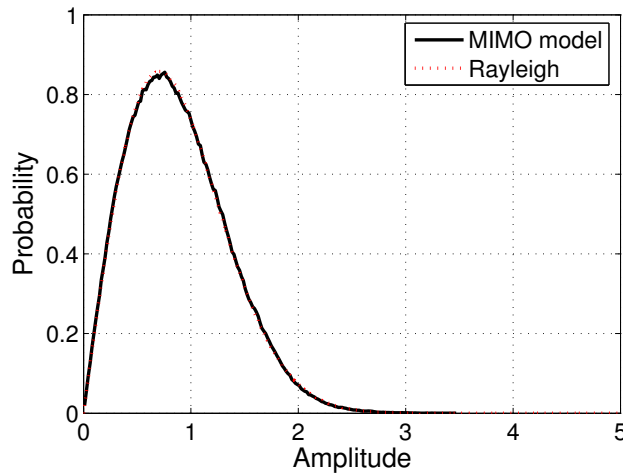


Figure 5.3: PDF of the amplitude of the receive signal in the NLOS case.

In Figure 5.5 the PDF of the receive signal phase averaged over several simulation runs is shown for the LOS case. As expected, the phase of the receive signal is equally distributed over 2π . A small jitter in the phase PDF is visible which is due to the finite number of simulation runs. Note that the phase PDF of a single realization of the channel is peaky for the Ricean channel and uniform for the Rayleigh case. The PDF of the phase for the Rayleigh (NLOS) channel averaged over several simulation runs looks identical to the PDF of the phase of the Ricean channel and is therefore not plotted.

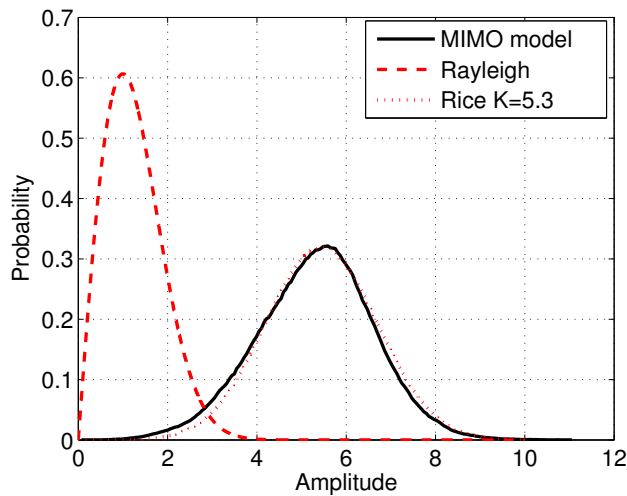


Figure 5.4: PDF of the amplitude of the receive signal in the LOS case with a Rice factor of $K_{LOS} = 5.3$. The Rayleigh distribution is plotted for comparison.

5.3 Transfer Function

The transfer function of the 4-times over-sampled receive signal is shown in Figure 5.6 for a single realization of the channel. The average transfer function (Figure 5.7) shows the shape of the receive filter, which is the standard UMTS root-raised cosine filter (4.11). The plotted single realization (Figure 5.6) demonstrates that the model itself is frequency selective. The average receive power over frequency however stays constant.

5.4 Doppler Spread

The Doppler effect is inherently included in the model due to its geometric nature. The maximum Doppler frequency depends on the speed of the MT. Since the MT is the only moving part of my model the maximum Doppler frequency

$$\nu_{\max} = \pm v_{\text{MT}} \frac{f_c}{c_0} \quad (5.1)$$

for a MT speed of $v_{\text{MT}} = 50 \text{ m/s}$ is $\pm 333 \text{ Hz}$ at a carrier frequency of 2 GHz. The Doppler spectrum of a single snapshot of the channel is given in Figure 5.8. It shows several peaks within the limits of the maximum Doppler frequency (red, dash-dotted lines) due to the various MPCs. The Doppler shift of a single MPC results from its

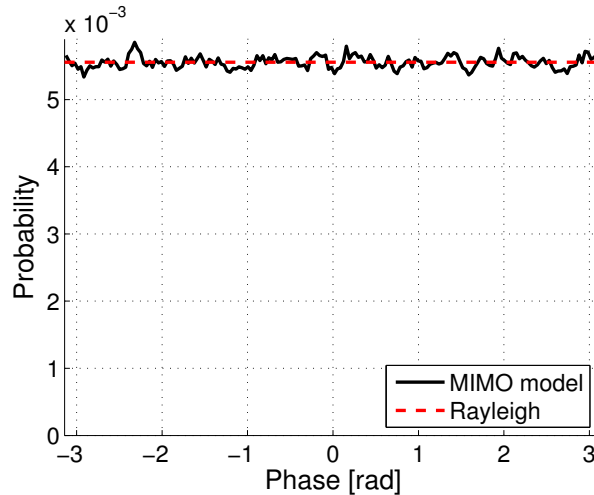


Figure 5.5: PDF of the phase of the receive signal.

position relative to the moving MT. The cosine of the angle of the line MT-IO to the movement vector of the MT is proportional to the Doppler shift

$$\nu_{\text{MPC}} = v_{\text{MT}} \cos(\phi_{\text{IO,MT}}) \frac{f_c}{c_0}. \quad (5.2)$$

In Figure 5.9 the mean Doppler spread, averaged over 500 channel realizations, is shown. For comparison the classical Jakes spectrum is plotted as well. The Jakes Doppler spectrum is defined by

$$S_{\text{D}}(\nu) = \frac{1.5 \bar{P}}{\pi \sqrt{\nu_{\text{max}}^2 - \nu^2}}, \quad (5.3)$$

whereas \bar{P} denotes the mean receive signal energy. The Jakes spectrum has two singularities at the maximum Doppler shift. These singularities are indicated in the simulated spectrum as well but not fully reached since this would require an infinite number of simulations. The two Doppler spectra do not match exactly, especially around the center. The Doppler spectra of my model does not show such a strong *bathtub*-shape as the Jakes spectrum, but flattens out in the middle of the spectrum. This is due to the fact that my model takes the elevation into account as well. In contrast the classical Jakes Doppler spectrum assumes purely 2-dimensional propagation conditions with IOs all around the MT and a vertical dipole as the antenna at the MT. To test the Doppler spectra of my model in more detail I have set all MPCs to the same height as BS and MT. This setup results in a 2-dimensional channel

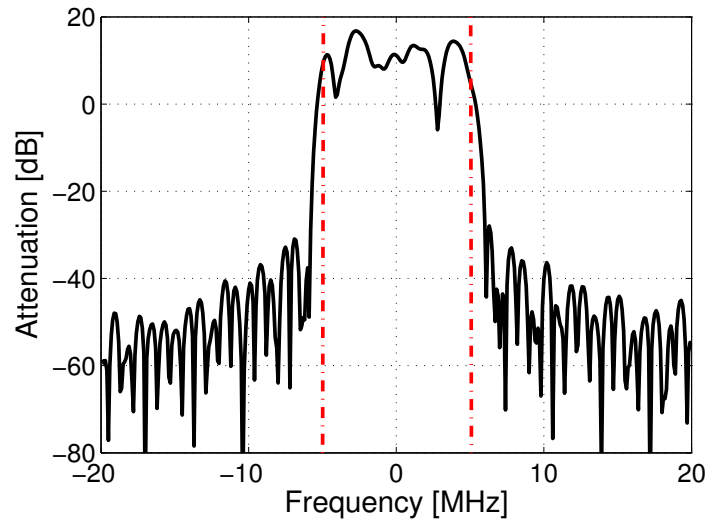


Figure 5.6: Transfer function of a single realization of the COST 273 LUM scenario. The UMTS bandwidth is depicted as red dash-dotted line.

model and the resulting Doppler spectrum has the same shape as the classical Jakes spectrum. The result of this test is shown in Figure 5.10. Taken the finite number of simulated snapshots into account the model fits very well with the classical Jakes spectrum.

The second extreme case for the Doppler spectrum is a fully 3-dimensional model where waves incident uniformly in all three dimensions [113]. In my model the angular spreads in elevation are smaller than in azimuth. Therefore the flattened bathtub is only visible around the center of the Doppler spectrum. The effect on the shape of the spectrum at the singularities is not that clearly visible due to the finite number of simulations and the resulting imperfect reproduction of the singularities. If I enlarge the angular spread in elevation to the same level as in azimuth I obtain a nearly flat Doppler spectrum (Figure 5.11). With increasing angular spread in elevation the spectrum flattens out more and more and the singularities diminish.

5.5 Small-Scale Fading

Small-scale fading is a result of the multi-path propagation of the wireless channel. Especially single antenna systems suffer from the, sometimes deep, fading dips. In Figure 5.12 the receive power levels of 4 antenna combinations using the first two Tx and Rx antennas of a 4x4 system with an antenna spacing of half a wavelength are

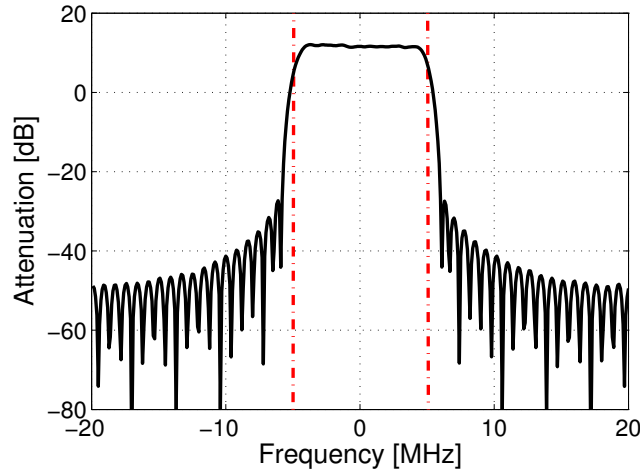


Figure 5.7: Transfer function averaged over 500 channel realizations of the COST 273 LUM scenario. The UMTS bandwidth is depicted as red dash-dotted line.

shown. The signals show the typical small scale fading with some deep fading dips. Signal energy of one antenna may fall down by about 15 dB for a short period in time due to destructive path superposition. In MIMO systems it is very unlikely that such deep fading dips occur for all antennas at the same point in time. Some correlation of the fading dips is visible in the Figure 5.12 due to the small spacing of the antenna elements of just half a wavelength.

5.6 Mutual Information

In Section 3.3.1 I have discussed the information theoretic MIMO capacity as a measure of the MIMO channel which describes the amount of information one can transmit per second and Hertz of bandwidth. Furthermore I have stated that the term mutual information [81] is better suited for the evaluation of measurements. This term reflects the fact that for a measured, or simulated channel, only single realizations of the channel are known but not the whole statistics of the channel³.

The mutual information of real world MIMO scenarios is typically smaller than

³One can argue that one knows the channel in detail if one models it. This is true up to a certain point. Calculating the MIMO capacity out of a complex channel model is not straight forward. But if one takes the (modelled) channel impulse responses for calculating mutual information one uses the same limited information of the channel as if one would estimate the mutual information out of measurements. In both cases only a limited information on the statistics of the channel is available.

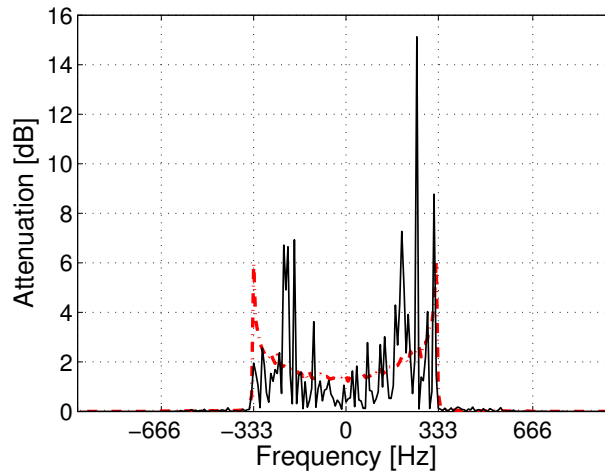


Figure 5.8: Doppler spectrum of a single realization of the channel. Single MPCs with different Doppler shifts are clearly visible.

the i.i.d. case (see also Section 3.3.3). This behavior is reflected by my model as well. In Figure 5.13 the mutual information of a 4×4 MIMO system is shown for the COST 273 LUM environment and antenna spacings of 0.1, 0.5, and 10λ . For this macro cellular environment the mutual information reaches about 8.5 bits/s/Hz on average. The CDFs of the simulations are steeper than for the capacity in the i.i.d. case. This is due to the Rice factor and reflects theory and measurement results [114]. An increasing Rice factor increases the deterministic component of the channel and therefore the steepness of the CDFs of the mutual information.

A large antenna spacing of 10λ does not result in significantly higher mutual information than an antenna spacing of λ half. The mutual information of the scenario is bounded by the constraints of the environment. A high BS with no IOs in the close vicinity limits the achievable maximum mutual information. This environmental limitation becomes better visible in Figure 5.14 where I have moderately changed the parameters of the LUM environment. For the tests I have added one additional cluster, or increased the angular spread of the clusters by a factor of 3, or increased the number of MPCs per cluster. All these variations do not show a significant variation in terms of mutual information⁴. Another result of these investigations is that my model is not sensitive to the number of MPCs per cluster. The standard set of 20

⁴Playing around with the parameters does not mean a complete change of the environment, but only slight changes.

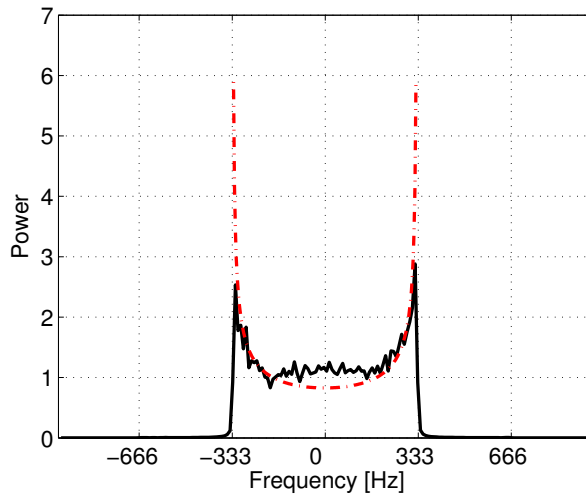


Figure 5.9: Mean Doppler spectrum of the LUM scenario averaged over 500 channel realizations. The classical Jakes Doppler spectrum is plotted as red dash-dotted line in addition.

MPCs per cluster shows the same mutual information even as 200 MPCs per cluster⁵. Therefore, this parameter does not seem to be of that importance for my model.

In contrast to the simulation results in the macro cellular case, the picocell environment (COST 273 PON) shows substantially higher capacity values. In Figure 5.15, again, a 4x4 channel is simulated and the mutual information for several antenna spacings is calculated. Already a spacing of $\lambda/2$ achieves a capacity that is about 80% of the i.i.d. case. With an antenna spacing of 2λ the i.i.d. capacity is nearly reached. The very small antenna spacing of $\lambda/10$ results again in a substantial loss of mutual information. Due to a low Rice factor the steepness of all the mutual information cdfs is now comparable to the i.i.d. case. All parameters of my model used for this simulations can be found in Annex A. Note that I have performed these simulations for antenna elements without antenna coupling.

5.7 Large-Scale Variations and Pathloss

As discussed in Section 4.11, my model on average reflects the attenuation of a given pathloss model. In Figure 5.16 the computed attenuation level of my model for the LUM environment is plotted over the distance between the BS and the MT. It shows

⁵There are only few results on the number of MPCs per cluster available in literature [108].

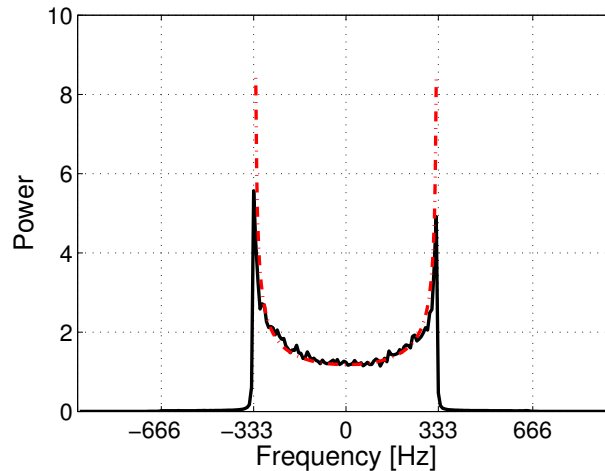


Figure 5.10: Mean Doppler spectrum of a 2-dimensional channel model averaged over 500 channel realizations. The classical Jakes Doppler spectrum is plotted as red dash-dotted line in addition.

the variation of the attenuation level due to the shadow fading and the increasing pathloss with the increasing BS-MT distance. For comparison the pathloss values, as given by the COST Walfish-Ikegami model [62], are plotted as well.

5.8 F-eigen-ratio

I use the F-eigen-ratio, as defined in Section 3.3.2, to validate the large-scale variations of my channel model. To get comparable results to the measurements I will use linear arrays of 8 elements for the BS and the MT. In Figure 5.17 a test case for the F-eigen ratio is shown where I have reduced my channel model to the LOS path as the only propagation mechanism. The MT starts at a distance of 200 m away from the BS and moves perpendicular to the distance vector. The F-eigen ratio for $F = 1, 2, 3, 4$ over the movement of the MT fits well with the theoretic curves for small angular spreads [14]. A more realistic scenario is evaluated for the F-eigen ratio in Figure 5.18. The two plots show single simulation runs of the LUM environment. For a MT movement of about 25 m the F-eigen ratio stays nearly constant but then drops rapidly.

To obtain a better comparison between the model and the measurements I use two metrics, the long-term time constant τ_{LT} and the WSS quality Q_{WSS} (see Section 3.3.3). The velocity of the MT was set to 4 km/h for all the simulations. Since the MT is the only moving part of my channel model this results in coherence times

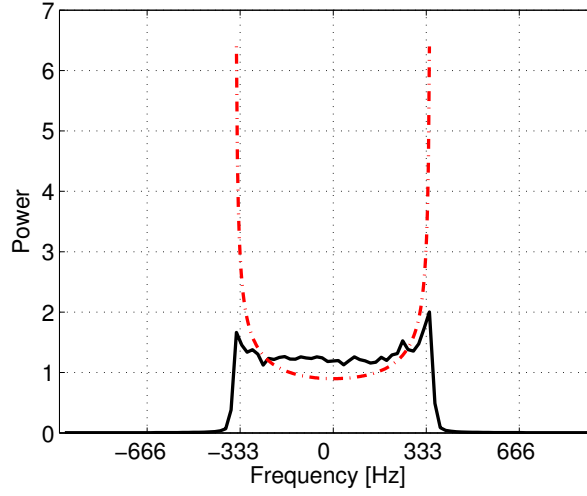


Figure 5.11: Doppler spectrum of a fully 3-dimensional channel model. The classical Jakes Doppler spectrum is plotted as red dash-dotted line in addition.

(Equation 3.10) of $\tau_{coh} = 180$ ms. The CDFs of the F-eigen ratio for the LUM, PCH, and POL environments and $F = 1, 2$ are shown in Figure 5.19 for various values of Δt . The spatial long-term time constant τ_{LT} is obtained from Figure 5.19 via visual inspection. A summary of the obtained parameters is given in Table 5.2 and Table 5.3 for the indoor and outdoor environments, respectively. These results are compared to the values obtained from the measurement data analysis. The agreement with the measurements is excellent, particularly the outdoor simulations show a very similar behavior to all the measurement results. The WSS Quality is always in the range between about 100 and 150, which seems to be a typical value for outdoor environments. In the indoor case the Q_{WSS} quality is slightly smaller in the POL environment compared to the measurements at Fornebu. This seems to be a result of the larger dimensions of the Fornebu office area compared to the specifications of the POL environment. Taken the dimensions of the simulated and measured areas into account, the Q_{WSS} values reflect the size of the area quite well.

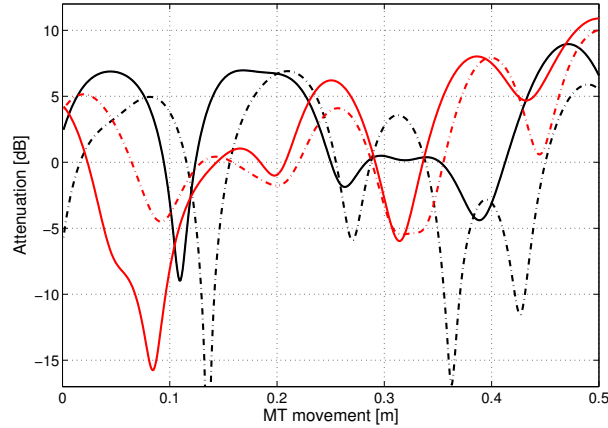


Figure 5.12: The receive power of 4 antenna combinations (the first 2 Rx and Tx antennas) of a 4×4 MIMO system. The curves including the first Tx antenna are plotted in red, the second Tx antenna is plotted in black. The solid lines denote for the first Rx antenna whereas the dash-dotted lines correspond to the second Rx antenna.

Environment	LUM	Kvadraturen* high BS	Kvadraturen* low BS	Vienna[15]
Long-term time constant τ_{LT}	26 sec	61 sec	73 sec	22.6 sec
MT speed v_{MT}	4 km/h	1 km/h	1 km/h	4 km/h
Coherence time τ_{coh}	180 ms	500 ms	540 ms	180 ms
WSS Quality Q_{WSS}	145	122	146	126

Table 5.2: Long-term time constant, Coherence Time and WSS Quality for the outdoor environments. Results marked with (*) are measurement results described in Section 3.3.3.

Environment	PCH	POL	Fornebu* office
Long-term time constant τ_{LT}	2.6 sec	1.1 sec	4.8 sec
MT speed v_{MT}	4 km/h	4 km/h	1 km/h
Coherence time τ_{coh}	180 ms	180 ms	540 ms
WSS Quality Q_{WSS}	15	6	9

Table 5.3: Long-term time constant, Coherence Time and WSS Quality for the indoor environments. Results marked with (*) are measurement results described in Section 3.3.3.

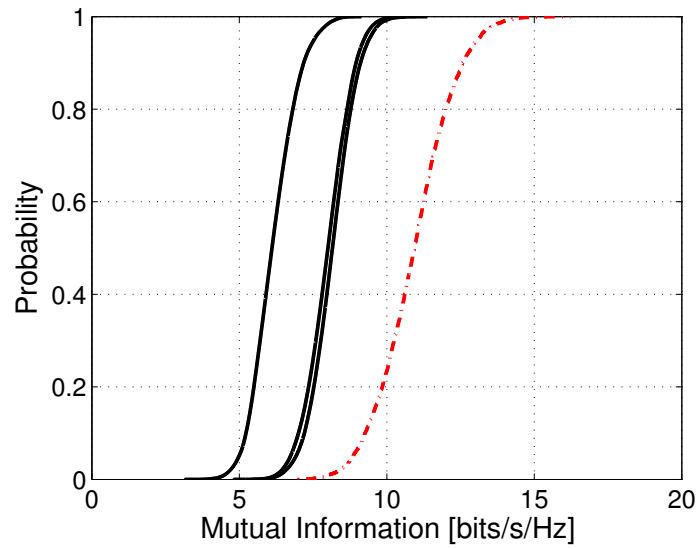


Figure 5.13: Mutual information of the LUM scenario for a 4x4 antenna MIMO system. The antenna spacing was set to 0.1, 0.5 and 10λ . The mutual information of the i.i.d. channel is given for comparison (red, dash-dotted line).

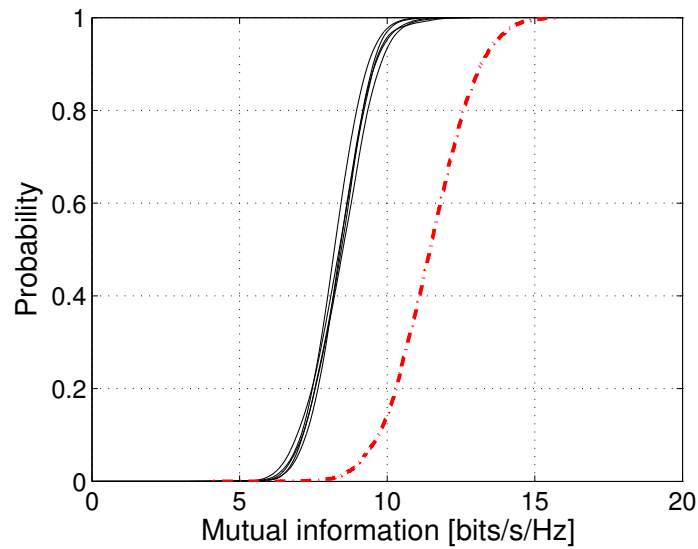


Figure 5.14: Mutual information of variations (one additional cluster, increase of the cluster angular spread, increased number of MPCs) of the LUM scenario for a 4x4 antenna MIMO system. The mutual information of the i.i.d. channel is given for comparison (red, dash-dotted line).

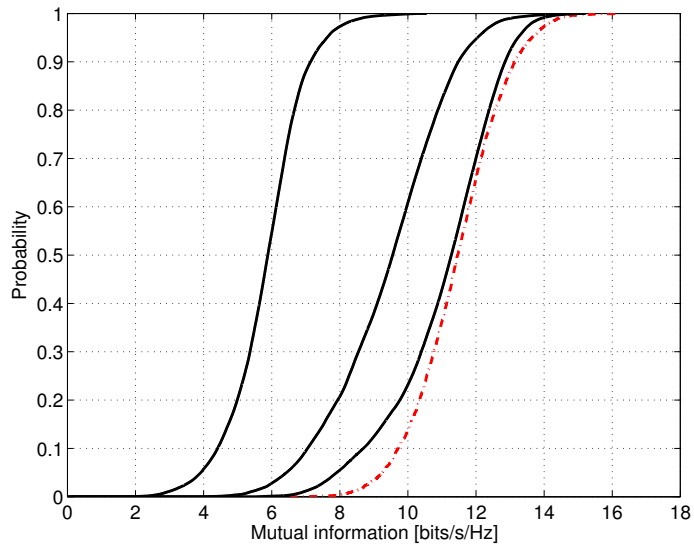


Figure 5.15: Mutual information of the PON picocell scenario for a 4x4 antenna MIMO system. The antenna spacing was set to 0.1, 0.2, 0.5, and 2λ . The mutual information of the i.i.d. channel is given for comparison (red, dash-dotted line).

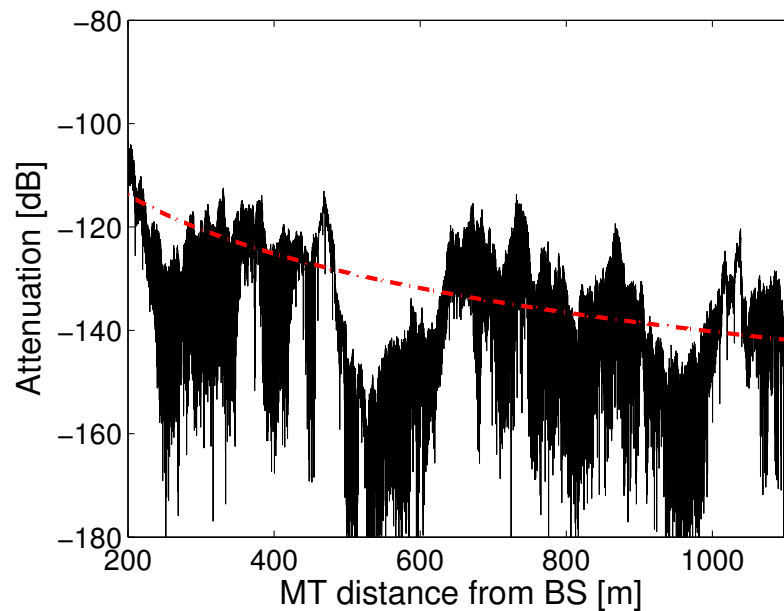


Figure 5.16: Path loss of the LUM scenario. The red, dash-dotted line shows the path loss as given by the COST Walfish-Ikegami path loss model.

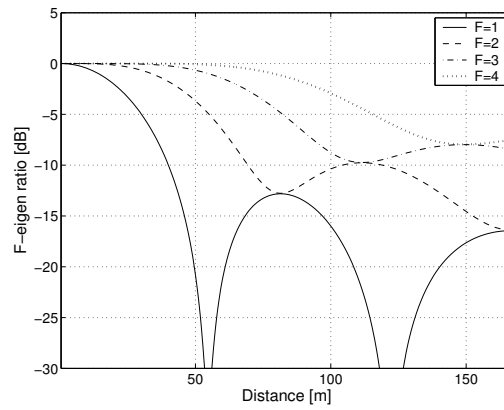


Figure 5.17: The F-eigen ratio for a single LOS path and $F = 1, 2, 3, 4$.

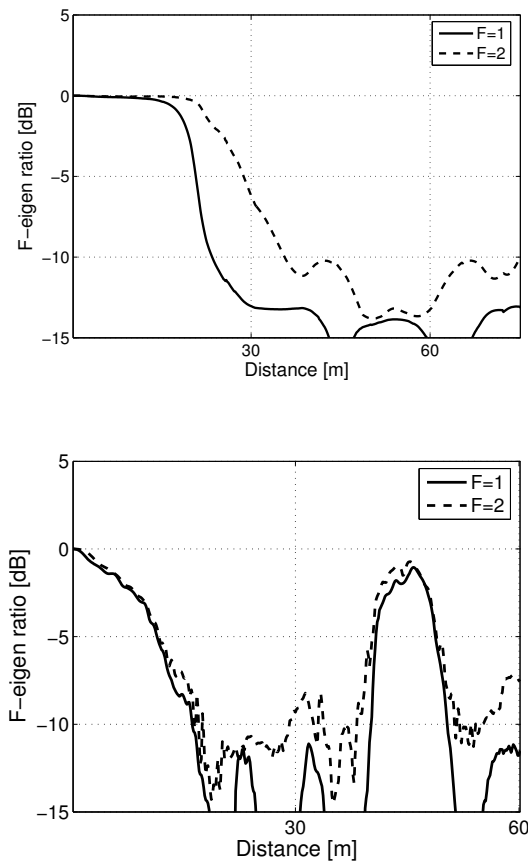
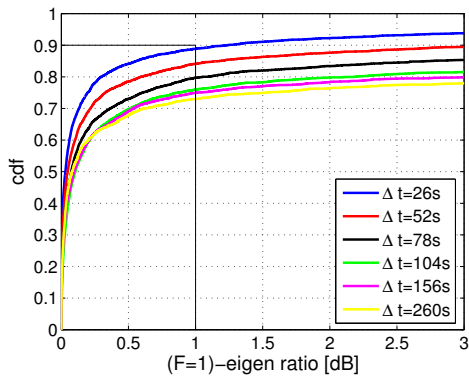
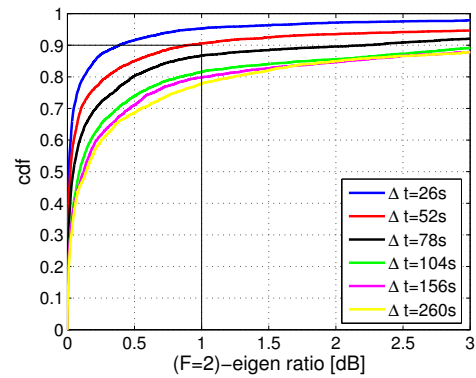


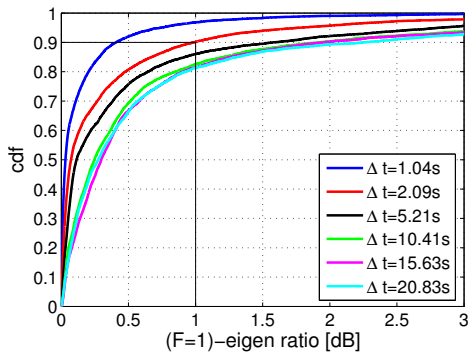
Figure 5.18: The F-eigen ratio for the LUM environment and $F = 1, 2$; two simulation runs of the same environment.



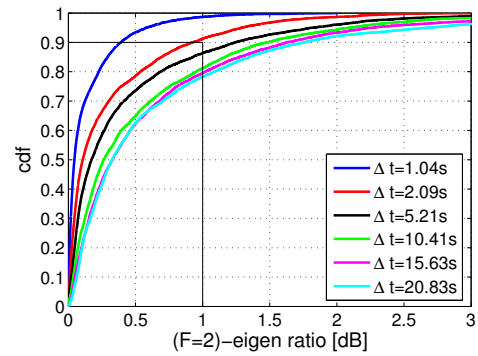
(a) LUM (F=1)-eigen ratio.



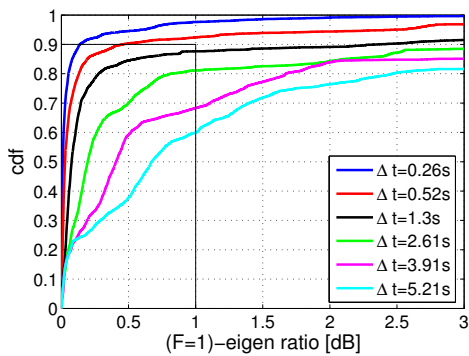
(b) LUM (F=2)-eigen ratio.



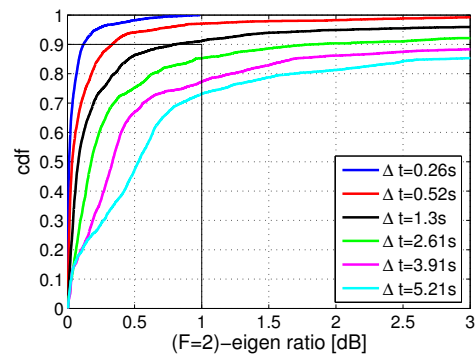
(c) PCH (F=1)-eigen ratio.



(d) PCH (F=2)-eigen ratio.



(e) POL (F=1)-eigen ratio.



(f) POL (F=2)-eigen ratio.

Figure 5.19: CDFs of the F-eigen ratio for the LUM, PCH, and POL environment and $F = 1, 2$.

5.9 Multi-User Detector

In the following I will show an application of my channel model. This work results from a collaboration with Thomas Zemen. We investigate the performance of an iterative MIMO multi-user receiver, implemented by Thomas Zemen [115], [116], in the uplink using my channel model. From my point of view this is the best validation of a channel model. My channel model was designed for receive algorithm studies. The following investigations even test some advanced features of my model like the multi-user capability as described in Section 4.12. One can find in literature many implementations of geometry based channel models but unfortunately nearly no references on receive algorithm performance tests using such models. Most people just use very simple channel models to validate their receive algorithms. Of course, using a geometry based model for performance evaluation is not that easy as ,e.g., using an AWGN channel. But the results of such tests using realistic models like my GSCM are much more valuable. In the following part I will describe the part of our work necessary to understand the results shown in Section 5.9.3.

5.9.1 Overview

Each MT uses one transmit antenna. Multi-carrier code division multiple access (MC-CDMA) based on orthogonal frequency division multiplexing (OFDM) is applied using a random spreading sequence in the frequency domain. The base station employs more than one antenna. The receiver has no knowledge about the detailed autocorrelation and power delay profile of the channel, only a maximum velocity of the MT and a maximum length of the impulse response is assumed. We compare the performance of the MIMO multi-user receiver for two different channel models:

- The first is a stochastic Rayleigh fading channel model, using a chip spaced delay tap line with i.i.d. taps and an exponentially decaying power delay profile. The channel is time-variant. Each tap has an autocorrelation according to the Jakes model [117]. The antennas at the BS are assumed to be uncorrelated [116].
- The second model is my implementation of the GSCM based on the COST 259 GTU environment.

We apply OFDM in order to transform the time-variant frequency-selective channel into a set of parallel time-variant frequency-flat channels, the so-called subcarriers. We consider time-variant channels which may vary significantly over the duration

of a long block of OFDM symbols. However, for the duration of each single OFDM symbol, the channel variation is assumed small enough to be neglected. This implies a very small inter-carrier interference (ICI) [118, 116]. Each OFDM symbol is preceded by a cyclic prefix to avoid inter-symbol interference (ISI).

The discrete-time sequence of channel coefficients for each frequency-flat subcarrier is bandlimited by the normalized Doppler bandwidth

$$B_D = \nu_{\max} T_S, \quad (5.4)$$

where $\nu_{\max} = \frac{v_{\max} f_C}{c_0}$ is the maximum Doppler frequency, v_{\max} is the maximum velocity, T_S is the symbol duration, and c_0 denotes the speed of light.

It was shown by Slepian [119] that time-limited parts of band-limited sequences span a low-dimensional subspace. A natural set of basis functions for this subspace is given by the so-called discrete prolate spheroidal sequences. A Slepian basis expansion using this subspace representation was proposed in [120] for time-variant channel equalization. It was shown in [121] that the channel estimation bias obtained with the Slepian basis expansion is more than a magnitude smaller than the Fourier basis expansion (i.e. a truncated discrete Fourier transform) [122].

We apply the iterative time-variant channel estimation scheme developed in [123, 124] to the MIMO case [116] and extend it to multi-path channels with non chip-spaced path delays.

The system operates at a carrier frequency $f_C = 2$ GHz and the $K = 32$ users move with a velocity $v_{\text{MT}} = 70$ km/h. This gives a maximum Doppler frequency of $\nu_{\max} = 133$ Hz corresponding to $B_D = 0.0027$. The number of subcarriers is $N = 64$ and the length of the OFDM symbol with cyclic prefix is $P = G + N = 79$. The data block consists of $M = 256$ OFDM symbols with $J = 60$ OFDM pilot symbols. The system is designed for a maximum velocity $v_{\max} = 100$ km/h which results in $D = 3$ for the Slepian basis expansion [125]. The BS uses $n_R = 2$ receive antennas. All simulation results are averaged over 100 independently generated data blocks. We assume a maximum path delay of $L_{\max} = 10$ symbols.

5.9.2 Simulation Environment

Description of the Stochastic Channel Model

Realizations of the time-variant frequency-selective MIMO channel $h_{k,q}[n, \ell]$ are generated using an exponentially decaying power-delay profile (PDP) $\eta^2[\ell] =$

Parameter	Value
Cell size	1000 m
No. of BS	1
No. of BS antennas	{1, 2}
No. of MT	{1, 32}
No. of MT antennas	1
Antenna pattern	omni-directional
No. of IOs	20 per cluster
Chip rate	$3.84 \cdot 10^6$
Oversampling	4 times

Table 5.4: Simulation parameters for the GSCM.

$e^{-\ell} / \sum_{\ell'=0}^{L-1} e^{-\ell'}$, $\ell = 0, \dots, L-1$, [6] with a length of $L = 15$. The time indices n and ℓ correspond to the sampling at rate $1/T_C$. The PDP corresponds to a root mean square delay spread $T_D = T_C = 260$ ns for a chip rate of $T_C = 3.84 \cdot 10^6$ 1/s. The autocorrelation for every channel tap is given by $R_{hh}[n, \ell] = \eta^2[\ell] J_0(2\pi\nu_D P n)$ which results in the classical Jakes' spectrum [117]. We simulate the time-variant channel using the model in [126] corrected for low velocities in [127].

Simulations using the GSCM

We have chosen the COST 259 GTU macro cell environment for all simulations using the GSCM. The simulation parameters are summarized in Table 5.4. At the transmitter and the receiver a root raised cosine filter is used for pulse-shaping. Both filters are applied to the four times over sampled transmit signal. After the receive filter the sample rate is reduced to the chip rate. The receiver performs processing at chip rate. All MTs are uniformly spread within the cell area. Note that there is a minimum distance between the BS and the MT of 100m due to the definition of the scenario.

Power Control and Fading Effects The COST 259 channel model includes large-scale and small-scale effects. For the focus of our investigations the large-scale effects are not taken into account since we assume perfect power control for slow changes of the channel. Thus only small-scale effects are visible to the receiver. Figure 5.20 shows the receive power levels for 16 users over one time slot and a MT speed of 70km/h. The power is normalized to a total receive power of unity (0 dB) on average

per user. With these settings the large-scale fading is kept outside the simulation.

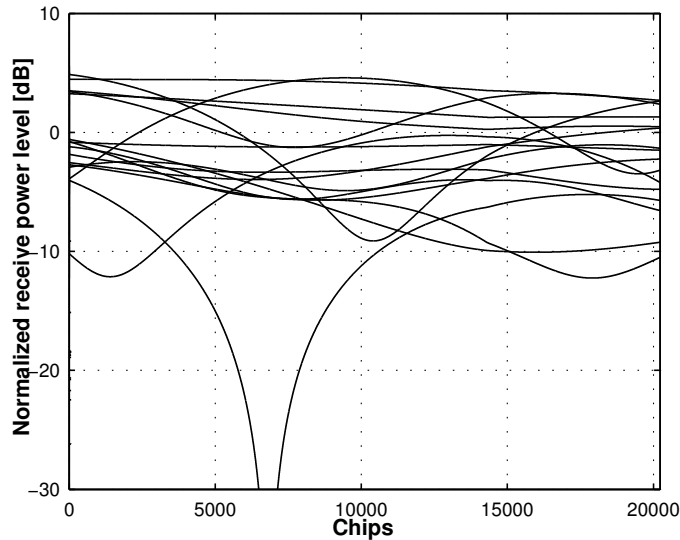


Figure 5.20: Normalized receive power of 16 users (from [125]).

Focusing on the variation of the receive power of the various users the differences look quite big. But this is mainly due to the short observation period. All MTs move over a distance of slightly more than one wavelength within one OFDM.

Synchronization We assume that all impinging user signals are received at the same time (synchronization mode 3⁶). This is achieved by subtracting the smallest delay from all MPCs of a user. This is no loss of generality but makes simulations much easier because the receive algorithm does not need additional synchronization measures.

Late Arrivals In my channel model the length of the impulse response is only given by the geometry of the simulated environment. Late arriving components, especially from far clusters, may occur. In an OFDM system the cyclic prefix length determines the maximum path delay that does not lead to performance degradation. To visualize this effect some simulations were performed with and without late arrivals

⁶More information on the synchronization modes can be found in Section 4.1.3.

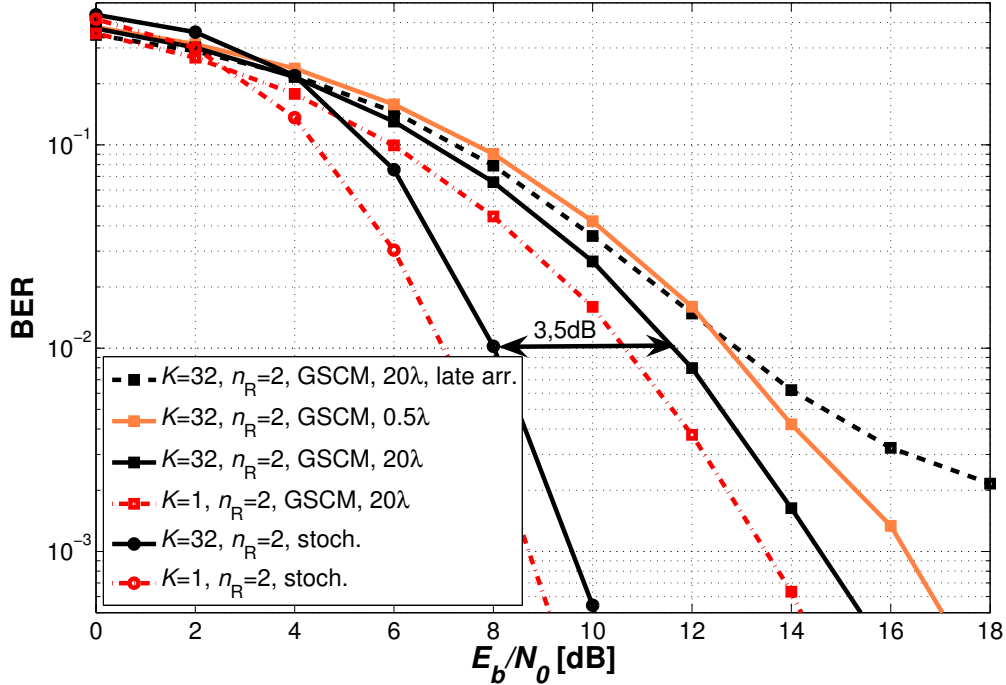


Figure 5.21: BER versus SNR on the uplink for the multi-user MIMO-OFDM receiver after 4 iterations. $K = 32$ users are moving at $v_{MT} = 70$ km/h and the receiver employs $n_R = 2$ antennas (from [125]).

(see Section 5.9.3). For the second case all late arriving components were set to zero. The total receive power was kept the same for both cases.

5.9.3 Results

In Figure 5.21, we illustrate the multiuser MIMO-OFDM uplink performance with iterative time-variant channel estimation based on the Slepian basis expansion in terms of bit error rate (BER) versus E_b/N_0 after 4 iterations. The effect using either the stochastic or the geometric channel model is compared.

The diversity order is nearly the same. The too optimistic assumptions like the regularly-spaced tap delay structure and the very large delay spread of the stochastic model result in better performance. All curves for the stochastic model are shifted by about 3.5 dB to the left compared to the GSCM with a receive antenna spacing of

20λ . For 32 users a performance loss of slightly less than 1 dB occurs compared to the single user case.

If the length of the impulse response exceeds the length of the cyclic prefix some ISI remains. This effect becomes visible for very high E_b/N_0 values. In contrast to the other simulations, which all have the same diversity at high E_b/N_0 , the late arrivals result indicates an error floor.

The simulation results show that an iterative receiver using the Slepian basis expansion in two dimensions for channel equalization is able to deal with delay tap line models and the more realistic GSCM. Implementations of receive algorithms [120] are often bound to regularly-spaced tap delay channel models and would fail in the presence of models having arbitrary delayed MPCs since the energy of one MPC is spread over several taps. This spreading of energy has to be taken into account by the channel estimator.

Our results demonstrate that multi-path and space diversity, which are predicted by the more realistic GSCM, are smaller than for tapped delay line models with Rayleigh fading on the individual MPCs.

Chapter 6

Conclusions and Outlook

This thesis deals with the characterization and modelling of the wireless MIMO channel. The thesis has three main parts. The first part, Chapter 3, deals with my measurements and the analysis of the MIMO channel. The next part in Chapter 4 addresses the MIMO channel model I have designed and implemented. In Chapter 5, the last part of my Thesis, I validate several aspects of my channel model.

Channel Measurements

In the following I list the key findings and conclusions about my channel measurements and evaluations.

- I address the problem of the estimation of mutual information based on channel sounder measurements and show the influence of measurement noise on the results.
- For the calculation of the mutual information the channel transfer matrix has to be normalized. I discuss the two useful normalization approaches, namely constant receive power and constant transmit power. Based on measurement results I illustrate the benefits and drawbacks of both of them.
- The evaluation of the measurements show that for constant receive power the LOS channel has lower mutual information than the NLOS channel. But if the smaller pathloss of the LOS channel than of the NLOS channel is taken into account the LOS case outperforms the NLOS channel in terms of mutual information. From a system point of view the LOS channel is better than the NLOS case due to the lower transmitter power necessary for obtaining the same channel throughput. The same conclusion is also drawn in [86].

Channel Modelling

In the following I present the key findings and conclusions about my channel model.

- A clear modular structure with well defined interfaces eases the adaptation of the model for new tasks and gives the possibility of adding additional functionality without changing the rest of the model. Some modules of my model like the Convolution Module or the Antenna Module are valid for any GSCM specification. Implementing new geometry based channel models only requires the reprogramming of the Propagation Module. All the other modules can be reused.
- I have introduced the twin cluster concept as a new approach of modelling the wireless MIMO channel using GSCMs. The big advantage of the twin cluster concept in comparison to the traditional single-interaction clusters and the local clusters is their ability of having angle of arrival, angle of departure and delay statistics independent of each other.
- At the moment standardized channel models use the twin cluster approach only for part of the modelling concept. I am confident that it is possible to generate realistic scenarios with the usage of twin clusters as the only propagation component. The twin cluster concept is based on the evaluation of measurements and this evaluation does not distinguish between different types of clusters. Especially for the long term statistics the twin cluster concept shows a big advantage versus other concepts dealing in the angular delay domain.
- My modelling concept is able to deal with any MIMO environment and any types of antenna arrays. However, realistic parameter sets for all those environments are required which is currently a bottleneck for my model. At the moment a lot of effort is put on the exploitation of the wireless MIMO channel [23]. Therefore I am confident that realistic parameter sets, obtained from measurement data, will be available within the near future.
- A realistic channel model always tends to be complex and requires a lot of input parameters. This is somehow also true for my model. Therefore I have put a Matlab implementation of the core part of my model on the internet. The model can be found at <http://www.ftw.at/cost273>. This implementation shall help people understanding my model in all detail and help to increase the usage of more realistic channel models. State of the art MIMO communication systems require realistic channel models for any performance investigations.

Channel Model Validation

In the following I give an overview on the key findings and conclusions of the validation of my channel model.

- The proposed channel model is able to deal with the wireless MIMO channel in a very realistic manner. It reflects small-scale and large-scale variations of the channel as well as polarization effects, the Doppler spread and antenna correlations. The validation of my channel model shows considerable conformance with measurement results. I want to stress that it is not possible to perform the whole validation, as I have done in Chapter 5 with a single simulation run. Different features of the channel model demand for different parameter settings of the model. With today's computers it is not possible to simulate, e.g., an 8×8 MIMO channel for UMTS and a MT movement of several hundred meters within realistic time scales. In addition the required memory for storing all the output data of the model would be tremendous. The specification of my model includes a lot of stochastic distribution functions which require Monte-Carlo simulations to validate the specific parameters.
- I also show results of the application of my model to a receive algorithm. This practical application of the model validates its usefulness and practicality. It is demonstrated that simple tap-delay line models pretend a better performance of a receive algorithm than it would have in real life. So, receive algorithm design can profit a lot from the usage of realistic channel models at an early development step.

Appendix A

Model Parameter Sets

In the following I list all the parameters of my model including the corresponding values for the three simulation environments I have used throughout my thesis. As in COST 259 and COST 273 I divide the parameters into external parameters and stochastic parameters. External parameters are parameters that remain fixed for a simulation run whereas the stochastic parameters describe the different radio environments. For my thesis I have used the following three environments and corresponding parameter sets:

- Large urban macrocell (LUM) in Table A.1 and A.4,
- Picocell Halls (PCH) in Table A.2 and A.5,
- Picocell Office LOS (POL) in Table A.3 and A.6,

Parameter	Value	Comments, incl. ref.
f_c [Hz]	2	2 GHz is typical because of UMTS
h_{BS} [m]	50	from COST 259
h_{MT} [m]	1.5	pedestrian walking
\vec{r}_{BS} [m]	(0,0, h_{BS})	origin of coordinate system
\vec{r}_{MT} [m]	uniformly distributed in cell area	
Cell radius [m]	1000	from COST 273
Pathloss Model:	COST 231 Walfish-Ikegami	[62]
$h_{rooftop}$ [m]	15	from COST 259 (GBU)
w_{road} [m]	25	from COST 259 (GBU)
w_b [m]	50	from COST 259 (GBU)
θ_{road} [°]	45	from COST 259 (GBU)

Table A.1: External parameters for the LUM environment.

Parameter	Value	Comments, incl. ref.
f_c [Hz]	2	2 GHz is typical because of UMTS
h_{BS} [m]	5	
h_{MT} [m]	1.5	pedestrian walking
\vec{r}_{BS} [m]	(0,0, h_{BS})	origin of coordinate system
\vec{r}_{MT} [m]	uniformly distributed in cell area	
Cell radius [m]	30	from COST 273
Pathloss Model:	COST 273	TD(02)055
A_{room} [m x m]	15	from COST 273
N_{floor} [m]	10	from COST 273
Opposite building [y/n]	y	from COST 273

Table A.2: External parameters for the PCH environment.

Parameter	Value	Comments, incl. ref.
f_c [Hz]	2	2 GHz is typical because of UMTS
h_{BS} [m]	2	
h_{MT} [m]	1	PDA
\vec{r}_{BS} [m]	$(0,0,h_{BS})$	origin of coordinate system
\vec{r}_{MT} [m]	uniformly distributed in cell area	
Cell radius [m]	5	from COST 273
Pathloss Model:	COST 273	TD(02)055
A_{room} [m x m]	5	from COST 273
N_{floor} [m]	4	from COST 273
Opposite building [y/n]	n	from COST 273

Table A.3: External parameters for the POL environment.

Parameter	Value	Comments, inc. ref.
LOS visibility region		
R_C [m]	30	from COST 259
L_C [m]	20	from COST 259
d_{co} [m]	500	from COST 259
Cluster visibility regions		
R_C [m]	100	from COST 259
L_C [m]	20	from COST 259
Average number of clusters N_C	2.18	from COST 259 (GBU)
Number of local clusters $N_{C,local}$	1	around the MT
Cluster selection parameter K_{sel}	1	from COST 273
Number of MPCs per cluster N_{MPC}	20	from [108]
Cluster power		
k_τ [dB/ μ s]	1	from COST 273
τ_B [μ s]	10	from COST 273
μ_K [dB]/ σ_K [dB]	((26-EPL)/6) / 6	from COST 259
Inter cluster delay		
$f(\tau_C)$ [μ s]	$\mathcal{U}[0/3]$	
Inter cluster angular spread at BS		
$f(\Phi_{BS})$ [$^\circ$]	$\mathcal{U}[0, 360[$	
$f(\Theta_{BS})$ [$^\circ$]	$\mathcal{U}[-10, 0]$	
Inter cluster angular spread at MT		
$f(\Phi_{MT})$ [$^\circ$]	$\mathcal{U}[0, 360[$	
$f(\Theta_{MT})$ [$^\circ$]	$\mathcal{U}[0, 45]$	
Intra cluster delay spread		
$f(\tau) = \mathcal{N}_{log}(\mu_\tau[\mu\text{s}]/\sigma_\tau[\text{dB}])$	0.4/3	from COST 273
Intra cluster angular spread at BS		
$f(\Phi_{BS}) = \mathcal{N}_{log}(\mu_{\varphi_{BS}}[^\circ]/\sigma_{\varphi_{BS}}[\text{dB}])$	0.81/0.34	from 3GPP
$f(\Theta_{BS}) = \mathcal{N}_{log}(\mu_{\vartheta_{BS}}[^\circ]/\sigma_{\vartheta_{BS}}[\text{dB}])$	0.5/3	from COST 259
Intra cluster angular spread at MT		
$f(\Phi_{BS}) = \mathcal{N}_{log}(\mu_{\varphi_{MT}}[^\circ]/\sigma_{\varphi_{MT}}[\text{dB}])$	35/0	from 3GPP
$f(\Theta_{BS}) = \mathcal{N}_{log}(\mu_{\vartheta_{MT}}[^\circ]/\sigma_{\vartheta_{MT}}[\text{dB}])$	10/3	
Shadow fading σ_{SF} [dB]	6	from COST 273
Autocorrelation distance d_{corr} [m]	100	from COST 259
Cross correlations ρ		from COST 273
$\rho_{\tau, \varphi_{BS}}$	0.5	
$\rho_{\tau, \varphi_{MT}}$	0	Unknown correlation
$\rho_{\tau, SF}$	-0.6	values are set
$\rho_{\varphi_{BS}, \varphi_{MT}}$	0	to zero
$\rho_{\varphi_{BS}, SF}$	-0.6	
$\rho_{\varphi_{MT}, SF}$	0	
Polarization		
μ_{XPD}/σ_{XPD} [dB]	6/2	from COST 273
μ_{VVHH}/σ_{VVHH} [dB]	0/ $-\infty$	from COST 273
μ_{VHHV}/σ_{VHHV} [dB]	0/ $-\infty$	from COST 273

Table A.4: Stochastic parameters for the LUM environment.

Parameter	Value	Comments, inc. ref.
LOS visibility region		
R_C [m]	3	
L_C [m]	1	
d_{co} [m]	30	
Cluster visibility regions		
R_C [m]	5	
L_C [m]	1	
Average number of clusters N_C	4	from COST 273
Number of local clusters $N_{C,local}$	1	around the MT
Cluster selection parameter K_{sel}	0	from COST 273
Number of MPCs per cluster N_{MPC}	20	from COST 273
Cluster power		
k_τ [dB/ μ s]	50	from COST 273
τ_B [μ s]	0.5	
μ_K [dB]/ σ_K [dB]	1/3	
Inter cluster delay		
$f(\tau_C)$ [μ s]	$\mathcal{U}[0/0.5]$	
Inter cluster angular spread at BS		
$f(\Phi_{BS})$ [$^\circ$]	$\mathcal{U}[0, 360[$	
$f(\Theta_{BS})$ [$^\circ$]	$\mathcal{U}[-60, 60]$	
Inter cluster angular spread at MT		
$f(\Phi_{MT})$ [$^\circ$]	$\mathcal{U}[0, 360[$	
$f(\Theta_{MT})$ [$^\circ$]	$\mathcal{U}[-60, 60]$	
Intra cluster delay spread		
$f(\tau) = \mathcal{N}_{log}(\mu_\tau[\mu\text{s}]/\sigma_\tau[\text{dB}])$	0.1/3	
Intra cluster angular spread at BS		
$f(\Phi_{BS}) = \mathcal{N}_{log}(\mu_{\varphi_{BS}}[^\circ]/\sigma_{\varphi_{BS}}[\text{dB}])$	10/3	
$f(\Theta_{BS}) = \mathcal{N}_{log}(\mu_{\vartheta_{BS}}[^\circ]/\sigma_{\vartheta_{BS}}[\text{dB}])$	5/3	
Intra cluster angular spread at MT		
$f(\Phi_{BS}) = \mathcal{N}_{log}(\mu_{\varphi_{MT}}[^\circ]/\sigma_{\varphi_{MT}}[\text{dB}])$	45/3	
$f(\Theta_{BS}) = \mathcal{N}_{log}(\mu_{\vartheta_{MT}}[^\circ]/\sigma_{\vartheta_{MT}}[\text{dB}])$	7/3	
Shadow fading σ_{SF} [dB]	3	from COST 273
Autocorrelation distance d_{corr} [m]	5	
Cross correlations ρ		
$\rho_{\tau, \varphi_{BS}}$	0	no known correlation values for this environment
$\rho_{\tau, \varphi_{MT}}$	0	
$\rho_{\tau, SF}$	0	
$\rho_{\varphi_{BS}, \varphi_{MT}}$	0	
$\rho_{\varphi_{BS}, SF}$	0	
$\rho_{\varphi_{MT}, SF}$	0	
Polarization		
μ_{XPD}/σ_{XPD} [dB]	9/2	from COST 273
μ_{VVHH}/σ_{VVHH} [dB]	$0/-\infty$	from COST 273
μ_{VHHV}/σ_{VHHV} [dB]	$0/-\infty$	from COST 273

Table A.5: Stochastic parameters for the PCH environment.

Parameter	Value	Comments, inc. ref.
LOS visibility region		
R_C [m]	3	
L_C [m]	1	
d_{co} [m]	30	
Cluster visibility regions		
R_C [m]	5	
L_C [m]	1	
Average number of clusters N_C	6	
Number of local clusters $N_{C,local}$	2	around the MT and BS
Cluster selection parameter K_{sel}	0	from COST 273
Number of MPCs per cluster N_{MPC}	20	from COST 273
Cluster power		
k_τ [dB/ μ s]	50	from COST 273
τ_B [μ s]	0.5	
μ_K [dB]/ σ_K [dB]	5/1	
Inter cluster delay		
$f(\tau_C)$ [μ s]	$\mathcal{U}[0/0.2]$	
Inter cluster angular spread at BS		
$f(\Phi_{BS})$ [$^\circ$]	$\mathcal{U}[0, 360[$	
$f(\Theta_{BS})$ [$^\circ$]	$\mathcal{U}[-60, 60]$	
Inter cluster angular spread at MT		
$f(\Phi_{MT})$ [$^\circ$]	$\mathcal{U}[0, 360[$	
$f(\Theta_{MT})$ [$^\circ$]	$\mathcal{U}[-60, 60]$	
Intra cluster delay spread		
$f(\tau) = \mathcal{N}_{log}(\mu_\tau[\mu\text{s}]/\sigma_\tau[\text{dB}])$	0.05/3	
Intra cluster angular spread at BS		
$f(\Phi_{BS}) = \mathcal{N}_{log}(\mu_{\varphi_{BS}}[^\circ]/\sigma_{\varphi_{BS}}[\text{dB}])$	10/3	
$f(\Theta_{BS}) = \mathcal{N}_{log}(\mu_{\vartheta_{BS}}[^\circ]/\sigma_{\vartheta_{BS}}[\text{dB}])$	5/3	
Intra cluster angular spread at MT		
$f(\Phi_{BS}) = \mathcal{N}_{log}(\mu_{\varphi_{MT}}[^\circ]/\sigma_{\varphi_{MT}}[\text{dB}])$	45/3	
$f(\Theta_{BS}) = \mathcal{N}_{log}(\mu_{\vartheta_{MT}}[^\circ]/\sigma_{\vartheta_{MT}}[\text{dB}])$	7/3	
Shadow fading σ_{SF} [dB]	3	from COST 273
Autocorrelation distance d_{corr} [m]	1	
Cross correlations ρ		
$\rho_{\tau, \varphi_{BS}}$	0	no known correlation values for this environment
$\rho_{\tau, \varphi_{MT}}$	0	
$\rho_{\tau, SF}$	0	
$\rho_{\varphi_{BS}, \varphi_{MT}}$	0	
$\rho_{\varphi_{BS}, SF}$	0	
$\rho_{\varphi_{MT}, SF}$	0	
Polarization		
μ_{XPD}/σ_{XPD} [dB]	9/2	from COST 273
μ_{VVHH}/σ_{VVHH} [dB]	$0/-\infty$	from COST 273
μ_{VHHV}/σ_{VHHV} [dB]	$0/-\infty$	from COST 273

Table A.6: Stochastic parameters for the POL environment.

Appendix B

List of Abbreviations

I list all the abbreviations used in my thesis in Table B.1, Table B.2, and Table B.3.

Abbreviation	Description
3GPP	Thirds Generation Partnership Project
ADPS	Angular Delay Power Spectra
AWGN	Additive White Gaussian Noise
BS	Base Station
CCDF	Complementary Cumulative Distribution Function
CDF	Cumulative Distribution Function
COST	European Co-operation in the field of Scientific and Technical Research
CRP	Constant Receive Power
CTP	Constant Transmit Power
DDIR	Double Directional Impulse Response
DOA	Direction of Arrival
DOD	Direction of Departure
ESPRIT	Estimation of Signal Parameters via Rotational Invariance Techniques

Table B.1: Abbreviations and their full description (A–F).

Abbreviation	Description
GBU	General Bad Urban
GCL	General Corridor LOS
GCN	General Corridor NLOS
GFH	General Factory/Hall
GHT	General Hilly Terrain
GOL	General Office LOS
GON	General Office NLOS
GOP	General Open Place
GSCM	Geometry-based Stochastic Channel Model
GSM	Global System for Mobile Communications
GRA	General Rural Area
GSL	General Street LOS
GSN	General Street NLOS
GSX	General Street Crossing
GTU	General Typical Urban
HPW	Homogeneous Plane Wave
ICI	Inter-Carrier Interference
IO	Interacting Object
ISI	Inter-Symbol Interference
LOS	Line of Sight
LRS	Local Region of Stationarity
LS	Large-Scale
LUM	Large Urban Macrocell
MC-OFDM	Multi-Carrier OFDM
MCC	Microcell City Center
MIMO	Multiple Input Multiple Output
MPC	Multi-path Component
MT	Mobile Terminal

Table B.2: Abbreviations and their full description (G–M).

Abbreviation	Description
NLOS	No LOS
OFDM	Orthogonal Frequency Division Multiplex
OIU	Outdoor-to-Indoor Urban Macrocell
OSF	Oversampling Factor
PCH	Pico Cell Hall
PDF	Probability Density Function
PIN	Positive Intrinsic Negative
POL	Pico Cell Office LOS
PON	Pico Cell Office NLOS
RA	Rural Area
SAGE	Space-Alternating Generalized Expectation Maximization Algorithm
SCM	Spatial Channel Model
SF	Shadow Fading
SMC	Small Urban Macro Cell
SINR	Signal-to-Noise and Interference Ratio
SNR	Signal-to-Noise Ratio
SS	Small-Scale
TU	Typical Urban
ULA	Uniform Linear Array
UMTS	Universal Mobile Telecommunications System
UWB	Ultra Wide Band
VCDA	Virtual Cell Deployment Area
VSWR	Voltage Standing Wave Ratio
WSS	Wide Sense Stationarity
XPD	Cross Polarization Discrimination

Table B.3: Abbreviations and their full description(N–Z).

Appendix C

List of Symbols

I list the symbols that are generally used throughout my thesis. In Table C.1 all Greek symbols are shown, whereas Table C.2 lists all lower case symbols and in Table C.3 all upper case symbols are denoted. Locally used symbols are omitted.

Symbol	Description
Δ	incremental step
$\mathbf{\Gamma}$	correlation matrix
λ	wavelength
$\mathbf{\Lambda}$	diagonal matrix of eigenvalues
μ	mean value
ν	Doppler frequency
ϕ	angle in elevation
φ	angular spread in elevation
ρ	SNR
σ	standard deviation
τ_{coh}	coherence time
τ_{LT}	long-term time constant
τ	delay
θ	angle in azimuth
ϑ	angular spread in azimuth
$\mathbf{\Upsilon}$	Cholesky factorization matrix
$\mathbf{\Xi}$	polarization matrix of attenuation coefficients
Ω	antenna pattern

Table C.1: Greek symbols used throughout my thesis.

Symbol	Description
a	attenuation coefficient
c_0	speed of light
d	distance
f	frequency
h	single antenna impulse response
h_F	filtered impulse response
h_{Rx}	receive filter
h_{Tx}	transmit filter
k_{OSF}	oversampling factor
n	noise
n_T	number of transmit antennas
n_R	number of receive antennas
$q_{\text{eigen}}^{(F)}$	F-eigen ratio of the F largest eigenvalues
r	radius
\vec{r}	distance vector
t	time
u	input signal after transmit filter
v	receive signal before receive filter
v_{MT}	speed of the MT
x	input signal
y	output signal

Table C.2: Lower case symbols used throughout my thesis.

Symbol	Description
A	attenuation coefficient
B	bandwidth
C	mutual information
\mathbf{C}	coupling matrix
Cl	number of clusters
E_b	signal energy
\mathbf{h}	channel impulse response matrix
J	Jacobi determinant
K	number of snapshots
K_{LOS}	LOS power factor
K_{sel}	cluster selection parameter
L	size of transition region
N_0	noise energy
Q_{WSS}	WSS quality
R	size/radius of a region
\mathbf{R}	covariance matrix
P	power level
S	total number of paths
S_{MPC}	number of MPCs per cluster
\mathbf{T}	rotation matrix
T_S	sample rate
\mathbf{W}	column matrix of eigenvectors of a matrix

Table C.3: Upper case symbols used throughout my thesis.

Bibliography

- [1] J. Winters, “On the Capacity of Radio Communications Systems with Diversity in Rayleigh Fading Environments,” *IEEE Journal on Selected Areas Communications*, vol. 5, pp. 871–878, June 1987.
- [2] G. J. Foschini and M. J. Gans, “On Limits of Wireless Communications in a Fading Environment when Using Multiple Antennas,” *Wireless Personal Communications*, vol. 6, no. 3, pp. 311–335, 1998.
- [3] I. P802.11n/D1.0, “Draft Amendment to Wireless LAN Media Access Control (MAC) and Physical Layer (PHY) Specifications: Enhancements for Higher Throughput,” tech. rep., IEEE, March 2006.
- [4] M. Steinbauer, *The Radio Propagation Channel – A Non-Directional, Directional, and Double-Directional Point-of-View*. Thesis, Vienna University of Technology, Vienna, Austria, November 2001.
- [5] M. Toeltsch, J. Laurila, K. Kalliola, A. Molisch, P. Vainikainen, and E. Bonek, “Statistical characterization of urban spatial radio channels,” *IEEE Journal on Selected Areas Communications*, pp. 539–549, April 2002.
- [6] L. Correia, ed., *Wireless Flexible Personalised Communications*. John Wiley & Sons, Ltd., 2001.
- [7] K. Haneda and J. Takada, “High-resolution estimation of NLOS indoor MIMO channel with network analyzer based system,” in *Proceedings of the 14th IEEE International Symposium on Personal, Indoor and Mobile Radio Communications (PIMRC)*, vol. 1, pp. 675–679, September 2003.
- [8] R. Thomä, D. Hampicke, A. Richter, G. Sommerkorn, and U. Trautwein, “MIMO vector channel sounder measurement for smart antenna system evaluation,” *European Transactions on Telecommunications*, September 2001.

- [9] L. Hentilä, P. Kyösti, J. Ylitalo, X. Zhao, J. Meinilä, and J.-P. Nuutinen, “Experimental Characterization of Multi-Dimensional Parameters at 2.45 and 5.25 GHz Indoor Channels,” in *Proceedings of the International Symposium on Wireless Personal Multimedia Communications (WPMC)*, (Aalborg, Denmark), September 2005. see also <http://www.propsim.com/>.
- [10] D. Hampicke, M. Landmann, C. Schneider, G. Sommerkorn, R. Thomä, T. Fügen, J. Maurer, and W. Wiesbeck, “MIMO capacities for different antenna array structures based on double directional wide-band channel measurements,” in *Proceedings of the 56th IEEE Vehicular Technology Conference (VTC) Fall*, vol. 1, (Vancouver, Canada), pp. 180–184, September 2002.
- [11] P. Lehne, H. Hofstetter, and M. Debbah, “Eigenvalue distributions and capacity evaluations from outdoor MIMO measurements at 2.1GHz,” in *Proceedings of the IST Mobile and Wireless Communications Summit 2003*, (Aveiro, Portugal), June 2003.
- [12] M. Herdin, *Non-Stationary Indoor MIMO Radio Channels*. Thesis, Vienna University of Technology, Vienna, Austria, 2004.
- [13] H. Hofstetter, I. Viering, and W. Utschick, “Evaluation of Suburban Measurements by Eigenvalue Statistics,” in *Proceedings of the COST 273 Workshop*, (Espoo, Finland), May 2002.
- [14] I. Viering, H. Hofstetter, and W. Utschick, “Validity of Spatial Covariance Matrices over Time and Frequency,” in *Proceedings of the IEEE Global Telecommunications Conference (GLOBECOM)*, (Taipeh, Taiwan), November 2002.
- [15] I. Viering, *Analysis of Second Order Statistics for Improved Channel Estimation in Wireless Communications*. PhD thesis, University of Ulm, Ulm, Germany, 2003.
- [16] J. Fessler and A. Hero, “Space-alternating generalized expectation maximization algorithm,” *IEEE Transactions on Signal Processing*, pp. 2664–2677, October 1994.
- [17] B. Fleury, M. Tschudin, R. Heddergott, D. Dahlhaus, and K. Pedersen, “Channel parameter estimation in mobile radio environments using the SAGE algorithm,” *IEEE Journal on Selected Areas Communications*, pp. 434–450, October 1999.

- [18] R. Roy and T. Kailath, "ESPRIT Estimation of signal parameters via rotational invariance techniques," *IEEE Transactions on Acoustics, Speech, Signal Processing*, pp. 984–995, July 1989.
- [19] M. Haardt and J. Nosske, "Unitary ESPRIT: How to obtain increased estimation accuracy with a reduced computational burden," *IEEE Transactions on Signal Processing*, pp. 1232–1242, May 1995.
- [20] H. Hofstetter, M. Steinbauer, and C. Mecklenbräuker, "Double-directional radio channel estimation at 2GHz for high speed vehicular mobiles - Experimental results," in *Proceedings of the International Symposium on Wireless Personal Multimedia Communications (WPMC)*, (Aalborg, Denmark), September 2001.
- [21] A. Richter, C. Schneider, M. Landmann, and R. Thoma, "Parameter Estimation Results of Specular and Dense Multi-path Components in Micro- and Macro-Cell Scenarios," in *Proceedings of the 61st International Symposium on Wireless Personal Multimedia Communications (WPMC)*, (Abano Terme, Italy), September 2004.
- [22] A. Richter and R. Thoma, "Joint maximum likelihood estimation of specular paths and distributed diffuse scattering," in *Proceedings of the 61st IEEE Vehicular Technology Conference (VTC) Spring*, vol. 1, (Baltimore, USA), pp. 11–15, May 2005.
- [23] N. Czink, P. Cera, J. Salo, E. Bonek, J.-P. Nuutinen, and J. Ylitalo, "A framework for automatic clustering of parametric MIMO channel data including path powers," in *Proceedings of the IEEE Vehicular Technology Conference (VTC) Fall*, (Montreal, Canada), September 2006.
- [24] A. F. Molisch, *Wireless Communications*. IEEE Press Wiley, 2005.
- [25] H. Özcelik, M. Herdin, W. Weichselberger, J. Wallace, and E. Bonek, "Deficiencies of 'Kronecker' MIMO radio channel model," *Electronics Letters*, pp. 1209–1210, August 2003.
- [26] W. Weichselberger, M. Herdin, H. Özcelik, and E. Bonek, "A stochastic MIMO channel model with joint correlation of both link ends," *IEEE Transactions Wireless Communications*, vol. 5, pp. 90–100, January 2006.

- [27] H. Özcelik, N. Czink, and E. Bonek, “What makes a good MIMO channel model?,” in *61st IEEE Vehicular Technology Conference (VTC) Spring*, pp. 156–160, May 2005.
- [28] A. Sayeed, “Deconstructing multiantenna fading channels,” *IEEE Transactions on Signal Processing*, pp. 2563–2579, October 2002.
- [29] A. Kanatas, I. Kountouris, G. Kostaras, and P. Constantinou, “UTD propagation model in urban microcellular environments,” *IEEE Transactions Vehicular Technology*, pp. 185–193, 1997.
- [30] G. Liang and H. Bertoni, “A new approach to 3-D ray tracing for propagation prediction in cities,” *IEEE Transactions on Antennas Propagation*, pp. 853–863, 1998.
- [31] S. Kim, B. G. Jr., T. Willis III, V. Erceg, S. Fortune, R. Valenzuela, L. Thomas, J. Ling, and J. Moore, “Radio propagation measurements and prediction using three dimensional ray tracing in urban environments at 908 MHz and 1.9 GHz,” *IEEE Transactions Vehicular Technology*, pp. 931–946, 1999.
- [32] G. Athanasiadou, A. Nix, and J. McGeehan, “A microcellular ray-tracing propagation model and evaluation of its narrow-band and wide-band predictions,” *IEEE Journal on Selected Areas Communications*, pp. 322–335, 2000.
- [33] G. Athanasiadou and A. Nix, “Investigation into the sensitivity of the power predictions of a microcellular ray-tracing propagation model,” *IEEE Transactions Vehicular Technology*, pp. 1140–1151, 2000.
- [34] C. Oestges, B. Clerckx, L. Raynaud, and D. Vanhoenacker-Janvier, “Deterministic channel modeling and performance simulation of microcellular wide-band communication systems,” *IEEE Transactions Vehicular Technology*, pp. 1422–1430, November 2002.
- [35] W. C. Y. Lee, “Effects on correlation between two mobile radio base-station antennas,” *IEEE Transactions on Communications*, vol. 21, pp. 1214–1224, 1973.
- [36] P. Petrus, J. H. Reed, and T. S. Rappaport, “Geometrical-based statistical macrocell channel model for mobile environments,” *IEEE Transactions on Communications*, vol. 50, pp. 495–502, 2002.

- [37] J. Blanz and P. Jung, "A flexibly configurable spatial model for mobile radio channels," *IEEE Transactions on Communications*, pp. 367–371, March 1998.
- [38] O. Norklit and J. B. Andersen, "Diffuse channel model and experimental results for array antennas in mobile environments," *IEEE Transactions on Antennas Propagation*, vol. 46, pp. 834–840, 1998.
- [39] J. Fuhl, A. Molisch, and E. Bonek, "Unified channel model for mobile radio systems with smart antennas," *IEE Proceedings Radar, Sonar and Navigation*, pp. 32–41, 1998.
- [40] M. Steinbauer and A. F. Molisch (eds.), *Directional channel models*. in L. Correia, *Flexible Personalized Wireless Communications*. J. Wiley, U.K., 2001.
- [41] A. Molisch, J. Laurila, and A. Kuchar, "Geometry-based stochastic model for mobile radio channels with directional component," in *Proceedings of the Symposium on Intelligent Antenna Technology for Mobile Communications*, (Guildford, UK), pp. 1–5, July 1998.
- [42] D. Gesbert, H. Bolcskei, D. Gore, and A. Paulraj, "Outdoor MIMO Wireless Channels: Models and Performance Prediction," *IEEE Transactions on Communications*, vol. 50, pp. 1926–1934, December 2002.
- [43] T. Svantesson, "A double-bounce channel model for multi-polarized MIMO systems," in *Proceedings of the 56th IEEE Vehicular Technology Conference (VTC)*, vol. 2, (Espoo, Finland), pp. 691–695, September 2002.
- [44] A. Molisch, "A generic model for MIMO wireless propagation channels in macro- and microcells," *IEEE Transactions on Signal Processing*, pp. 61–71, January 2004.
- [45] H. Hofstetter, I. Viering, and P. Lehne, "Spatial and temporal long term properties of typical urban base stations at different heights," *COST 273, TD(03)061*, 2003.
- [46] J. D. Parsons, *The Mobile Radio Propagation Channel*. Halstead Press, 1992.
- [47] R. Vaughan and J. B. Andersen, *Channels, Propagation and Antennas for Mobile Communications*. IEE Publishing, 2003.

- [48] A. Kwan, J. Dudley, and E. Lantz, “Who really discovered Snell’s law?,” *Physics World*, 2002.
- [49] D. Shiu, G. Foschini, M. Gans, and J. Kahn, “Fading correlation and its effect on the capacity of multielement antenna systems,” *IEEE Transactions on Communications*, vol. 48, pp. 502–513, 2000.
- [50] D. Chen-Nee Chuah; Kahn, J.M.; Tse, “Capacity of multi-antenna array systems in indoor wireless environment,” in *Proceedings of the IEEE Global Telecommunications Conference (GLOBECOM)*, vol. 4, pp. 1894–1899, November 1998.
- [51] M. Debbah and R. Müller, “MIMO channel modelling and the principle of maximum entropy,” *IEEE Transactions on Information Theory*, vol. 51, May 2005.
- [52] M. Debbah, R. Müller, H. Hofstetter, and P. Lehne, “Validation of Mutual Information Complying MIMO Channel Models,” *IEEE Transactions Wireless Communications*, p. submitted, 2005.
- [53] C. Oestges, D. Vanhoenacker-Janvier, and B. Clerckx, “Macrocellular directional channel modeling at 1.9 GHz: cluster parametrization and validation,” in *Proceedings of the IEEE Vehicular Technology Conference (VTC) Spring*, vol. 1, pp. 121–125, May 2005.
- [54] C.-C. Chong, C.-M. Tan, D. Laurenson, S. McLaughlin, M. Beach, and A. Nix, “A new statistical wideband spatio-temporal channel model for 5-GHz band WLAN systems,” *IEEE Journal on Selected Areas Communications*, pp. 139–150, February 2003.
- [55] N. Czink, E. Bonek, L. Hentilä, P. Kyösti, J. Nuutinen, and J. Ylitalo, “The interdependence of cluster parameters in MIMO channel modeling,” in *Proceedings of the European Conference on Antennas and Propagation (EuCap)*, (Nice, France), p. to be published, November 2006.
- [56] K. Li, M. Ingram, and A. V. Nguyen, “Impact of clustering in statistical indoor propagation models on link capacity,” *IEEE Transactions on Communications*, pp. 521–523, April 2002.

- [57] A. Molisch, A. Kuchar, J. Laurila, K. Hugl, and R. Schmalenberger, "Geometry-Based Directional Model for Mobile Channels - Principles and Implementation," *European Transactions on Telecommunications*, pp. 351–359, 2003.
- [58] H. Hofstetter, A. Molisch, and N. Czink, "A twin-cluster MIMO channel model," in *Proceedings of the European Conference on Antennas and Propagation (EuCap)*, (Nice, France), p. to be published, November 2006.
- [59] 3GPP, "Spatial channel model for MIMO simulations," tech. rep., Spatial Channel Model AHG (Combined ad-hoc from 3GPP & 3GPP2), September 2003.
- [60] L. Correia, ed., *Towards Mobile Broadband Multimedia Networks*. Elsevier Science Publishers B. V., 2006.
- [61] M. Failli, ed., *COST207 – Digital Land Mobile Radio Communications – Final Report*. Commission of the European Communities, 1989.
- [62] E. Damosso, ed., *COST 231: Evolution of Land Mobile Radio (Including Personal) Communications (Final Report) EUR 18957*. Published by European Commission, 1996.
- [63] M. Feuerstein, K. Blackard, T. Rappaport, S. Seidel, and H. Xia, "Path loss, delay spread, and outage models as functions of antenna height for microcellular system design," *IEEE Transactions Vehicular Technology*, vol. 43, pp. 487–498, August 1994.
- [64] H. Asplund, A. Molisch, M. Steinbauer, and N. Mehta, "Clustering of scatterers in mobile radio channels - Evaluation and modeling in the COST259 Directional Channel Model," in *Proceedings of the IEEE Vehicular Technology Conference (VTC)*, pp. 901–905, 2002.
- [65] A. Molisch, H. Asplund, R. Heddergott, M. Steinbauer, and T. Zwick, "The COST 259 Directional Channel Model I. Philosophy and general aspects," *IEEE Transactions Wireless Communications*, p. in press.
- [66] H. Asplund, A. Glazunov, A. Molisch, K. Pedersen, and M. Steinbauer, "The COST 259 Directional Channel Model II. Macrocells," *IEEE Transactions Wireless Communications*, p. in press.

- [67] J. Lempiainen and J. Laiho-Steffens, "The performance of polarization diversity schemes at a base station in small/micro cells at 1800 MHz," *IEEE Transactions Vehicular Technology*, vol. 47, pp. 1087–1092, August 1998.
- [68] K. Kalliola, H. Laitinen, L. Vaskelainen, and P. Vainikainen, "Directional 3D real-time dual-polarized measurement of wideband mobile radio channel," in *Proceedings of the 16th IEEE Instrumentation and Measurement Technology Conference (IMTC)*, vol. 1, pp. 170–175, May 1999.
- [69] S. Balling, M. Hein, M. Hennhöfer, G. Sommerkorn, R. Stephan, and R. Thomä, "Broadband Dual Polarized Antenna Arrays for Mobile Communication Applications," in *Proceedings of the 33rd European Microwave Conference (EMC)*, (Munich, Germany), October 2003.
- [70] G. Sommerkorn, D. Hampicke, R. Klukas, A. Richter, A. Schneider, and R. Thomä, "Uniform Rectangular Antenna Array Design and Calibration Issues for 2-D ESPRIT Application," in *Proceedings of the European Personal Mobile Communication Conference (EPMCC)*, (Vienna, Austria), February 2001.
- [71] J. Guterman, A. A. Moreira, and C. Peixeiro, "Two-element multi-band fractal PIFA for MIMO applications in small size terminals," in *Proceedings of the IEEE Antennas & Propagation Society Symposium*, (Monterey, CA), June 2004.
- [72] A. Pal, B. Lee, P. Rogers, G. Hilton, M. Beach, and A. Nix, "Effect of Antenna Element Properties and Array Orientation on Performance of MIMO Systems," in *Proceedings of the 1st Int. Symp. on Wireless Communication Systems*, pp. 120–124, September 2004.
- [73] B. Getu and J. Andersen, "The MIMO cube - a compact MIMO antenna," *IEEE Transactions Wireless Communications*, pp. 1136–1141, October 2005.
- [74] K. Pensel and J. Nosseck, "Uplink and Downlink Calibration of an Antenna Array in a Mobile Communication System," *COST 273, TD(97)058*, 1997.
- [75] P. Lehne and H. Hofstetter, "Documentation of the measurement campaign-part 1: 2.1 GHz, FLOWS deliverable no. D10(1)," tech. rep., IST project Flows, IST-2001-32125, April 2003.
- [76] *Walter Krenn, Hochfrequenztechnik GmbH. Am Kanal 27, 1112 Vienna, Austria.*, 2001.

- [77] D. Evans, L. Correia, H. Hofstetter, A. Burr, H. Rohling, G. Lehmann, R. Williams, and P. Lehne, "Flexible Convergence of Wireless Standards and Services. The IST FLOWS Project - An Overview," *E&I Journal*, 2003.
- [78] S. Skyttemyr, P. Hansen, and O. Alsos, "Broadband Cavity-backed Microstrip Antenna with Dual Linear Polarisation and Direct Microstrip Line Feeding," in *Proceedings of the AP2000 Millennium Conference on Antennas & Propagation*, (Davos, Switzerland), April 2000.
- [79] I. Telatar, "Capacity of multi-antenna gaussian channels," tech. rep., AT&T Technical Memorandum, June 1995.
- [80] P. Bello, "Characterization of Randomly Time-Variant Linear Channels," *IEEE Communication Letters*, pp. 360–393, 1963.
- [81] H. Bölcskei, D. Gesbert, C. Papadias, and A. van der Veen, *Space-Time Wireless Systems; From Array Processing to MIMO Communications*. Cambridge University Press, 2006.
- [82] A. Molisch, M. Steinbauer, M. Toeltsch, E. Bonek, and R. Thoma, "Capacity of MIMO systems based on measured wireless channels," *IEEE Journal on Selected Areas Communications*, vol. 20, pp. 561–569, April 2003.
- [83] R. Thomä, M. Landmann, G. Sommerkorn, and A. Richter, "Multidimensional high-resolution channel sounding in mobile radio," in *Proceedings of the 21st IEEE Instrumentation and Measurement Technology Conference (IMTC)*, vol. 1, pp. 257–262, May 2004.
- [84] P. Kyritsi, R. Valenzuela, and D. Cox, "Channel and capacity estimation errors," *IEEE Communication Letters*, vol. 6, pp. 517–519, December 2002.
- [85] P. Almers, F. Tufvesson, and A. Molisch, "Keyhole effect in MIMO wireless channels: measurement and theory," in *Proceedings of the IEEE Global Telecommunications Conference (GLOBECOM)*, vol. 4, pp. 1781–1785, November 2003.
- [86] M. Herdin, H. Özcelik, H. Hofstetter, and E. Bonek, "Variation of the Measured Indoor MIMO Capacity with Receive Direction and Position at 5.2GHz," *IEE Electronic Letters*, vol. 38, pp. 1283–1285, 2002.

- [87] L. Godara, "Application of Antenna Arrays to Mobile Communications, Part II: Beam-Forming and Direction-of-Arrival Considerations," in *Proceedings of the IEEE*, August 1997.
- [88] C. Brunner, W. Utschick, and J. Nossék, "Exploiting the short-term and long-term channel properties in space and time: eigenbeamforming concepts for the BS in WCDMA," *European Transactions on Telecommunications, Special Issue on Smart Antennas*, vol. 5, pp. 561–569, 2001.
- [89] J. Salz and J. Winters, "Effect of Fading Correlation on Adaptive Arrays in Digital Wireless Communications," in *Proceedings of the International Conference on Communications (ICC)*, (Geneva, Switzerland), pp. 1768–1774, 1993.
- [90] K. Hugl, J. Laurila, and E. Bonek, "Downlink beamforming for frequency division duplex systems," in *Proceedings of the IEEE Global Telecommunications Conference (GLOBECOM)*, vol. 4, pp. 2097–2101, May 1999.
- [91] TSG RAN WG4, "Deployment Aspects," Tech. Rep. 3G TR 25.493 V2.0.0, 3rd Generation Partnership Project (3GPP), 2000.
- [92] I. Viering, H. Hofstetter, and W. Utschick, "Spatial Long-Term Variations in Urban, Rural and Indoor Environments," *COST 273, TD(02)131*, 2002.
- [93] B. Fleury, "An uncertainty relation for WSS processes and its application to WSSUS systems," *IEEE Transactions on Communications*, vol. 44, pp. 1632–1634, December 1996.
- [94] A. Molisch and M. Steinbauer, "Condensed parameters for characterizing wide-band mobile radio channels," *International Journal of Wireless Information Networks (IJWIN)*, vol. 6, pp. 133–154, July 1999.
- [95] M. Shafi, M. Zhang, A. Moustakas, P. Smith, A. Molisch, F. Tufvesson, and S. Simon, "Polarized MIMO channels in 3-D: models, measurements and mutual information," *IEEE Journal on Selected Areas in Communications*, vol. 24, pp. 514–527, March 2006.
- [96] N. Czink and H. Hofstetter, "Proposal for the COST 273 Channel Model: How to model multi-cluster environments," *COST 273, TD(05)070*, 2005.
- [97] M. Marques, *A Wideband Directional Model for Micro-Cells in UMTS*. Thesis, Instituto Superior Técnico, Lisbon, Portugal, May 2001.

- [98] J. Conrat and P. Pajusco, “A Versatile Propagation Channel Simulator for MIMO Link Level Simulation,” *COST 273, TD(03)120*, 2003.
- [99] J. Proakis, *Digital Communications*. New York: McGraw-Hill, 4th ed., 2000.
- [100] J. Nielsen and G. Pedersen, “GAI Antenna Measurement File Format,” tech. rep., Center for PersonKommunikation Aalborg University, Denmark, January 2003.
- [101] N. Czink, M. Herdin, H. Özcelik, and E. Bonek, “Number of multipath clusters in indoor MIMO propagation environments,” *IEE Electronic Letters*, pp. 1498–1499, November 2004.
- [102] T. Fügen, J. Maurer, C. Kuhnert, and W. Wiesbeck, “A modelling approach for multiuser MIMO systems including spatially-colored interference (cellular example),” in *Proceedings of the IEEE Global Telecommunications Conference (GLOBECOM)*, vol. 2, (Dallas, Tx), pp. 938–942, November 2004.
- [103] A. Molisch, J. Dietert, R. Heddergott, M. Steinbauer, and T. Zwick, “The COST 259 Directional Channel Model III. Micro- and Picocells,” *to be submitted*.
- [104] T. Zwick, C. Fischer, and W. Wiesbeck, “A stochastic multipath channel model including path directions for indoor environments,” *IEEE Journal on Selected Areas Communications*, pp. 1178–1192, August 2002.
- [105] Q. Spencer, B. Jeffs, M. Jensen, and A. Swindlehurst, “Modeling the statistical time and angle of arrival characteristics of an indoor multipath channel,” *IEEE Journal on Selected Areas Communications*, pp. 347–359, March 2000.
- [106] M. Bengtsson and B. Volcker, “On the estimation of azimuth distributions and azimuth spectra,” in *Proceedings of the IEEE Vehicular Technology Conference (VTC) Fall*, vol. 3, (Atlantic City, USA), pp. 1612–1615, October 2001.
- [107] J. Laurila, A. Molisch, and E. Bonek, “Influence of the scatterer distribution on power delay profiles and azimuthal power spectra of mobile radio,” in *Proceedings of the IEEE International Symposium on Spread Spectrum Techniques and Applications (ISSSTA)*, (Sun City, South Africa), pp. 267–271, September 1998.

- [108] U. Trautwein, G. Sommerkorn, C. Schneider, and R. S. Thomä, “Measurement and Analysis of MIMO Channels in Public Access Scenarios at 5.2 GHz,” in *Proceedings of the International Symposium on Wireless Personal Multimedia Communications (WPMC)*, (Aalborg, Denmark), September 2005.
- [109] T. Klingenbrunn and P. Mogensen, “Modelling Cross-Correlated Shadowing in Network Simulations,” in *Proceedings of the IEEE Vehicular Technology Conference (VTC)*, pp. 1407–1411, 1999.
- [110] Forschungszentrum Telekommunikation Wien, *An Implementation of the COST273 Channel Model*: <http://www.ftw.at/cost273/index.html>, 2006.
- [111] http://www.smart-systems.at/smartsim/smartsim_intro_alternate.html.
- [112] 3GPP (3rd Generation Partnership Project), *UMTS Radio Interface*, March 2000.
- [113] R. Clarke and W. L. Khoo, “3-D mobile radio channel statistics,” *IEEE Transactions Vehicular Technology*, pp. 798–799, August 1997.
- [114] V. Erceg, P. Soma, D. Baum, and A. Paulraj, “Capacity obtained from multiple-input multiple-output channel measurements in fixed wireless environments at 2.5 GHz,” in *Proceedings of the International Conference on Communications (ICC)*, vol. 1, pp. 396–400, April 2002.
- [115] T. Zemen, C. Mecklenbräuker, J. Wehinger, and R. Müller, “Iterative Joint Time-Variant Channel Estimation and Multi-User Decoding for MC-CDMA,” *IEEE Transactions Wireless Communications*, vol. 5, pp. 1469–1478, June 2006.
- [116] C. Mecklenbräuker, J. Wehinger, T. Zemen, F. Hlawatsch, and H. Artes, *Multuser MIMO Channel Equalization*, in *Smart Antennas State-of-the-Art*, T. Kaiser and A. Bourdoux (ed.). New York: EURASIP Book Series, Hindawi Publishing Co., 2004.
- [117] W. Jakes, *Microwave Mobile Communications*. New York: John Wiley, 1974.
- [118] Y. G. Li and L. J. Cimini, “Bounds on the interchannel interference of OFDM in time-varying impairments,” *IEEE Transactions on Communications*, vol. 49, pp. 401–404, March 2001.

- [119] D. Slepian, "Prolate spheroidal wave functions, Fourier analysis, and uncertainty - V: The discrete case," *The Bell System Technical Journal*, vol. 57, pp. 1371–1403, May 1978.
- [120] T. Zemen and C. F. Mecklenbräuker, "Time-variant channel equalization via discrete prolate spheroidal sequences," in *Proceedings of the 37th Asilomar Conf. on Signals, Systems and Computers*, (Pacific Grove (CA), USA), pp. 1288–1292, November 2003.
- [121] T. Zemen and C. F. Mecklenbräuker, "Time-Variant Channel Estimation using Discrete Prolate Spheroidal Sequences," *IEEE Transactions on Signal Processing*, vol. 53, pp. 3597–3607, September 2005.
- [122] A. M. Sayeed, A. Sendonaris, and B. Aazhang, "Multiuser detection in fast-fading multipath environment," *IEEE Journal on Selected Areas Communications*, vol. 16, pp. 1691–1701, December 1998.
- [123] T. Zemen, *OFDM multi-user communication over time-variant channels*. Dissertation, Vienna University of Technology, Vienna, Austria, August 2004.
- [124] T. Zemen, C. F. Mecklenbräuker, J. Wehinger, and R. R. Müller, "Iterative multi-user decoding with time-variant channel estimation for MC-CDMA," in *Proceedings of the Fifth International Conference on 3G Mobile Communication Technologies*, (London, United Kingdom), 2004.
- [125] H. Hofstetter, T. Zemen, J. Wehinger, and G. Steinböck, "Iterative MIMO Multi-User Detection: Performance Evaluation with COST 259 Channel Model," in *Proceedings of the International Symposium on Wireless Personal Multimedia Communications (WPMC)*, (Abano Terme, Italy), September 2004.
- [126] Y. R. Zheng and C. Xiao, "Simulation models with correct statistical properties for Rayleigh fading channels," *IEEE Transactions on Communications*, vol. 51, pp. 920–928, June 2003.
- [127] T. Zemen and C. Mecklenbräuker, "Doppler diversity in MC-CDMA using the Slepian basis expansion model," in *Proceedings of the 12th European Signal Processing Conference (EUSIPCO)*, (Vienna, Austria), September 2004.

Biography

Personal Data

Name: Helmut Hofstetter
 Date of birth: 18.10.1975
 Place of birth: Krems, Austria
 Address: Landersdorferstrae 33a,
 A-3500 Krems, Austria

Education

2000 - Doctoral studies at Vienna University of Technology.
 Mar. 2000 Diplom-Ingenieur, with honors, Electrical Engineering / Communications,
 Vienna University of Technology.
 1995 - 2000 Electrical Engineering studies at Vienna University of Technology.
 Jun. 1995 Matura, with honors.
 1990 - 1995 High school, Hhere Technische Bundeslehranstalt St. Plten
 - Department for Engineering and Automation.
 1986 - 1990 Realgymnasium in Krems, Ringstrasse.
 1982 - 1986 Elementary school Krems Lerchenfeld.

Professional Background

Positions held

2006 Researcher, Institute Eurcom , Mobile Communications
 2001 - 2005 Project manager, FTW - Telecommunication Research Center Vienna.
 2000 - 2005 Researcher for Mobile Communications, FTW - Telecommunication
 Research Center Vienna.
 1999 - 2000 Scientific Assistant at Vienna University of Technology ,
 Mobile Communications.

Visits

2002 Telenor Research and Development, MIMO measurements within the
 IST project FLOWS, Oslo, Norway. Duration: 3 months.